Searches for Stellar Radio Activity in Circular Polarisation

Joshua Pritchard

A thesis submitted in fulfilment of the requirements for the degree of

Doctor of Philosophy (PhD)

Supervisor:
Prof. Tara Murphy

Co-supervisors:
Dr. George Heald

THE UNIVERSITY OF SYDNEY

The University of Sydney
Faculty of Science
School of Physics

February 21, 2024

For Mars and Antares—may you dance together for an age.

Statement of Originality

This is to certify that to the best of my knowledge, the content of this thesis is my own work. This thesis has not been submitted for any degree or other purposes. I certify that the intellectual content of this thesis is the product of my own work and that all the assistance received in preparing this thesis and sources have been acknowledged.

Authorship Attribution Statement

I confirm that the authorship attribution statements at the beginning of each chapter are correct.

Joshua Pritchard

February 21, 2024

As supervisor for the candidature upon which this thesis is based, I confirm that the originality and authorship attribution statements given above, and at the beginning of each chapter are correct.

Prof. Tara Murphy

February 21, 2024

Abstract

Transient radio bursts produced in the coronae of stellar atmospheres and within planetary magnetospheres often feature a high degree of circular polarisation. These events reveal the presence of strong magnetic fields, and trace particle acceleration driven by magnetic reconnection, space weather, and auroral current systems. The detection of stellar radio emission has historically been challenged by the overwhelmingly higher surface density of extragalactic sources that dominate the radio sky, which produce a large number of false positive associations to optically identified stars. Our knowledge of the radio star population has therefore been primarily driven by targeted study of the most active, nearby systems, impacting the inference of population statistics and discovery of new regimes of stellar radio activity.

In this thesis I present a body of work that exploits the circular polarisation of magnetically driven stellar radio emission to identify large samples of radio stars in widefield surveys. I demonstrate the use of this technique as part of the first all-sky survey with the Australian Square Kilometre Array Pathfinder (ASKAP)—the Rapid ASKAP Continuum Survey (RACS)—which resulted in the detection of 33 radio stars, 23 of which have not been previously reported active at radio frequencies. I further extend this search technique to the multi-epoch Variables and Slow Transients (VAST) pilot survey resulting in 196 detections of a sample of 46 radio stars, and use the repeat sampling of this group to present constraints on the statistical fraction of the M-dwarf population that produce radio bursts. Finally, I describe the use of this technique to discover auroral radio pulses from the M9.5 ultracool dwarf SCR J1845−6357—the oldest and slowest rotator among radio detected ultracool dwarfs to date—and present results from a two year monitoring campaign with ASKAP and the Australia Telescope Compact Array. I conclude by outlining the application of circular polarisation searches to future surveys with ASKAP and next generation instruments such as the Square Kilometre Array, which will result in tens of thousands of new radio star detections and provide a new window into stellar magnetism.

This thesis was primarily written at my home and at the University of Sydney, on the land of the Gadigal people of the Eora nation.

The work presented in this thesis uses observations from the Australia Telescope Compact Array, which stands on the land of the Gomeroi people, and the Australian Square Kilometre Array Pathfinder, which stands on the land of the Wajarri Yamatji people.

Acknowledgements

I would like to acknowledge and thank all of the wonderful people that supported me throughout my candidature and fostered my development as a scientist.

I am immensely grateful to my supervisor Tara Murphy for constant guidance and endless patience throughout the last four years. Nine years ago you took the time to eat pizza with me and talk about my study plans, and gave me the encouragement I needed to return to university and study physics. Over the course of my PhD your advice has always pushed me in new and interesting directions, and you have shaped the way that I think as a scientist.

I am similarly grateful to my co-supervisor George Heald. From plot suggestions to helping strengthen the construction of my arguments, you have been a constant source of advice for improving the presentation of my work. I have benefited greatly from your understanding of radio interferometry and polarisation, and I am humbly grateful for your guidance in learning these black magics.

Thanks to all of the fellow students and colleagues I have worked with—to Dougal Dobie, Andrew Zic, and Harry Qiu for the support as I was beginning as a student and for providing observing guidance with ATCA. Particular thanks go to Andrew Zic for helping to shape much of what I know about radio stars. To my PhD office (and remote office) mates Daniele d'Antonio, Mark Edwards, Ashna Gulati, Emily Kerrison, James Leung, Liroy Lourenco, Kovi Rose, Gary Strain, Yuanming Wang, and Ziteng (Andy) Wang. It has been fantastic to endure the PhD journey alongside you all, and I am grateful for your camaraderie as virtual officemates throughout the pandemic. Thanks in particular to Kovi Rose for proofreading this thesis.

Beyond those already mentioned, I have had the pleasure to work with many fantastic collaborators—including Akash Anumarlapudi, Craig Anderson, Julie Banfield, Martin Bell, Gerry Doyle, Laura Driessen, Stefan Duchesne, Catherine Hale, Aidan Hotan, Richard "Dick" Hunstead, Luca Ighina, David L. Kaplan, Emil Lenc, Christene Lynch, Dave McConnell, Vanessa A. Moss, Andrew O'Brien, Miguel Pérez-Torres, Sergio Pintaldi, Wasim Raja, Gavin Ramsay, Stuart Ryder, Jeremy Rigney, Elaine Sadler, Gregory Sivakoff, Adam J. Stewart, Michael S. Wheatland, Tim White, and Matthew Whiting. Among these my thanks in particular go to Martin Bell who co-supervised me during Honours and taught me a lot about fundamental radio astronomy; David Kaplan for always having helpful comments to improve my work; and Emil Lenc for constant help with technical questions and always having a friendly ear for complaints about the conventions of circular polarimetry.

I am grateful for the support and interest of the entire Variables and Slow Transients group, the Sydney Institute for Astronomy, and CSIRO Space and Astronomy. I would also like to acknowledge support from the Australian Government through the Research Training Program scholarship.

I am extremely grateful to my family for your love and support over the last several years, and your understanding when I have taken a week to pick up the phone. To my Mum Jacqueline, Dad Andrew, and brother Callum, you have encouraged me throughout every endeavour of my life and this support has given me the necessary comfort and confidence to pursue my goals. Mum and Dad, you shaped the way I think about the world and taught me how to question and challenge new information. Cal, don't worry you never have to call me Dr. :). To my late grandparents, Claire and Peter Wood, thank you for the support you always gave me growing up. Grandma you taught me to build an attitude of confidence and were one of the toughest yet kindest people I have ever known. Pa, you always inspired me to want to learn more about the world and will always be a source of curiosity. I love and miss you both. Love and thanks to my newest family members—Greg, Sue, Jack, Lorraine, Evie, James, Alex, Gabi, Tommy, Libby, and Briony.

My deepest thanks to my primary home office mates Elio, MJ, and Calypso. Elio, it has been inspiring to watch the diligent work on your PhD thesis "*A Density Wave Theory of Transient Archimedean Plumbing Spirals*". MJ you were a pillar of support throughout the last seven years and will always have a place in my heart. I miss you. Calypso, my thanks to you for the early morning wakeup calls to ensure I kept a good work pace.

Most of all, thank you to my fiancée Sammy. I am so immensely grateful for your constant love, guidance, and support. You encouraged me to stick through every difficult stage of this project, and constantly inspire me with your ambition, drive, and passion. You got me through the isolation of the pandemic and somehow made it a joy to endure, and you lit up our home with laughter and music and didn't let me get buried by the ups and downs of a research project. I could not have finished this without you. This is for you.

Amid all the splendours of the World,
its vast halls and spaces, and its wheeling fires,
Ilúvatar chose a place for their habitation
in the Deeps of Time and in the midst of the innumerable stars.

And this habitation might seem a little thing to those ...
who consider only the immeasurable vastness of the World ...
and not the minute precision to which they shape all things therein.

— J. R. R. Tolkien

Contents

List of Figures

List of Tables

Summary of Works

This thesis contains one peer-reviewed publication, one submitted paper that is currently under review, and one paper currently in preparation.

> Chapter 2 has been published as *"A circular polarization survey for radio stars with the Australian SKA Pathfinder."* in Pritchard J., et al., 2021, MNRAS, 502, 5438

> Chapter 3 has been published as *"Multi-epoch sampling of the radio star population with the Australian SKA Pathfinder"* in Pritchard J., et al., 2024, MNRAS, p. stae127

> Chapter 4 is currently being prepared for submission under the working title *"Two year monitoring of auroral pulses from the slowly rotating ultracool dwarf SCR J1845−6357"*

In addition to these primary works, I list 20 peer-reviewed publications that I have made contributions to as a coauthor during completion of this thesis.

> Dobie D., et al., 2019, *"An ASKAP search for a radio counterpart to the first high-significance neutron star-black hole merger LIGO/VIRGO s190814bv."*, ApJ, 888, L13

> McConnell D., et al., 2020, *"The Rapid ASKAP Continuum Survey I: Design and first results"*, PASA, 37, e048

> Ackley, K., et al., 2020, *"Neutron Star Extreme Matter Observatory: A kilohertz-band gravitational-wave detector in the global network"*, PASA, 37, e047

> Hale C. L., et al., 2021, *"The Rapid ASKAP Continuum Survey Paper II: First Stokes I Source Catalogue Data Release"*, PASA, 38, e058

> Leung J. K., et al., 2021a, *"A search for radio afterglows from gamma-ray bursts with the Australian Square Kilometre Array Pathfinder"*, MNRAS, 503, 1847

> Wang Z., et al., 2021, *"Discovery of ASKAP J173608.2-321635 as a Highly Polarized Transient Point Source with the Australian SKA Pathfinder"*, ApJ, 920, 45

> Dobie D., et al., 2022, *"A comprehensive search for the radio counterpart*

of GW190814 with the Australian Square Kilometre Array Pathfinder", MNRAS, 510, 3794

Ighina L., et al., 2022, *"Constraining the radio properties of the $z = 6.44$ QSO VIK J2318−3113"*, A&A, 663, A73

Murphy T., et al., 2021, *"The ASKAP Variables and Slow Transients (VAST) Pilot Survey"*, PASA, 38, e054

Rigney J., et al., 2022, *"Searching for stellar flares from low-mass stars using ASKAP and TESS"*, MNRAS, 516, 540

Wang Y., et al., 2022, *"Radio variable and transient sources on minute time-scales in the ASKAP pilot surveys."*, MNRAS, 523, 5661

Wang Z., et al., 2022, *"A pilot ASKAP survey for radio transients towards the Galactic Centre"*, MNRAS, 516, 5972

Anumarlapudi A., et al., 2023, *"Characterizing Pulsars Detected in the Rapid ASKAP Continuum Survey"*, ApJ, 956.1, 28

Dobie D., et al., 2023, *"Radio transients and variables in the tenth Deeper, Wider, Faster observing run"*, MNRAS, 519, 4684

Duchesne S. W., et al., 2023, *"The Rapid ASKAP Continuum Survey IV: continuum imaging at 1367.5 MHz and the first data release of RACS-mid"*, PASA, 40, e034

Wang Y., et al., 2023, *"Discovery of PSR J0523−7125 as a circularly polarized variable radio source in the Large Magellanic Cloud."*, ApJ, 930, 38

Gulati A., et al., 2023, *"Classical novae in the ASKAP pilot surveys"*, PASA, 40, e025

Rose K., et al., 2023, *"Periodic radio emission from the T8 dwarf WISE J062309.94−045624.6"*, ApJ, 951, L43

Zic, A., et al., 2024, *"Discovery of radio eclipses from 4FGL J1646.5-4406: A new candidate redback pulsar binary"*, MNRAS

Duchesne, S. W., et al., 2024, *"The Rapid ASKAP Continuum Survey V: Cataloguing the sky at 1 367.5 MHz and the second data release of RACS-mid"*, PASA, 41, e003

Chapter 1

Introduction

In 1932 Karl Jansky serendipitously discovered a source of radio emission repeating at the sidereal period of 23 h 56 min—unambiguous evidence for an origin beyond the Solar system (Jansky 1933). The discovery gained significant coverage in popular media outlets but received minimal attention from the astronomy community. Continued study of radio astronomy was initially only carried out by Grote Reber who confirmed the extrasolar detection and began to map the radio sky (Reber 1940). The radio source was associated with emission originating from the Milky Way, but its physical origin was not understood until much later.

The development of radio receivers advanced considerably with widespread use throughout the second world war, and in 1942 British physicist and then radar operator Stanley Hey discovered a source of radio noise interfering with radar equipment across Britain. Hey localised the signal to a group of active sunspots, marking the first detection of radio emission from the Sun. The detection was kept a secret until the end of the war (Hey 1946), and Solar radio emission was independently discovered by Reber in the meantime (Reber 1944). In the following years the Sun became one of the most well studied objects in the radio sky, revealing a variety of thermal and non-thermal radio emissions associated with Solar magnetic activity and space weather (McCready et al. 1947; Payne-Scott et al. 1947).

Hey went on to produce another apparent radio star discovery, detecting multiple sources of radio emission across the sky that were spatially unresolved and poorly localised in comparison to the optical sky (Hey et al. 1946). The source of the radio emission was unknown, with Reber suggesting an origin in the gas of the interstellar medium (Reber & Greenstein 1947) and other authors—namely Martin Ryle—suggesting the emission originated from stellar atmospheres (Ryle 1949). The *radio star hypothesis* was a topic of debate through to the mid 1950s despite Bolton & Stanley (1949) demonstrating the nature of these sources to be compact and likely associated with optical sources such as Taurus A (the Crab Nebula), Cygnus A, Virgo A, and Centaurus A. One of the main setbacks to accepting the non-stellar origin of these objects was a gap in the theory of the synchrotron radio emission produced in magnetised plasmas.[1] With the development of synchrotron theory by

[1] This topic will be discussed further in § 1.1.

Schwinger (1949) and its application to explain the optical emission from the Crab Nebula by Shklovski (1953), it became widely accepted the "radio stars" were in fact associated with extragalactic emission sources. The radio star hypothesis lost favour, and the Sun again became the only known true radio star.

In the next decade searches for the first true radio stars were conducted (see Lovell (1964a) for a review of their history). These searches detected burst activity from very active nearby stars that were known to produce optical flares, such as V371 Ori (Slee 1963) and UV Cet (Lovell 1964b), but used large single-dish telescopes with poor resolution and a limited capability to identify large samples. Through to the modern era, even with high angular resolution interferometric radio telescopes radio stars have been difficult to identify in large quantities, primarily due to false-positive association with the original "radio stars"—the large population of extragalactic radio sources that dominate the sky. However, one route to separating these populations is through the polarisation properties of their radio emission, as sources of stellar radio emission are often highly *circularly polarised* while the synchrotron emission powering most extragalactic sources has essentially no circular polarisation.

In this thesis I will present a body of work focused on the use of circular polarisation to distinguish radio stars from extragalactic radio sources in widefield surveys with the Australian Square Kilometre Array Pathfinder. In § 1.1 I describe the micro-physical processes that are relevant to the production of stellar radio emission, and in § 1.2 I review the macro-physics of stellar environments in which these processes are activated. In § 1.3 I review previous efforts to detect non-thermal radio emission from magnetically active stars in both targeted and widefield surveys, and motivate the utility of circular polarisation searches in overcoming the challenges encountered by traditional search techniques. Finally, in § 1.4 I summarise the contents of this thesis in employing circular polarisation searches to build large samples of previously undetected radio stars.

1.1 Stellar Radio Emission Mechanisms

1.1.1 Radio Emission Fundamentals

A wide range of micro-physical processes are responsible for the production and propagation of radio emission in astrophysical plasmas. In this section I briefly review the fundamental physics underlying these processes so they can be applied in the context of emission from the magnetised environment of stellar atmospheres.

With the exception of emission from transitions between atomic bound states—for example the OH, CO, and H I spectral lines—astrophysical radio emission is primarily produced by the acceleration of charged particles following the Larmor formula, given in its covariant form (Jackson 1999) by

$$P = \frac{2}{3c^3}\left(\frac{q_\alpha}{m_\alpha}\right)^2 \gamma^2 \left[\left(\frac{\mathrm{d}\mathbf{p}}{\mathrm{d}t}\right)^2 - \frac{1}{c^2}\left(\frac{\mathrm{d}\mathcal{E}}{\mathrm{d}t}\right)^2\right], \tag{1.1}$$

where P is the radiated power, m_α and q_α are the mass and charge of the particle of species α, $\gamma = (1 - v^2/c^2)^{-1/2}$ is the Lorentz factor, v, $\mathbf{p}$ and $\mathcal{E}$ are the particle velocity, momentum and energy, and c is the speed of light. Two important details result from this relationship. The power produced by electron accelerations far exceeds that of ions, due to the factor of 1 836 higher charge to mass ratio over that of the proton. Secondly, more power is produced by accelerations for which $\mathrm{d}\mathcal{E}/\,\mathrm{d}t = 0$, so that forces perpendicular to the particle velocity—such as those imparted by magnetic fields—are more important than forces parallel to the motion.

The radio power collected by a telescope is dependent upon multiple instrumental factors such as the projected area of the telescope aperture $\cos\theta\,\mathrm{d}A$ and frequency bandwidth $\mathrm{d}\nu$, and further depends on the solid angle $\mathrm{d}\Omega$ from which the emission is being received. However, normalising by these factors, a quantity upon which all observers can agree is the *specific intensity*

$$I_\nu = \frac{\mathrm{d}P}{\cos\theta\,\mathrm{d}A\,\mathrm{d}\Omega\,\mathrm{d}\nu}. \tag{1.2}$$

For radio sources extending over a small solid angular extent, integrating I_ν over the angular source distribution produces the *spectral flux density*

$$S_\nu = \int_{\mathrm{source}} I_\nu\,\mathrm{d}\Omega \tag{1.3}$$

which is traditionally expressed in units of Jansky, where $1\,\mathrm{Jy} = 10^{-26}\,\mathrm{Wm^{-2}Hz^{-1}}$. Image-plane maps of radio intensity are often quoted in units of Jansky per solid angle of synthesised beam or point-spread-function (PSF), and the latter is used throughout this thesis. These quantities each depend upon the distance d between observer and source, and therefore the *spectral radio luminosity*

$$L_\nu = S_\nu 4\pi d^2 \tag{1.4}$$

is often useful to describe the intrinsic radio power produced by a source within the bandwidth $\mathrm{d}\nu$. These quantities are often written without including the term "spectral", and I will use this practice throughout the rest of this thesis.

A number of propagation effects modify the intensity produced in a source region through the absorption and emission of radiation along the path to an observer. The evolution of I_ν along a path s is described by the *radiative transfer* equation

$$\frac{\mathrm{d}I_\nu}{\mathrm{d}s} = j_\nu - \kappa_\nu I_\nu, \tag{1.5}$$

where the emission coefficient j_ν represents sources of radiation that contribute emission along the path of propagation, and the absorption coefficient κ_ν represents the tendency for emission to be attenuated by absorption per unit path length. A useful quantity to describe the relative impact of absorption along the path $s = s_2 - s_1$ is the *optical depth*

$$\tau = \int_{s_1}^{s_2} \kappa_\nu(s)\,\mathrm{d}s. \tag{1.6}$$

When $\tau \ll 1$ the emission is described as *optically thin* and intervening plasma has a minor effect on the characteristics of background radiation, while for $\tau \gg 1$ the emission is called *optically thick*, and there is sufficient absorption and emission from intervening plasma to destroy information about the background. In this scenario the specific intensity approaches the *source function*

$$I_\nu = J_\nu = \frac{j_\nu}{\kappa_\nu}, \tag{1.7}$$

and in regions of local thermodynamic equilibrium tends to the Planck function

$$I_\nu = J_\nu = B(\nu, T) = \frac{2h\nu^3}{c^2}\frac{1}{\exp\left(h\nu/k_B T\right) - 1}, \tag{1.8}$$

where h is Planck's constant, k_B is Boltzmann's constant, and T is the blackbody temperature. This result is known as Kirchoff's law, and ties the emission and absorption properties of any system in local thermodynamic equilibrium to the spectrum of a blackbody.

At radio frequencies the photon energy $h\nu$ is typically much lower than the thermal energy $k_B T$, and therefore emission is generally only significant in the Rayleigh-Jeans tail of $B(\nu, T)$

$$B(\nu, T) \approx \frac{2k_B T \nu^2}{c^2}. \tag{1.9}$$

The specific intensity is then often expressed in terms of *brightness temperature*, which is the corresponding temperature a blackbody would require to produce a given specific intensity at frequency ν

$$T_b = I_\nu \frac{c^2}{2k_B \nu^2}. \tag{1.10}$$

In general the brightness temperature is independent of the local thermodynamic temperature T, and only equivalent when the emitting system is in local thermodynamic equilibrium. Instead T_b is simply an alternate way of expressing I_ν in units of temperature, and provides an additional diagnostic of the mechanism driving radio emission. Emission processes are described as *thermal* when the plasma is in local thermodynamic equilibrium and develops a *Maxwellian* velocity distribution

$$f(v) = \left[\frac{m_\alpha}{\sqrt{2\pi k_B T}}\right]^{-\frac{3}{2}} \exp\left(-\frac{m_\alpha v^2}{2k_B T}\right), \tag{1.11}$$

where v is the particle velocity, while *non-thermal* emission is associated with a deviation from this distribution, typically through inclusion of either a high energy tail or anisotropy in the particle velocity distribution. Many non-thermal plasmas in astrophysical environments are well described by a power law

$$n(\mathcal{E}) = (\delta - 1)\mathcal{E}_0^{\delta-1} N \mathcal{E}^{-\delta} \tag{1.12}$$

where $\mathcal{E}_0$ is a minimum energy, $n(\mathcal{E})$ is the number density of electrons with energy $\mathcal{E}$, N is the number of electrons with energy $\mathcal{E} > \mathcal{E}_0$, and δ is the electron energy spectral index (Dulk 1985).

Emission processes can be further distinguished by the coherence of the radiated fields, where the radio emission produced by most processes is *incoherent* in the sense that the radiation produced by multiple particles is uncorrelated. An emission mechanism is considered *coherent* if the radiation produced by N separate particles is correlated in phase, resulting in an intensity that is enhanced by a factor N^2 rather than the N factor increase from adding the fields incoherently. This may be achieved in a magnetised plasma through one of three types of instability in the particle distribution (Melrose 2009):

1. an *antenna* instability, in which particles bunch together with both momenta and spatial positions correlated on a scale smaller than the emission wavelength, and thus radiate together as a macro-particle;
2. a *reactive* instability in which particle motion is correlated only in momentum-space and wave-particle interactions lead to particles bunching in phase;
3. a *maser* instability in which the particle distribution is uncorrelated, but develops a population inversion in momentum space that acts as a source of free energy powering wave growth through negative absorption, in analogue to stimulated emission in a classical maser/laser.

In astrophysical plasmas the growth rates of these processes saturate over rapid timescales (Melrose 1991) and evolve into one another—with antenna emission causing particles to diffuse and become spatially uncorrelated forming a reactive instability, and reactive mechanisms subsequently randomising particle momenta as the wave grows forming a maser instability. Maser instabilities then saturate as relaxation of the particle distribution reaches a steady state balance with the engine driving the instability, and therefore likely represent the observable stage of the majority of coherent radiation processes (Melrose 2017).

The brightness temperature of incoherent emission mechanisms is limited by the *inverse Compton catastrophe* (Kellermann & Pauliny-Toth 1969)—where repeated inverse Compton scattering in the most energetic sources of synchrotron emission results in rapid cooling to a maximum attainable brightness temperature of

$T_B \sim 10^{12}$ K. This limit is often only reached at frequencies $\gtrsim$1 GHz by relativistic beaming of emission from the brightest quasars, and often softer limits of $T_B \sim 10^{11}$ K are observed where equipartition is reached in energy density between the source electrons and local magnetic field (Readhead 1994).

1.1.2 Magneto-ionic Wave Modes

A wide variety of stellar radio emission processes are driven by the acceleration of electrons within a magnetised plasma. Two characteristic frequencies in these environments are the angular plasma frequency $\omega_p = \sqrt{4\pi n_e e^2/m_e}$ and electron cyclotron frequency $\omega_e = eB/m_e c$, where e and m_e are the charge and mass of the electron, n_e is the local electron density, B is the local magnetic field strength, and c is the speed of light. The excitation of wave modes in the plasma is generally treated with the *magneto-ionic theory* (Hartree 1931; Appleton 1932), in which the plasma is treated as a cold, magnetised electron gas, ignoring thermal electron motions and assuming the ion component of the plasma is stationary. Electromagnetic waves in this plasma are dispersive due to a bi-refringent response to the refractive index, such that the speed of waves varies with polarisation with respect to the ambient magnetic field.

The two natural wave modes in such a plasma are the *ordinary* and *extra-ordinary* modes which are polarised with electric field parallel and perpendicular to the ambient magnetic field respectively. For arbitrary propagation angle θ with respect to the local magnetic field, each mode has an upper and lower branch in the dispersion relations, pictured in Figure 1.1. The lower branch of the ordinary mode is called the whistler or w-mode and disappears for purely perpendicular propagation ($\theta = \pi/2$), while the lower extra-ordinary branch is called the z-mode and is present for all θ. These modes are polarised with electric field parallel to the wavevector $\mathbf{k}$ with resonances at the respective lower and upper hybrid frequencies $\omega_{lh} = 1/\sqrt{\omega_p^2 + \omega_i\omega_e}$ and $\omega_{uh} = \sqrt{\omega_p^2 + \omega_e^2}$, which inhibit coupling to free-space wave modes preventing escape as radiation. The w- and z-modes are therefore not of further interest to the work in this thesis. The upper branches are known by the names of their parent modes, with the ordinary (o-mode) propagating freely above the cutoff at ω_p with the same dispersion as in an unmagnetised plasma, while the extra-ordinary (x-mode) is influenced by the ambient magnetic field and can only propagate above the x-mode cutoff frequency $\omega_x = \omega_p + \omega_e$.

The magneto-ionic modes are elliptically polarised with the fractional degree of linear (f_{LP}) and circular (f_{CP}) polarisation strongly dependent on θ. However, often the *quasi-circular* and *quasi-planar* approximations are appropriate in which the waves are respectively fully circularly and linearly polarised (Melrose 1986). The quasi-circular approximation applies in the condition

$$\frac{\omega^2\omega_e^2}{(\omega^2 - \omega_p^2)^2}\frac{\sin^4\theta}{\cos^2\theta} \ll 1 \tag{1.13}$$

which occurs for a large range of propagation angle and frequency combinations,

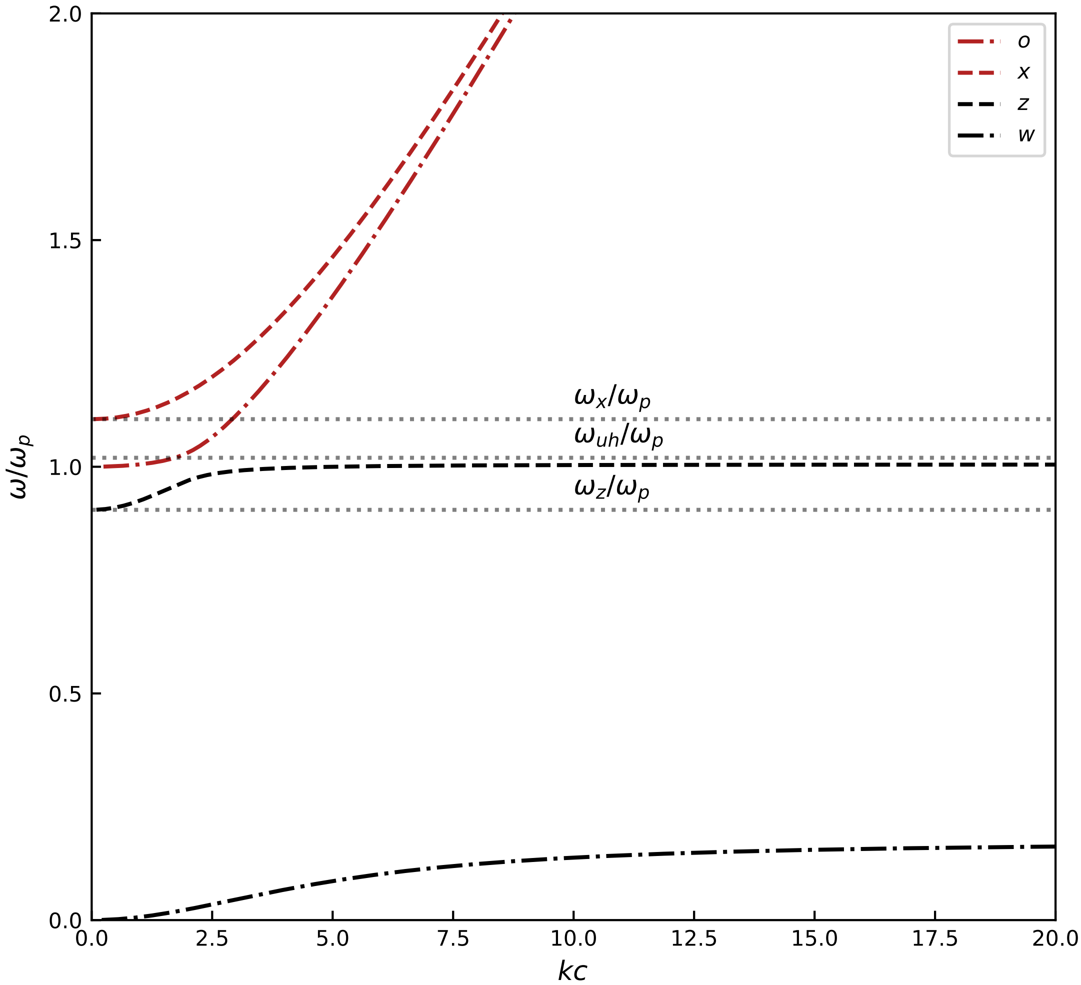

Figure 1.1: Dispersion relation for the four magneto-ionic modes in a cold, magnetised plasma with $\omega_p/\omega_e = 5$ and wavevector oriented at an angle $\theta = \pi/6$ with respect to the ambient magnetic field. Dot-dashed lines show the two ordinary solution branches of ω/ω_p as a function of wavenumber in units of frequency kc, with the o-mode in red and the w-mode in black, while dashed lines show the two extra-ordinary branches with the x-mode shown in red and the z-mode shown in black. The w- and z-modes are prohibited from escaping as radiation due to resonances at the lower hybrid frequency ω_{lh} and upper hybrid frequency ω_{uh} respectively. The o- and x-modes are free to propagate as right and left circularly polarised waves above cutoff frequencies of ω_p and ω_x respectively.

and therefore the o-mode and x-mode waves are typically treated as 100 % circularly polarised. The x-mode polarisation vector rotates in the same sense as the electron gyro-motion—corresponding to right-handed circular polarisation for waves emitted somewhat aligned with the ambient magnetic field and left handed polarisation if anti-aligned, while the o-mode is polarised in the opposite sense. A differential generation or propagation of the two modes then leads to a net circular polarisation in the received radiation, providing a diagnostic of the magnetic field orientation in the source region.

1.1.3 Bremsstrahlung Emission

Bremsstrahlung radiation is produced when electrons experience accelerations due to Coulomb interactions with ions in the plasma. As this interaction is between particles in free space rather than bound atomic states, this mechanism is often also referred to as *free-free* emission. The spectral profile of free-free emission is broadband above a lower cutoff at the plasma frequency ω_p below which the magneto-ionic modes cannot propagate, and scales with ν^{-2} in the optically thin regime while independent of frequency when optically thick. In the plasma conditions typical of stellar chromospheres and coronae the absorption coefficient is given by

$$\kappa_{ff} = 0.2 \frac{n_e^2}{T^{3/2} \left(\nu \pm \nu_e \cos\theta\right)^2}, \tag{1.14}$$

where the $+/-$ signs in the denominator correspond to o-mode and x-mode respectively (Zlotnik 1968; Gelfreikh 2004). The stronger x-mode emission can lead to mild circular polarisation in optically thin plasmas ($f_{CP} \approx 2\left(\nu_e/\nu\right)\cos\theta$) (e.g. McCauley et al. 2019), while in the optically thick regime the polarisation information is lost (Dulk 1985).

1.1.4 Gyromagnetic Emission

In magnetised plasmas the dominant acceleration mechanism is the Lorentz force

$$\mathbf{F} = q\left(\mathbf{E} + \mathbf{v} \times \mathbf{B}\right), \tag{1.15}$$

which causes electrons and ions to undergo helical motion about the ambient magnetic field. Electromagnetic waves can be excited with large intensities when in resonance with the gyrating electrons, meeting the condition

$$\omega - \frac{s\omega_e}{\gamma} - k_{\parallel} v_{\parallel} = 0 \tag{1.16}$$

where s is the harmonic number of ω_e, and $k_{\parallel}$ and $v_{\parallel}$ are the components of the wavevector and electron velocity parallel to the ambient magnetic field direction. In strongly magnetised plasmas the first two terms dominate over the third and emission occurs at harmonics of the electron cyclotron frequency $\omega \approx s\omega_e$. The emissivity of gyromagnetic emission at each harmonic is in general represented in terms of Bessel functions, and precise solution requires non-trivial summation over the harmonic ranges relevant to a particular electron velocity distribution. In practice gyromagnetic emission is therefore treated separately in three regimes depending upon the relevant harmonic ranges—gyroresonance emission, gyro-synchrotron emission, and synchrotron emission.

Gyro-resonance emission occurs in the regime in which the electrons are non-relativistic ($\gamma - 1 \ll 1$) and therefore typically features a thermal velocity distribution due to frequent particle collisions. Here, the non-relativistic gyro-motion of electrons results in a $\sin^2\theta$ angular emission pattern where θ is the angle with respect to the particle velocity, and significant power is only produced at low order harmonics $s \simeq 10$. The Bessel functions are typically approximated by the leading term in a Taylor series expansion and summed only over a small harmonic range (Melrose 1986), allowing expressions for the optical depth to be obtained that are a strong function of emission angle with respect to the ambient magnetic field (e.g. Zlotnik 1968; Robinson & Melrose 1984; White & Kundu 1997). The emission is optically thick for a large range of propagation angles and hence becomes depolarised—but for some propagation angles the optical depths of each mode vary, leading to a high degree of circular polarisation in the sense of the o-mode (White & Kundu 1997). While gyro-resonance emission is a probe of enhanced magnetic activity in the chromosphere, absorption of radiation through the inverse process of this mechanism is also important in the context of stellar radio emission, where emission produced at lower coronal depths may be absorbed in overlaying gyro-resonance layers.

Synchrotron emission occurs in the opposite limit in which electrons are ultra-relativistic ($\gamma - 1 \gg 1$) and the gyro-motion of electrons is Doppler boosted, causing the majority of emission to radiate into a narrow beam of width $2/\gamma$ oriented in the direction of the instantaneous particle velocity (Ginzburg & Syrovatskii 1965). The received emission is modulated into pulses that are only visible over a fraction of each cyclotron period, causing high-order harmonics in the range $s > 100$ to contribute significant power to the emission profile. By treating the large harmonic range as continuous, the Bessel functions can then be approximated with Airy functions to calculate the emissivity and polarisation (e.g. Melrose & Dulk 1982). The spectral shape of synchrotron emission typically follows a power-law $S_\nu \propto \nu^{\alpha_\nu}$ with separate spectral indices α_ν in the optically thick and thin regimes. In the optically thin regime the spectral index $\alpha_\nu = -(\delta - 1)/2$ is dependent on the electron energy index δ (see Equation (1.12)), and in the optically thick regime where synchrotron self-absorption causes a spectral turnover the index becomes $\alpha_\nu = 2.5$.

Synchrotron emission is linearly polarised with very low degrees of circular polarisation (Stocke & Scott 1975), and requires exotic circumstances for circular polarisation greater than of order 1 % (e.g. Melrose 1971; Pacholczyk & Swihart 1971). The majority of continuum radio sources are powered by synchrotron emission including active galactic nuclei and diffuse Galactic emission. Synchrotron emission is also relevant in some stellar environments, such as the winds of hot stars (White 1985) and magnetospheric radiation belts (Bolton et al. 2002)—however, the majority of magnetically driven stellar radio emission is driven by the other processes described in this section and feature moderate to high degrees of circular polarisation. The low degree of circular polarisation of synchrotron emission therefore provides an extremely effective filter for the selection of stellar radio sources and it is this property that is exploited in the body of work presented in this thesis to efficiently identify radio stars.

Gyro-synchrotron emission is produced by mildly relativistic particle distributions ($\gamma - 1 \approx 1$), with harmonics in the range $10 < s < 100$ contributing. In this velocity regime the gyro-magnetic emission Bessel functions are neither well approximated by a truncated Taylor series nor by an Airy integral. Numerical calculations of the emissivity and absorption of gyro-synchrotron emission have been presented by several authors (e.g. Ramaty 1969; Takakura 1972; Simões & Costa 2006, 2010) though are computationally intensive to reproduce as a diagnostic for observed gyro-synchrotron spectra. Simplified expressions are therefore often used that relate the shape of the gyro-synchrotron emission spectrum to fundamental plasma parameters (e.g. Robinson & Melrose 1984; Dulk & Marsh 1982) such as the electron density n_e, magnetic field strength B, emission viewing angle θ, and distributions of electron energy and pitch angle (e.g. Stähli et al. 1989).

The full spectral shape is typically in the form of a broken power-law, with a characteristic turnover frequency ν_{peak} and separate power-law spectral indices in the optically thin ($\nu > \nu_{\mathrm{peak}}$) and optically thick ($\nu < \nu_{\mathrm{peak}}$) regimes. The optically thin spectral index $\alpha_\nu = 1.2 - 0.9\delta$ is a probe of the electron energy index δ, while the optically thick slope is dependent on multiple absorption factors—including gyro-synchrotron self-absorption, free-free and gyro-resonance absorption during propagation, and Razin-Tsytovich suppression as the plasma refractive index deviates significantly from unity (Klein & Chiuderi-Drago 1987).

The polarisation of non-thermal gyro-synchrotron emission is similarly dependent upon source parameters, with high degrees of fractional circular polarisation possible depending upon viewing angle θ, and the distribution of electron energy. The emission is polarised in the sense of the x-mode when optically thin and the o-mode when optically thick, causing gyro-synchrotron spectra to show an inversion in the sign of circular polarisation around ν_{peak}. Gyro-synchrotron emission can also be driven by high temperature thermal populations with a sufficient population of relativistic electrons in the high-energy Maxwellian tail. Recently extrasolar thermal gyro-synchrotron emission has been detected for the first time in two young stellar objects (Golay et al. 2023).

1.1.5 Electron Cyclotron Maser Instability

The electron cyclotron maser instability (ECMI) is a reactive instability between electron gyromotion and a right circularly polarised electromagnetic wave (Wu & Lee 1979). Wave-particle resonance results in electrons seeing a stationary rest-frame electric field that causes momentum-space bunching in gyro-phase angle (Chu 2004). Energy transfer between the wave and particles then results in correlated motion of the azimuthally bunched electrons, driving emission or absorption of the extraordinary magneto-ionic wave mode. Net emission requires a source of free energy such that particles transferring energy to the wave outweigh the particles removing energy through absorption. The source of free energy in ECMI is an anisotropy in the electron velocity distribution $f(v)$ with a positive gradient in velocity $\partial f(v)/\partial v > 0$, leading to a maser instability that drives 100 % circularly polarised coherent emission near the cyclotron frequency and its harmonics (Treumann 2006).

Two common anisotropies in astrophysical sources of ECMI are the *loss-cone* and *horseshoe* distributions. The loss-cone distribution has a deficiency of electrons with velocity parallel to the magnetic field $v_\parallel$, and is typically formed due to the loss of electrons with low pitch angle α during reflection at a magnetic mirror in

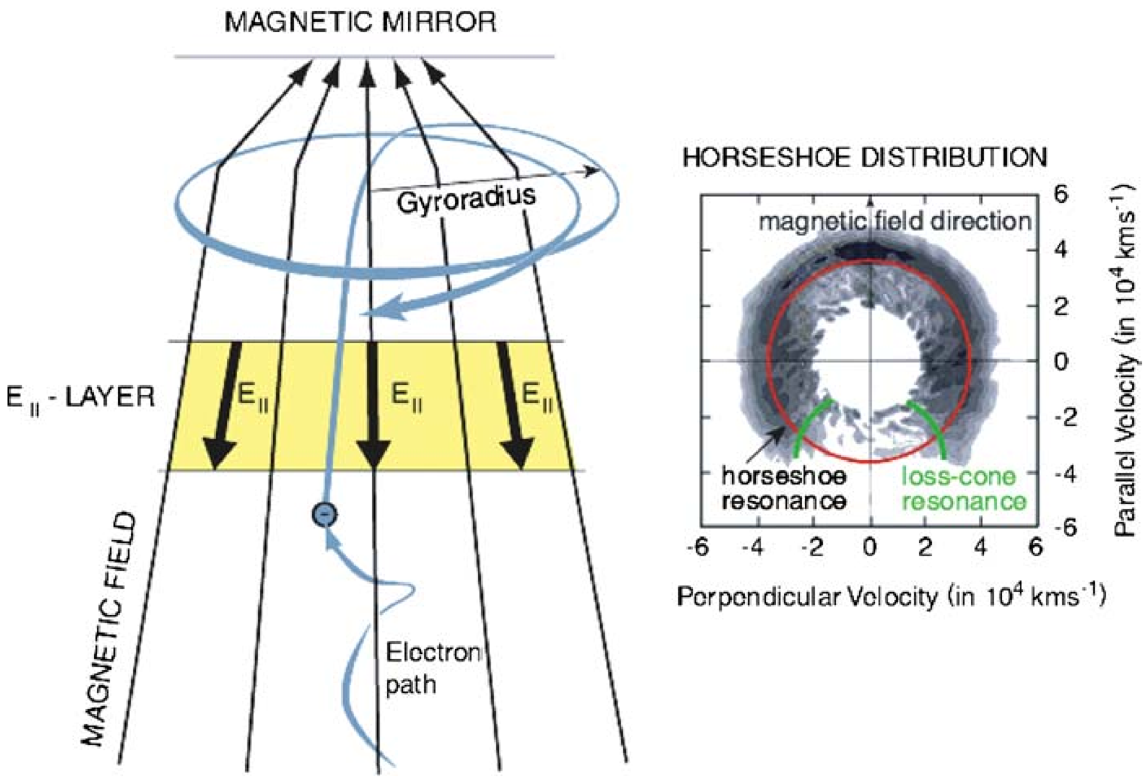

Figure 1.2: Left: Schematic of the development of a horseshoe electron velocity distribution. Electrons travelling along a converging magnetic field are first accelerated by a field aligned potential and develop a ring-shell distribution with a deficiency in low-velocity electrons, and are then reflected by a magnetic mirror formed by the converging field developing a one-sided loss-cone. Right: Velocity phase-space diagram of a ring-shell distribution with a one-sided loss cone. Resonance ellipses with maximal $\partial f(v)/\partial v > 0$ contributions are shown in red for the ring-shell component and green for the loss-cone component. Image credit: Treumann (2006).

a region of increasing magnetic field strength, such as the converging field lines in a dipole field or the footprint of a magnetic flux tube. Here conservation of the magnetic moment $\mu = m_e v_\perp^2/2B$ results in transfer of momentum from parallel to perpendicular velocity $v_\perp$ to balance the increasing field strength B. Electrons with a low velocity pitch angle $\alpha = \tan^{-1}\left(v_\perp/v_\parallel\right)$ are able to retain sufficient $v_\parallel$ to impact with the atmosphere[2] and are lost, while electrons with pitch angle greater than the loss-cone angle α_L are reflected and hence form a one-sided loss-cone distribution with a deficiency of $v_\parallel$ electrons in the upward direction. A positive gradient in the velocity distribution is therefore produced as electrons with excess gyromotion relax into the loss-cone. The horseshoe distribution is a combination of a one-sided loss-cone distribution with a *ring-shell* distribution, in which electron velocities form a circular ring shape in $v_\parallel - v_\perp$ space due to particle acceleration by a field aligned electric potential (Treumann 2006). Schematics showing the development of a loss-cone and horseshoe distribution are pictured in Figure 1.2.

[2]Generally the ionosphere in a planetary context, and chromosphere in a stellar context.

The condition defined by Equation (1.16) represents an ellipse in $v_\parallel - v_\perp$ space centred on $v_\parallel = \omega c N/\omega_e \cos\theta$ where N is the parallel refractive index, and traces the particle velocities capable of resonance with a wave mode of a particular frequency (Hess et al. 2008). The absorption coefficient for ECMI at that frequency is then determined by integrating over the electron velocity distribution along the ellipse, with the weighted contribution of $\partial f/\partial v$ determining whether positive or negative absorption dominates, and where dominant negative absorption corresponds to a high growth rate of electromagnetic waves (Melrose & Dulk 1982). For a loss-cone distribution the resonance ellipse with maximal growth rate is offset in $v_\parallel$ to align with the loss cone edge where $\partial f/\partial v_\perp > 0$, and therefore carries a frequency dependent beaming angle

$$\theta = \arccos\left[\frac{v}{c}\left(1 - \frac{\omega_e}{\omega_{e,\max}}\right)\right], \tag{1.17}$$

where $\omega_{e,\max}$ is the cyclotron frequency at the mirror reflection point (Hess et al. 2008).

The horseshoe distribution growth rate is maximised for a resonance ellipse aligned just inside of the ring where $\partial f/\partial v > 0$ and centred at the origin where $v_\parallel = 0$. The emission pattern is therefore beamed at an angle $\theta = \pi/2$ independent of frequency. The horseshoe distribution leads to significantly higher growth rates than the loss-cone due to the larger number of particles that can contribute to wave growth.

1.1.6 Plasma Emission

The other coherent mechanism relevant to stellar radio emission is *plasma emission*, a process through which electromagnetic waves are excited by collective particle motion induced by the non-linear coalescence of electrostatic plasma waves (Ginzburg & Zhelezniakov 1958). The emission can be produced at the fundamental ω_p or second harmonic $2\omega_p$ of the plasma frequency, depending upon the specific wave-wave processes involved. In both cases the process begins with the generation of non-thermal Langmuir waves by an unstable electron beam—where higher velocity electrons overtake slower particles generating a two-stream instability, and pile up towards the front of the beam creating a positive gradient in the velocity distribution (Melrose 2009). This maser instability saturates through quasi-linear relaxation as the high velocity particles transfer energy to Langmuir waves and reach a marginally stable state. Wave growth then occurs stochastically as the wave distribution and electron beam encounter density fluctuations that perturb the instability, leading to a turbulent, non-thermal distribution of Langmuir waves (Robinson 1992).

The non-thermal Langmuir wave distribution may then lead to excitation of the magneto-ionic wave modes through two routes of non-linear wave-wave interaction (Melrose 1987). First, the generation of a transverse electromagnetic wave T may be achieved through either the coalescence of a Langmuir wave L and an ion acoustic wave S of appropriate wavelength and frequency in the interaction $L + S \rightarrow T$, or through the decay of a Langmuir wave in the interaction $L \rightarrow S + T$. Transverse waves in these scenarios are generated at the fundamental of the plasma frequency ω_p, and hence excite only the ordinary magneto-ionic mode. Secondly, the scattering of two oppositely directed Langmuir waves can produce a transverse wave in the process $L+L \rightarrow T$. The kinematic conditions of this interaction result in a transverse wave at the second harmonic $2\omega_p$, which is capable of exciting both the ordinary and extra-ordinary modes.

Plasma emission is therefore intrinsically 100 % left circularly polarised at the fundamental if directed somewhat aligned with the magnetic field in the source region, and 100 % right circularly polarised when anti-aligned—the opposite sense of polarisation to ECMI emission. Observationally the polarisation of Solar radio bursts attributed to fundamental plasma emission processes have lower than 100 % circular polarisation suggesting the emission becomes depolarised while propagating through the corona. This may occur due to coupling between the o-mode and x-modes as the wave scatters against plasma density gradients (e.g. Melrose 2006) or crosses transverse magnetic field regions en-route to the observer (e.g. Pacholczyk & Swihart 1970). As harmonic emission excites both modes the polarisation is generally mild in the sense of the o-mode, though propagation effects may similarly impart higher fractional polarisation.

1.2 Phenomenology of Stellar Radio Activity

The emission mechanisms described in the previous section can be driven by a wide variety of astrophysical phenomena occurring in stellar magnetospheres, which are distinct within different regimes of stellar effective temperature, rotation speed, magnetic field strength, plasma density, and age. Often magnetically driven radio activity is broadly separated into two paradigms—*Solar-type activity* that is driven by magnetic reconnection and is powered by plasma emission processes, and *auroral emission* that is driven by large-scale magnetospheric current systems and is powered by ECMI. In this section I briefly review the origin of strong magnetism in planets and stars, and the macroscopic processes that lead to the production of coherent radio emission in these environments.

1.2.1 Solar-type Radio Activity

Due to its proximity the Sun is naturally the most well studied radio star. A rich zoo of observable features and processes associated with the buildup and release of magnetic energy have been recorded at optical, ultraviolet, and X-ray wavelengths—such as sunspots, plages, coronal loops, Solar flares, and coronal mass ejections. Some of these processes are responsible for particle acceleration and enhancement of the Solar wind, causing dynamic plasma conditions in interplanetary space collectively referred to as *space weather*.

The generation of strong magnetic fields in the Sun and other main sequence stars is usually attributed to the $\alpha\Omega$ dynamo (Brandenburg & Subramanian 2005). In this model shear rotational flows at the tachocline—a transition region between the internal radiative zone and external convection zone—wind and amplify the field lines of an existing poloidal field into a toroidal configuration (the Ω-effect). Turbulent plasma motion induced by the coriolis force then reconfigures the toroidal field into an amplified poloidal field (the α-effect) (Parker 1955).

In recent years, modern radio interferometers and processing techniques such as tied array beamforming have provided a means to perform imaging spectroscopy (see Gary (2023) for a review) to track the time and frequency evolution of these features on the spatially resolved radio Sun. These techniques provide a means to measure properties of the local plasma environment such as effective temperature, magnetic field strength and orientation, and the distribution of electron energies, and tie the evolution of these parameters to the bulk motion of Solar features (e.g. Kontar et al. 2017; Bhunia et al. 2023).

The Quiet Sun

The Sun is a persistent radio source even in regions and periods with an absence of elevated magnetic activity, generally referred to as the *quiet Sun* (Smerd 1950). This emission is generated by thermal Bremsstrahlung emission driven by frequent Coulomb collisions between electrons in local thermodynamic equilibrium (Shibasaki et al. 2011). Due to the ν^{-2} dependence of Bremsstrahlung emission optical depth, radio observations probe different coronal altitudes as a function of frequency allowing a three dimensional picture to be formed of the coronal plasma environment (e.g. Aschwanden 1995; Vocks et al. 2018). Thermal Bremsstrahlung emission is difficult to detect from other stars due to the low brightness temperature of thermal emission, but has been detected at 8 GHz from the F5 sub-giant star Procyon by Drake et al. (1993), at 34.5 GHz from chromospherically active Solar-type stars by Villadsen et al. (2014), and at 9 and 21 GHz from the K0III giant Pollux by O'Gorman et al. (2017). The majority of quiescent stellar radio emission is generated by gyro-synchrotron emission, a feature unobserved on the quiet Sun.

Solar Radio Bursts

During periods of activity the Sun releases magnetic energy through a variety of processes, and generates non-thermal radio bursts that can be orders of magnitude brighter than the quiescent level. These bursts have been historically classified into five types, based upon their appearance in maps of intensity as a function of time and frequency known as *dynamic spectra* (Wild et al. 1963). Figure 1.3 shows a multi-instrument dynamic spectrum capturing a range of Solar radio bursts coincident with an X-ray flare (Morosan et al. 2019).

Type I bursts, also known as *spike bursts*, are short duration ($t \sim 1\,\mathrm{s}$) and narrowband ($\Delta\nu/\nu \sim 0.03$) that typically occur in groups accompanied by an increase in continuum background emission, referred to collectively as *Solar noise storms*. Solar noise storms are located above active regions at typical coronal altitudes of 0.2–0.5 $R_\odot$ and occur at frequencies of 50–500 MHz (Elgarøy 1977), with chains of individual bursts tending to drift from high to low frequencies over minute timescales (Mercier et al. 2015). Type I bursts are widely accepted to be powered by fundamental plasma emission, with both the burst and continuum components showing a

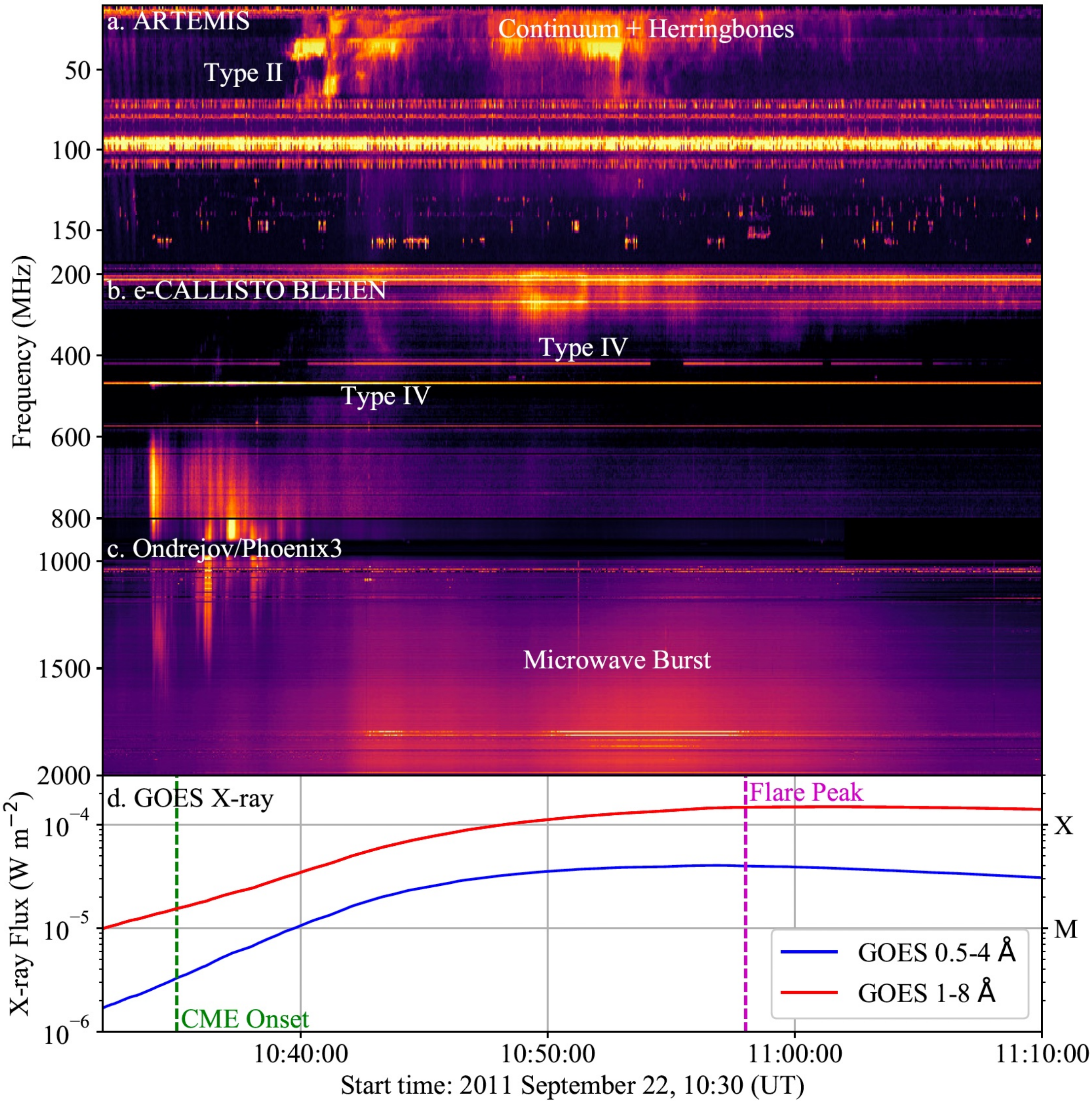

Figure 1.3:
Wideband dynamic spectrum showing a range of Solar radio burst activity following a CME, captured by the ARTEMIS-IV Radiospectrograph (Kontogeorgos et al. 2006), the Bleien dish in the e-CALLISTO network (Benz et al. 2005, 2009a), and the Ondrejov RT5 Spectrograph and Phoenix3 spectrometer (Benz et al. 2009b). Observed features include fundamental and harmonic type II bursts accompanied by herringbone structure at ∼50 MHz, type III bursts followed by a type IV burst at ∼300 MHz, and a long duration microwave burst at $\gtrsim$1 GHz. Image credit: Morosan et al. (2019).

high degree of circular polarisation in the sense of the ordinary magneto-ionic mode (Dulk et al. 1984; McCauley et al. 2019). However, the source of free energy driving the generation of plasma waves is debated. The two predominant theories involve either ongoing minor magnetic reconnection events (Melrose 1980; Benz & Wentzel 1981) which may occur at open-closed field line boundaries near active regions (e.g. Del Zanna et al. 2011; Mandrini et al. 2015), or the emergence of magnetic flux tubes from beneath the photosphere, driving shocks that power the emission (Spicer et al. 1982; Li et al. 2017).

Type II bursts are widely accepted to be associated with the formation of energetic electron beams and Langmuir waves by magnetohydrodynamic shocks, which propagate through the corona generating plasma emission (Cairns et al. 2003). They appear in dynamic spectra as a pair[3] of bands at the fundamental and second harmonic of the local plasma frequency that drift slowly ($\sim$1 MHz s^{-1}) from high to low frequency as the shock moves from regions of higher to lower plasma density. The shocks driving type II bursts are generally accepted to be caused by coronal mass ejections (CMEs) (Gopalswamy 2006), though it is possible some are associated with stellar flare blast waves (e.g. Claßen & Aurass 2002; Morosan et al. 2023). With an assumed coronal density model the burst drift rate can be mapped to a shock velocity, with typical speeds of $\sim$1000 km s^{-1} in agreement with that of CMEs observed with white light coronagraphs (Webb & Howard 2012).

In some type II bursts the fundamental and harmonic bands individually split into multiple sub-bands, which may be explained by simultaneous plasma emission from ahead of and behind the shock front, additionally providing a diagnostic of the shock strength and local magnetic field strength (Smerd et al. 1975). Type II bursts are usually only weakly polarised ($f_{CP} < 5\,\%$) despite a component being generated by fundamental plasma emission that is usually highly circularly polarised (e.g. Komesaroff 1958; Ramesh et al. 2022). However, some type II bursts show circularly polarised fine structure known as *herringbones*, appearing as short, fast drifting bursts extending above or below the main bands (Cairns & Robinson 1987).

Multiple searches have been conducted for type II emission from magnetically active M-dwarf stars (e.g. Crosley et al. 2016; Crosley & Osten 2018a,b; Villadsen & Hallinan 2019) though none have been detected to date. This is plausibly due to the much stronger magnetic fields in these systems that cause confinement of CME ejecta (Alvarado-Gómez et al. 2020), suppress the formation of shocks in the high Alfvén speed plasma (Mullan & Paudel 2019), or only allow their formation at such low coronal densities that the type II emission occurs at frequencies below the ionospheric cutoff at $\sim$10 MHz.

Type III bursts are short in duration (0.1–10 s) and drift in frequency at a much faster rate than type II bursts ($\sim$100 MHz s^{-1}). They are driven by mildly relativistic electron beams travelling along magnetic field lines at velocities of $v \sim 0.1$–0.6 c (Klassen et al. 2003), which develop instabilities that generate both fundamental and harmonic plasma emission. Type III bursts are associated with magnetic reconnection events and often accompanied by emission at optical and X-ray wavelengths (Kundu et al. 1995; Winter & Ledbetter 2015). Bursts accompanying large Solar flares can begin in the >0.5 GHz range (e.g. Benz et al. 1992) drifting down to a lower frequency cutoff of $\sim$100 MHz, and map to closed field lines that confine the electron beams to the inner magnetosphere. Other so called *inter-planetary* type III bursts occur on open field lines, beginning at frequencies of <300 MHz and drifting down to the $\sim$10 kHz range observable by space-based instruments (e.g. Reiner et al.

[3] occasionally a third band at the third harmonic is seen (e.g. Zlotnik et al. 1998).

1995; Krupar et al. 2018). See (Reid & Ratcliffe 2014) for a comprehensive review of type III bursts.

Type IV bursts are wideband continuum emission that typically follow energetic flares and coronal mass ejections. They occur in two varieties: *stationary* type IV bursts are thought to be driven by electrons spiralling along post-eruption loops generating gyro-synchrotron emission, while *moving* type IV bursts are associated with particle acceleration as magnetic fields are reconfigured in the wake of a CME, and can feature up to 100 % circular polarisation and high brightness temperature (Cliver et al. 2011).

Despite plasma emission and gyrosynchrotron emission driving the majority of Solar radio bursts, highly circularly polarised Solar spike bursts are occasionally observed accompanying the hard X-ray bursts following Solar flares, and have been attributed to ECMI driven by a horseshoe distribution (Cliver et al. 2011; Melrose & Wheatland 2016; Ning et al. 2021). The presence of both coherent mechanisms acting in the conditions of the Solar corona highlights the importance of local plasma conditions in determining the mechanism by which the release of magnetic energy is converted to radio emission. Further, the extreme variety of plasma conditions in stellar atmospheres is suggestive that the existing Solar radio burst classification scheme is not necessarily applicable to radio bursts from other stars, particularly in systems hosting significantly stronger magnetic fields.

1.2.2 Planetary Radio Emission

Each of the planetary magnetospheres in our Solar system have distinct plasma environments with a rich variety of interactions leading to the production of radio emission. Although the focus of this thesis is on stellar radio emission, it is useful to review these processes as analogous environments exist in the magnetospheres of cool stars.

The Earth's magnetosphere consists of a primarily dipolar magnetic field, which is reconfigured through interaction with the Solar wind into a complex organisation of current systems and non-thermal plasma environments (Borovsky & Valdivia 2018). As the Solar wind approaches the Earth, magnetic reconnection occurs between the wind-carried inter-planetary magnetic field and the dayside magnetopause—accelerating particles and carrying newly formed open field lines around the magnetosphere and into the magnetotail. This extended structure consists of a northern and southern lobe of open field lines separated by a current sheet, where nightside reconnection closes the field lines, energising and injecting particles back into the inner magnetosphere.

This process is known as a *Dungey cycle* (Dungey 1961), and is responsible for driving the dynamics of a variety of non-thermal plasma environments—such as the Van-Allen radiation belts that trap high energy particles (Li & Hudson 2019), and the ion and electron plasma sheets that are the source of auroral processes (Borovsky et al. 1998). Energetic particles travel from these environments along magnetic field lines of increasing strength which form a magnetic mirror, causing high pitch angle particles to reflect back into the magnetosphere while low pitch angle particles precipitate into the atmosphere, ionising atmospheric gases and producing the visible *aurora australis* and *aurora borealis* (Evans & Moore 1979). The population of reflected electrons then has a loss-cone velocity distribution, which is formed into a horseshoe distribution by field aligned electric fields in auroral density cavities (Pottelette et al. 1999; Ergun et al. 2004). This is the source of free energy that drives the auroral kilometric radiation (AKR), a highly beamed low frequency radio emission at 100–300 kHz powered by the electron cyclotron maser .

Auroral radio emission is also produced by the other magnetised planets in the Solar system, with the magnetic field dependence of ECMI producing higher frequency emission from the stronger magnetospheres of Jupiter, Saturn, Uranus, and Neptune (Zarka 1998). Jupiter is by far the most dominant magnetic influence in the Solar system other than the Sun, with a field strength 10 000 times greater than the Earth and a magnetotail extending out to the orbit of Saturn (Desch & Rucker 1983). The large scale and strength of the magnetosphere prevents efficient transport of energy by interaction with the Solar wind—and rather than Dungey cycles, rapid planetary rotation and a steady source of plasma from the volcanic moon Io are the primary drivers of plasma dynamics. Io's frequent volcanic activity loads the Jovian magnetosphere with plasma which then co-rotates with the Jovian magnetic field due to a torque induced by currents coupling the ionosphere and magnetosphere (Hill 1979). At distances greater than $\sim$20 R_J from the planet co-rotation begins to break down, as the ionospheric currents are unable to supply sufficient torque to balance the increasing angular momentum of outward plasma diffusion (Cowley & Bunce 2001).

This process supplies the middle and outer Jovian magnetosphere with plasma where large radiation belts produce broadband synchrotron emission (Bolton et al. 2002). The region over which co-rotation breaks down is also the source of a field aligned current that directs electrons along field lines mapping to a narrow oval surrounding Jupiter's polar cap. Field aligned voltages accelerate low pitch angle electrons into the Jovian atmosphere generating bright infra-red, ultraviolet and x-ray auroral emissions (Saur et al. 2003; Mauk & Saur 2007; Grodent et al. 2018). The reflected, upward moving electrons are then left with a loss-cone velocity distribution (Kurth et al. 2017; Louarn et al. 2017) that drives the ECMI producing the auroral decametric (DAM) and hectametric (HOM) radio emission.

Jupiter also features auroral emissions driven by electrodynamic interaction with each of the Galilean moons—with interactions induced by Io, Europa, and Ganymede (e.g. Louis et al. 2023), and to a lesser extent Callisto (e.g. Menietti et al. 2001)—as each satellite intercepts the flow of co-rotating plasma with a relative velocity lower than the Alfvén speed. This *sub-Alfvénic interaction* generates Alfvén waves that propagate upstream of the disturbance along magnetic flux tubes connecting to the Jovian polar caps, carrying energy from the interaction and accelerating particles into a field aligned current. As with the main auroral oval, the electron distribution attains a loss-cone distribution by reflecting in the magnetic mirror formed by the increasing magnetic field and produce ECMI driven auroral radio emission.

Both in-situ measurement of the plasma environment (e.g. Louis et al. 2017, 2023) and high-resolution ground based observations (e.g. Ryabov et al. 2014) have revealed bursts with a wide range of fine structures, durations, and frequency drift patterns. The emissions are broadly classified based on the auroral engine they are driven by (e.g. Io / non-Io), and by the time and frequency characteristics as long (L), short (S), or narrowband (N) bursts. Io has the strongest interaction with Jupiter, and produces decametric radio bursts with a distinct arc shape in dynamic spectra due to the frequency dependent beam geometry (Hess et al. 2008).

Figure 1.4 shows an overview of the Jovian aurorae captured by instruments across the electromagnetic spectrum, with infra-red images of the Io volcano distribution and southern auroral oval from the JIRAM detector onboard the *Juno* spacecraft, an ultraviolet image of the northern auroral oval from the UVOT instrument on the Neil Gehrels *Swift* Observatory, and radio frequency dynamic spectra of auroral emissions captured by he Ukrainian UTR-2 decameter array (Ryabov et al. 2014).

In recent years there has been a strong effort to detect radio emission from a scaled up version of the Jupiter-satellite interaction in other star systems, either by the interaction between a strongly magnetised planet and its moons or a star and close-in exoplanet. This phenomenon is broadly referred to as *star-planet interaction* (SPI), and could present a distinct exoplanet detection method that complements the biases inherent to standard radial velocity and transit method searches, and may also provide the means for the first detection of exo-moons. To date several studies have claimed hints of SPI through the detection of coherent auroral pulses (Vedantham et al. 2020a; Pineda & Villadsen 2023), though stellar magnetic activity unassociated with planetary systems is also capable of explaining these detections and more evidence is required. The hall-mark signature of SPI as seen in the Jupiter-Io interaction is the modulation of auroral pulses at a period distinct from the rotation period, though the beamed auroral pulses can often have a complex morphology in dynamic spectra that introduces structure to the lightcurve (Kavanagh & Vedantham 2023). A robust identification of SPI will therefore require the comparison of observations with modelling of both the electrodynamic engine driving the emission (e.g. Saur et al. 2013; Nichols & Milan 2016; Turnpenney et al. 2018, 2020) and the observable features associated with the auroral source configurations produced by those engines (e.g. Hess et al. 2008; Hess & Zarka 2011; Kavanagh et al. 2021; Kavanagh & Vedantham 2023).

1.3 Review of Radio Star Surveys

1.3.1 Targeted Surveys

Historically the majority of stellar radio studies have relied on targeted observations of stars selected on the basis of previously known magnetic activity. In this section I review the results of targeted surveys of various sub-populations of radio stars—highlighting their strengths in tracing local plasma conditions and the factors driving stellar radio activity and their shortcomings in studying of large samples.

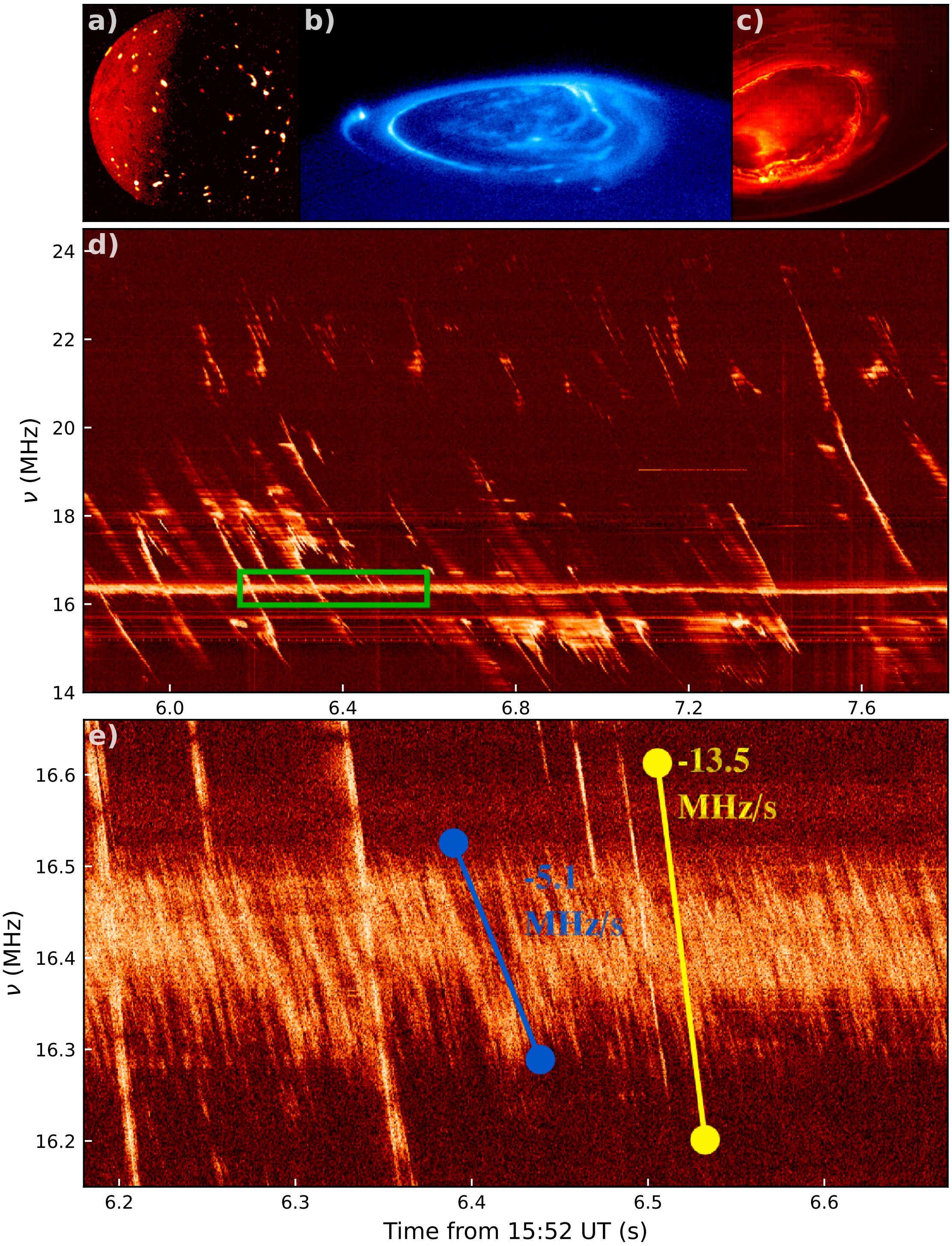

Figure 1.4: Multi-wavelength view of the Jovian aurorae. *a) Juno* JIRAM infra-red image of volcanic hotspots on Io. *b) Swift* UVOT ultra-violet image of the northern auroral oval, with Io hotspot visible to the left. *c) Juno* JIRAM infra-red image of the southern auroral oval. d) Ukrainian UTR-2 decameter array dynamic spectrum of an S-burst storm driven by Io on 2008-10-30, showing a variety of auroral radio bursts. e) Zoomed in section of d) with multiple fast drifting S-bursts visible on top of an L-burst. Image credit: *a)/b)/c)* NASA/ESA, *d)/e)* Ryabov et al. (2014).

Flare Stars and Solar-type Activity

In the 1980s and 1990s stars with strong X-ray emission or optical flaring were targeted by numerous surveys, some of which established important metrics that have persisted in the radio star literature for decades. Güdel (1992) conducted an 8.5 GHz survey with the Karl G. Jansky Very Large Array (VLA) of 12 K-dwarf systems with strong emission in X-rays and chromospheric Ca II lines, and detected seven stars. These results show a strong correlation between the radio and non-simultaneous X-ray luminosity. Güdel et al. (1993) surveyed 21 M-dwarfs using the VLA at 5 and 8.5 GHz and simultaneous X-ray monitoring with *ROSAT*, and detected 17 stars, revealing a similar radio and X-ray luminosity correlation. Güdel & Benz (1993) extended this relation to encompass magnetically active main-sequence stars from type F to M and interacting binary systems, and Benz & Güdel (1994) showed the correlation holds across the full luminosity range of Solar flares. This correlation between 5 GHz radio luminosity L_ν and X-ray luminosity L_X follows the relationship $L_X \approx 15.5\,\mathrm{Hz} L_\nu$—now known as the Güdel-Benz (hereafter GB) relation. This relationship is understood to derive from a common acceleration mechanism driving the partition of energy into emission in both bands. In this model, magnetic reconnection accelerates electrons that radiate non-thermal gyrosynchrotron emission and heats coronal plasma resulting in thermal X-ray emission.

Jackson et al. (1987) and White et al. (1989) surveyed all known flare stars within 10 pc (Gurzadyan & Terzian 1980) with the VLA at 1.5 and 5 GHz and detected nine out of the 29 targeted systems. Combining previous VLA observations in the literature they found a radio activity fraction of ∼40 % among stars that demonstrate optical flaring and chromospheric line emission (dMe/dKe) and a much lower fraction of ∼5 % among stars with low activity (dM/dK), concluding that the radio emission of K- and M-dwarfs is primarily associated with optical and chromospheric activity. However the observations in this sample varied significantly in duration with some observations as short as 15–20 min, and were therefore only sensitive to emission from extremely active stars that may not represent the wider population.

In recent years several radio studies of magnetically active M-dwarfs have focused on the search for indicators of extrasolar space weather. M-dwarfs are the most abundant type of star and should therefore host the majority of exoplanets in the Galaxy (Golovin et al. 2023)—though the habitable zones in these stars are much closer, and the energy released in optical and X-ray flares orders of magnitude greater than the Sun (Yang et al. 2017). Targeted radio searches have therefore aimed to detect and quantify the impact of space weather events such as coronal mass ejections on the conditions for planetary habitability in these systems.

Osten & Bastian (2006) surveyed the active M-dwarf AD Leo with the Arecibo telescope at 1.3 GHz and detected two highly circularly polarised, coherent radio bursts. One burst showed variability on 30 ms timescales and rapid frequency drifts with similar morphology to type III spike bursts observed in the low Solar corona, and was attributed to fundamental plasma emission. The other showed slower variation and frequency drift, plausibly representing a disturbance propagating through the corona. In a followup study of AD Leo Osten & Bastian (2008) conducted high time resolution observations with Arecibo capturing a 45 s long highly circularly polarised burst composed of multiple striated sub-bursts occurring over ∼2 ms timescales. The authors attributed this burst to the electron cyclotron maser due to the observed rapid positive and negative frequency drifts, indicating that both coherent emission mechanisms can be active in the same star.

Lynch et al. (2017b) targeted the prototypical flare star UV Cet for 9 h with the Murchison Widefield Array (MWA; Bowman et al. 2013; Tingay et al. 2013) at 154 MHz identifying four coherent, elliptically polarised bursts that they attributed to the electron cyclotron maser, with a potential periodicity consistent with the stellar rotation period. Later observations of UV Cet by Zic et al. (2019b) with the Australian Square Kilometre Array Pathfinder (ASKAP; Johnston et al. 2008; Hotan et al. 2021) at 888 MHz detected multiple elliptically polarised pulses with a periodicity matching the stellar rotation period, interpreting the pulses as ECMI driven auroral emission produced in a density cavity within the corona. Bastian et al. (2022) observed UV Cet with the MeerKAT telescope from 544–1712 MHz resolving fine structure in the auroral pulses, explained by the frequency dependent beaming of an auroral active region swept through the line of sight. These observations highlighted the presence of auroral activity in a star well-known for optical flaring (Lacy et al. 1978) and stochastic radio bursts (Villadsen & Hallinan 2019), demonstrating that the regimes of auroral and solar-type radio activity are not mutually exclusive in cool stars.

In a search for type II bursts associated with coronal mass ejections Crosley et al. (2016) conducted a 15 h survey of the active M-dwarf YZ CMi with the Low Frequency Array (LOFAR; van Haarlem et al. 2013) from 10–190 MHz with no detections. Crosley & Osten (2018a) targeted the active M-dwarf EQ Peg for a total of 44 h with the VLA at 370 MHz identifying two transient outbursts, but neither showed features in common with type II bursts. Zic et al. (2020) conducted simultaneous optical and radio observations of Proxima Centauri with ASKAP at 950 MHz and detected a bright, elliptically polarised radio burst coincident with an optical flare, followed hours later by broadband radio emission resembling a type IV Solar radio burst indicative of a coronal mass ejection.

Villadsen & Hallinan (2019) performed a 58 h targeted survey of five magnetically active M-dwarfs with the VLA from 0.22–6 GHz searching for the radio signature of a coronal mass ejection. Through dynamic spectroscopy they identified 22 coherent radio bursts with a diverse range of features in the time-frequency plane that are distinct from the Solar radio burst classification scheme. The duty cycle of detected bursts in this study peaks at ∼10 % at a frequency of 1–1.4 GHz, falling at lower and higher frequencies. However both of these properties may only be representative of the small sample targeted in the survey. The five targeted M-dwarfs all demonstrate high levels of optical, X-ray, and chromospheric emission line activity, and are also among the most radio active M-dwarfs in the Solar neighbourhood. This sample is therefore likely to over-represent the duty cycle of radio activity among the general M-dwarf population. The peak frequency of the duty cycle is also representative of the coronal properties of the targeted stars, and larger samples encompassing the full range of M-dwarf magnetic field strength and plasma density are needed to place robust constraints on the frequency dependence of M-dwarf radio activity.

Close and Interacting Binary Systems

Close binary systems are among the brightest and most active radio stars at frequencies of $\sim$1 GHz, producing both non-thermal quiescent emission and frequent flares. These systems have short orbital periods of 1–30 d and low binary separations of $\sim$0.01 AU causing the component stars to be tidally locked and resulting in rapid stellar rotation. These systems therefore tend to have prominent indicators of magnetic activity with strong X-ray and chromospheric line emission. The close binary nature of these systems can also result in the coupling and interaction of the stellar magnetospheres, resulting in complex magnetospheric configurations (Uchida & Sakurai 1985), large starspot covering fractions (Berdyugina & Tuominen 1998), and strong reconnection driven radio flares. RS Canum Venaticorum (RS CVn) is the prototypical system for variables in this class with detached components, while Algol is the prototype for semi-attached systems that fill their Roche lobe.

Close binaries are also known to produce coherent, highly circularly polarised bursts. In observations with the Westerbork Synthesis Radio Telescope (WSRT) van den Oord & de Bruyn (1994) of the RS CVn binary II Peg van den Oord & de Bruyn (1994) detected coherent flares at 360 and 609 MHz. They attributed the lower frequency burst to plasma emission but found the presence of $\sim$100 % circular polarisation in the 609 MHz flare difficult to explain, rejecting ECMI on the basis of the weak implied magnetic field strength. Slee et al. (2008) conducted high-time resolution observations of the RS CVn binary HR 1099 with the Australia Telescope Compact Array (ATCA) at 1.4 and 2.4 GHz, and identified two 100 % circularly polarised bursts lasting 2–3 h with structure evident on timescales of 78 ms. The authors suggested the coherent bursts may be driven by an auroral process, in which strong stellar winds from the K2 subgiant inject energetic plasma into the G5 dwarf magnetosphere and generate an ECMI source.

Morris & Mutel (1988) conducted a survey of 103 RS CVn binary systems at 5 GHz with the VLA and detected 53 systems, placing constraints of $\lesssim 10^{15}$ erg s^{-1} Hz^{-1} on the median 5 GHz radio luminosity of this population. Drake et al. (1989) surveyed a further 77 RS CVn systems and incorporated the Morris & Mutel (1988) sample into a total sample of 122 RS CVn binaries observed with the VLA at 5 GHz (Morris & Mutel 1988; Mutel & Lestrade 1985; Florkowski et al. 1985; Pallavicini et al. 1985; Drake et al. 1986), and reported detection of 66 systems with most detected more than once. They found strong correlations between the 5 GHz radio luminosity and Ca II H and K line emission, and between radio luminosity and non-simultaneous X-ray luminosity. The radio X-ray correlation was later discovered to span a wider range of stars, and is now known as the Güdel-Benz relation Güdel & Benz (1993); Benz & Güdel (1994).

Auroral Emission from Low-mass Stars

Stars of spectral type later than M3 are fully convective and lack the internal temperature required to support a radiative zone (Jao et al. 2018), and hence the $\alpha\Omega$

dynamo cannot operate. Stellar magnetic activity indicators such as X-ray and chromospheric emission begin to decline for stars beyond this boundary (Mohanty et al. 2002; Berger et al. 2010), and yet strong magnetic fields are nonetheless revealed in these cool stars by intense radio emission (Berger 2006). The precise dynamo process responsible for the magnetic fields of fully convective objects is still an open question, but the α^2 dynamo—in which turbulent motions alone are able to generate and self-sustain a global field—is a leading model (Chabrier & Küker 2006). Fully convective stars typically possess a dipolar magnetic field configuration on large scales, with the majority of magnetic flux concentrated in smaller scale, chaotic field configurations (Kochukhov 2021). Some mid M-dwarfs have shown evidence of stable magnetic field configurations over decades long timescales (e.g. Kellett et al. 2002; Vida et al. 2016) in contrast to the magnetic reversals observed on the Sun, while later type stars are found in both strong poloidal and weakly magnetic toroidal configurations, perhaps indicating the presence of activity cycles (Morin et al. 2010).

Stars of spectral type M7 onwards are collectively named *ultracool dwarfs* (UCDs) and extend through the later L and T spectral types. These spectral types also encompass *brown dwarfs*—objects that are massive enough to initiate deuterium fusion (stellar mass $M \gtrsim 13\,\mathrm{M_J}$) but too small to initiate hydrogen burning ($M \lesssim 75\,\mathrm{M_J}$) in their cores (Spiegel et al. 2011). UCDs have been the focus of targeted surveys since the unexpected discovery by Berger et al. (2001) of both quiescent and flaring radio emission from a brown dwarf—orders of magnitude brighter than expected from the GB relation. Berger (2002) conducted a followup survey of 12 UCDs with the VLA at 8.5 GHz resulting in three detections, and Berger (2006) compiled a sample of 90 stars from M5 to T8 with a total of nine detections, establishing an activity fraction among ultracool dwarfs of ∼10 %. Burgasser & Putman (2005) surveyed seven UCDs with ATCA at 5 and 8 GHz with two detected in quiescent emission, and one UCD producing a bright, 100 % circularly polarised coherent pulse.

In 5 and 8.5 GHz VLA monitoring of an L3.5 brown dwarf candidate spanning 3 yr, Berger et al. (2005) detected variable ∼60 % circularly polarised radio emission with a periodicity of 3 h. Hallinan et al. (2006) conducted 5 and 8.5 GHz observations of an M9 dwarf previously detected by Berger (2002), discovering faint periodic radio emission in agreement with the estimated stellar rotation period of 2 h. Further 8.5 GHz observations with the VLA by Hallinan et al. (2007) and Hallinan et al. (2008) identified bright, 100 % circularly polarised pulses repeated in three stars, each repeated at the stellar rotation period and attributed to a coherent emission mechanism. These studies placed UCD radio emission within the context of an auroral radio emission model—in which the ECMI drives persistent radio emission beamed into a hollow cone, which is then modulated by stellar rotation that periodically sweeps the emission cone into the observer line of sight.

While auroral emission is typically confined to high latitude regions of dipolar planetary magnetospheres, the more complex magnetic field configuration of ultracool dwarfs can result in more varied auroral source distributions. Lynch et al. (2015) observed two UCDs with the VLA at 5 and 7 GHz and identified three periodic pulses in each band. Through modelling of the pulse properties in dynamic spectra, the authors found agreement with an auroral source distributions originating in the footprints of coronal magnetic loops in multipolar, non-axisymmetric global magnetic fields.

McLean et al. (2012) surveyed a sample of 104 M- and L-dwarfs with the VLA at 8.5 GHz for 1 h each and detected four stars. Compiling these results with the literature the authors presented a sample of 167 UCDs with radio observations and measured rotation rates, and showed that in contrast to other magnetic activity indicators rapid rotation is still an important component of the radio activity in fully convective stars. A few volume limited surveys of UCDs have also been conducted—Antonova et al. (2013) surveyed 32 UCDs within 20 pc using the VLA at 5 GHz, but made no detections, and Lynch et al. (2016) targeted 15 UCDs within 10 pc with ATCA at 5.5 and 9 GHz detecting three stars. The majority of UCD radio studies have so far been conducted above 5 GHz where ECMI probes magnetic field strengths of >3.5 kG, leaving lower frequency bands relatively uninvestigated. Lower frequency surveys are sensitive to either higher coronal altitudes where the fields of strongly magnetised stars decline, or may probe deeper into the corona in stars with weaker field strengths. Zic et al. (2019a) surveyed nine UCDs with the Giant Metrewave Radio Telescope (GMRT) at 610–1300 MHz, detecting quiescent gyrosynchrotron emission from two stars with signs of a spectral turnover.

The low detection rates in these surveys are broadly in agreement with the 10 % activity fraction established by Berger (2006), and may represent a multitude of factors. These include the prevalence of strong magnetic fields and auroral current systems in the UCD population, geometric factors such as the relative alignments of rotation and magnetic axes which may cause the emission beam pattern to be directed away from the line of sight, and the longevity of active auroral regions which may be intrinsically variable.

In 5 and 8.5 GHz VLA observations Berger et al. (2009) detected auroral pulses accompanied by Hα emission produced in the stellar chromosphere, both showing periodicity at the stellar rotation period. Simultaneous observation of these separate magnetic probes allowed constraints on the global magnetospheric configuration. Hallinan et al. (2015) targeted the auroral pulsing M8.5 dwarf LSR J1835 with simultaneous monitoring of Hα and radio observations at 4.5 and 7 GHz with the VLA. They detected auroral radio pulses varying in phase with the Hα emission modulated by stellar rotation, attributed to enhanced Hα emission at the deposition site of auroral electrons in the brown dwarf atmosphere. Motivated by this relationship, Kao et al. (2016) surveyed a sample of six late L/T-dwarfs with the VLA from 4–8 GHz, selected on the basis of previously detected Hα emission or optical/IR variability. They detected quiescent emission from five out of the six targets and auroral pulses from four, demonstrating a significant increase in detection rate compared to the $\sim$10 % rate, and further reinforcing the association between radio and optical auroral emissions observed in planetary magnetospheres.

Recently the source of quiescent emission accompanying aurorally active UCDs has been the subject of multiple high angular resolution very long baseline interferometry (VLBI) observations. Climent et al. (2023) and Kao et al. (2023) both conducted VLBI observations of LSR J1835 with the European VLBI Network (EVN) at 5 GHz and the Very Long Baseline Array (VLBA) at 8.4 GHz respectively, detecting both quiescent emission and auroral pulses. Both studies resolved the quiescent gyrosynchrotron emission into a double-lobed structure separated by 18 stellar radii and aligned equatorially with the magnetic and rotation axes. These observations placed the quiescent emission associated with aurorally active UCDs in the context of large-scale radiation belts analogous to the Van Allen radiation belts surrounding Earth and Jupiter, in contrast to the reconnection driven quiescent emission produced in the coronae of magnetically active stars.

Selection Biases

Targeted surveys have provided the sensitivity and extended monitoring time necessary to identify the microphysics involved in emission from individual stars, helping to form a picture of the connection to other stellar parameters such as mass loss (e.g. Aarnio et al. 2012), stellar rotation (e.g. McLean et al. 2012), magnetic field configuration (e.g. Berger et al. 2009), and multi-wavelength activity (e.g. Berger et al. 2010). These observations have also helped to constrain models of the complex interaction of these parameters in the evolution of stellar magnetism and mass loss. However the majority of these studies targeted stars on the basis of known emission at optical or X-ray wavelengths, the presence of chromospheric line emission, or prior known radio activity. Inferred statistical properties such as the activity fraction of a given stellar class (e.g. White et al. 1989) and burst rate and luminosity distributions (e.g. Villadsen & Hallinan 2019) are therefore difficult to extrapolate to the general population.

Targeted surveys are also not ideal for the discovery of new regimes of stellar radio activity, as limited telescope resources are unlikely to be allocated to speculative programs without strong detection prospects. The initial discovery of UCD radio emission by Berger et al. (2001) was prompted by detection of an X-ray flare (Rutledge et al. 2000), and subsequent targeted surveys of these systems have primarily focused on the 5–8 GHz range, while recently auroral radio emission has been discovered from ultracool dwarfs at lower frequencies (Vedantham et al. 2020b, 2023; Rose et al. 2023) that is unassociated with X-ray emission. Current searches for SPI are particularly vulnerable to such selection biases, and unbiased widefield surveys will be an important component in making the first robust identification of these rare systems.

Finally, targeted surveys require a large allocation of telescope resources that are prohibitive for the identification of large samples. For example, Bower et al. (2009) surveyed 172 M-dwarfs within 10 pc with the VLA at 5 GHz for ∼10–20 min each as part of a program to search for exoplanets through their gravitational influence on the stellar astrometry. The VLA search resulted in the detection of 29 stars, and a subset of the seven brightest stars was selected for high angular resolution observations with the VLBA. These observations detected five stars in all three epochs with no signatures of acceleration, excluding the presence of 3–6 M_J planets within 1 AU. In contrast, modern widefield radio telescopes are capable of monitoring multiple candidates simultaneously in a single telescope pointing, allowing deeper sensitivity thresholds compared to a targeted survey and increasing the capacity to identify high quality followup candidates.

1.3.2 Widefield Surveys

In contrast to the detailed studies enabled by targeted radio surveys, widefield surveys are an ideal tool for the compilation of large samples and serendipitous discovery of rare objects. While widefield surveys have been prolific in the production of large extragalactic source catalogues, historically it has been difficult to identify emission from radio stars through astrometric association to optical star catalogues alone. The radio sky is dominated by extragalactic radio sources—and coupled with the large surface density of optical stars, particularly at low Galactic latitudes, the likelihood of chance association between foreground stars and unrelated extragalactic radio sources is typically prohibitive for the angular resolution achieved by most widefield radio telescopes.

Helfand et al. (1999) conducted a search for radio stars in the VLA Faint Images of the Radio Sky at Twenty-cm (FIRST; Becker et al. 1995) survey at 1.4 GHz covering a 5000 deg^2 patch of sky to a sensitivity of 0.7 mJy PSF^{-1}. This search relied on association between unresolved radio sources and stars from multiple astrometric catalogues and resulted in 26 detections. Kimball et al. (2009) performed a search of FIRST through comparison to the Sloan Digital Sky Survey (SDSS; Adelman-McCarthy et al. 2008), and identified 112 matches between SDSS sources with stellar spectra and radio sources brighter than 1.25 mJy. However, the authors estimated a similar number of matches between unrelated SDSS stars and FIRST radio galaxies should be produced due to chance alignment. Driessen et al. (2023) performed a search for radio stars revealed by significant proper motion between four widefield surveys: FIRST, VLASS, and two epochs of the Rapid ASKAP Continuum Survey (RACS), an all-sky survey with ASKAP which has recently been completed at 888 MHz (RACS-low; McConnell et al. 2020) and 1368 MHz (RACS-mid; Duchesne et al. 2023). They detected eight radio stars with ASKAP using this method, including two that were not previously reported as radio loud, and demonstrated the effectiveness of proper motion as a secondary indicator of a stellar association.

1.3.3 Circular Polarisation Surveys

Purely astrometric association of radio sources identified in a widefield radio survey is unreliable due to the high surface density of active galactic nuclei and radio quiet stars in radio and optical surveys respectively. Therefore in order to reliably identify radio stars in widefield surveys a second indicator of stellar origin must be employed. As discussed in §§ 1.1 to 1.2 the radio emission from magnetised stellar and planetary atmospheres often features moderate to high degrees of circular polarisation. In contrast, the synchrotron emission produced by active galactic nuclei is typically only of order $\sim$0.1 % and at most $\sim$1–2 % circularly polarised (Stocke & Scott 1975; Macquart 2002). Widefield radio surveys in circular polarisation are therefore well-designed to distinguish between stellar and extragalactic radio sources, and are sensitive to the discovery of systems with unexpected radio properties that would otherwise not be included in targeted surveys.

Beyond radio stars and planets, pulsars are the other main population of radio source with significant circular polarisation (Johnston & Kerr 2018). These objects are usually discovered using time-domain search techniques that rely upon resolving pulse periodicity (Lorimer & Kramer 2004) and are therefore impacted by a range of intrinsic and propagation effects that blend or deform pulse profiles, such as extreme orbital dynamics and scatter broadening. Circular polarisation searches are sensitive to the polarised continuum emission of many integrated pulses rather than single pulse morphology, and are therefore well-suited to the discovery of pulsars in these environments (e.g. Kaplan et al. 2019; Wang et al. 2022b). Circular polarisation is also a prominent feature in more exotic radio transients such as magnetars (e.g. Kramer et al. 2007; Dai et al. 2019) and galactic centre radio transients (e.g. Wang et al. 2021; Hyman et al. 2021). Many of these objects are located towards the galactic plane and centre, where emission from diffuse structure complicates interferometric imaging—particularly on the short timescales on which source variability occurs—and limits attainable sensitivity through confusion. Circular polarisation searches are insensitive to diffuse galactic emission and are therefore an ideal discovery technique for galactic radio transients in general.

Despite the utility of circular polarisation for transient radio astronomy, until only recently widefield searches have been limited to total intensity or linear polarisation, primarily due to the impact of polarisation leakage introduced by uncertainty in the primary beam shape for existing widefield telescopes such as the Murchison Widefield Array (MWA; Tingay et al. 2013) (Sutinjo et al. 2015; Lenc et al. 2017). Lenc et al. (2018) conducted the first all-sky circular polarisation radio survey with the MWA at 200 MHz employing a novel polarisation leakage mitigation technique to reach a leakage of $\lesssim 1\,\%$, and identified 33 known pulsars and two tentative radio stars. The low yield in radio star detections may be attributed to the mosaicing of observations from separate nights in order to reach the sensitivity of $\sim$3 mJy PSF^{-1}. As meter wavelength stellar radio emission is typically transient on timescales of minutes to hours, bursts may only have been sampled over individual 2 min long snapshots and subsequently diluted through mosaicing with non-detections.

Recently the first widefield surveys with ASKAP have been completed in both total intensity and circular polarisation, providing the first opportunity for widefield circular polarisation searches at centimetre wavelengths where stellar radio activity has been suggested to peak (Villadsen & Hallinan 2019). Pritchard et al. (2021) conducted a circular polarisation search of RACS-low detecting 33 radio stars, 23 of which had not been previously identified as radio loud in the literature. In a circular polarisation search of RACS-mid Rose et al. (2023) discovered periodic auroral pulses from a T8 brown dwarf—the coldest object detected at radio frequencies to date. The Variables and Slow Transients (VAST) pilot survey (VASTP; Murphy et al. 2021) is a multi-epoch ASKAP survey of a subset of the RACS footprint, and has been completed in the 888 and 1368 MHz bands. Pritchard et al. (2024) conducted a circular polarisation search of the 888 MHz observations (VASTP-low) and made 196 detections of a sample of 43 radio stars, allowing constraints to be placed on the activity fraction of coherent M-dwarf radio bursts.

Circular polarisation searches have also been recently conducted as part of the LOFAR Two-meter Sky Survey (Shimwell et al. 2017; Callingham et al. 2023, LoTSS/V-LoTSS;) at 144 MHz. This survey has resulted in the discovery of a T6.5 brown dwarf (Vedantham et al. 2020b) and detection of periodic auroral emission from a T5.5/T7 binary (Vedantham et al. 2023), as well as samples of coherently emitting M-dwarfs (Vedantham et al. 2020a; Davis et al. 2021; Callingham et al. 2021a), close binaries (Toet et al. 2021), and magnetic chemically peculiar stars (Hajduk et al. 2022). As these low frequency detections of coherent stellar radio emission probe lower magnetic field strengths and plasma densities than ASKAP, targeted followup and comparison of these samples will aid understanding of the connection between stellar radio emission characteristics and varying regimes of stellar magnetism.

1.4 Overview of Thesis

Extensive study has been conducted of the non-thermal, magnetically driven radio emission associated with Solar radio activity and auroral current systems within the planetary magnetospheres of the Solar system. The rich variety of radio emissions from these environments trace fundamental plasma parameters, and provide a probe of the diverse macrophysical processes responsible for the transport and energisation of particles. Stellar and planetary systems beyond the Solar system present an even richer diversity of plasma environments, and motivate the search for associated transient radio emissions that provide one of the only lenses into local magnetospheric conditions and dynamics. Building a larger sample of radio stars is necessary to test plasma physics in regimes that are inaccessible within the Solar system, to constrain models of the generation and dissipation of stellar magnetic fields, and to further develop understanding of the relationships between stellar magnetism and other fundamental stellar parameters.

While targeted surveys are ideal for the detailed study of previously identified radio stars, and are an essential component in constraining local plasma conditions, they are incapable of providing an unbiased view of the wider population. In contrast unbiased widefield surveys are ideal as a discovery tool and are capable of building large statistical samples for targeted followup, but unambiguous detection of radio stars in a widefield search has been challenging since the beginnings of radio astronomy due to the overwhelming population of extragalactic radio sources that dominate the sky. In this thesis I will highlight the use of circular polarisation as a tool for the unambiguous identification of radio stars with widefield radio survey instruments such as ASKAP.

In Chapter 2 I present the first centimetre band all-sky circular polarisation survey at 888 MHz (Pritchard et al. 2021). This search was conducted as part of the RACS-low and resulted in 33 radio star detections including 23 that were previously unreported as radio loud in the literature. These results demonstrate the effectiveness of circular polarisation searches as a discovery tool that will become standard in future all-sky transient radio surveys.

In Chapter 3 I present an extension of this search technique to the multi-epoch low band VAST pilot survey at 888 MHz (Pritchard et al. 2024). This is the first dedicated multi-epoch survey in circular polarisation, and the repeat-sampling of this survey has allowed robust estimates of radio activity population parameters such as the fraction of M-dwarfs producing coherent radio bursts. These surveys have also resulted in estimates of the radio star surface density and expected detection rates in future surveys with ASKAP and the Square Kilometre Array.

In Chapter 4 I present the discovery of auroral pulses from the M9.5 ultracool dwarf SCR J1845−6357 and the results of a two year, 200 h monitoring program with ASKAP and ATCA observations spanning 0.8–10 GHz. This object was discovered in a circular polarisation search with ASKAP as part of the Deeper Wider Faster (DWF; Andreoni & Cooke 2019) program, and is the oldest and slowest rotating aurorally active UCD detected to date, representing a prime example of the discovery benefits of widefield circular polarisation searches. In this work I present dynamic spectra of a diverse range of periodic and apparently stochastic coherent pulses.

In Chapter 5 I provide conclusions and an outlook to the application of circular polarisation searches in future surveys with ASKAP and the Square Kilometre Array, which should produce tens of thousands of radio star detections in the coming years.

Chapter 2

A circular polarisation survey for radio stars with ASKAP

Joshua Pritchard,[1,2,3] Tara Murphy,[1,3] Andrew Zic,[1,2] Christene Lynch,[4,5] George Heald,[6] David L. Kaplan,[7] Craig Anderson,[8,2] Julie Banfield,[2] Catherine Hale,[6] Aidan Hotan,[6] Emil Lenc,[2] James K. Leung,[1,2,3] David McConnell,[2] Vanessa A. Moss,[2,1] Wasim Raja,[2] Adam J. Stewart,[1] and Matthew Whiting[2]

[1]Sydney Institute for Astronomy, School of Physics, University of Sydney, NSW 2006, Australia
[2]CSIRO Astronomy and Space Science, PO Box 76, Epping, NSW 1710, Australia
[3]ARC Centre of Excellence for Gravitational Wave Discovery (OzGrav), Hawthorn, Victoria, Australia
[4]International Centre for Radio Astronomy Research (ICRAR), Curtin University, Bentley, WA, Australia
[5]ARC Centre of Excellence for All Sky Astrophysics in 3 Dimensions (ASTRO3D), Bentley, WA, Australia
[6]CSIRO Astronomy and Space Science, PO Box 1130, Bentley, WA 6102, Australia
[7]Department of Physics, University of Wisconsin–Milwaukee, Milwaukee, Wisconsin 53201, USA.
[8]National Radio Astronomy Observatory, 1003 Lopezville Rd, Socorro, NM 87801, USA

This Chapter was published as Pritchard et al. (2021), MNRAS, 502, 5438. All content included in this chapter is my own work unless otherwise stated—including writing the manuscript, production of tables and figures, development of the code, candidate selection and classification. with specific contributions from co-authors described below. Andrew Zic and Christene Lynch contributed helpful discussion in the interpretation of emission from some stars, and all other co-authors contributed to observation, processing and quality analysis of the RACS-low data products that this work is based upon.

2.1 Abstract

We present results from a circular polarisation survey for radio stars in the Rapid ASKAP Continuum Survey (RACS). RACS is a survey of the entire sky south of $\delta = +41^\circ$ being conducted with the Australian Square Kilometre Array Pathfinder telescope (ASKAP) over a 288 MHz wide band centred on 887.5 MHz. The data we analyse includes Stokes I and V polarisation products to an RMS sensitivity of 250 µJy PSF^{-1}. We searched RACS for sources with fractional circular polarisation above 6 %, and after excluding imaging artefacts, polarisation leakage, and known pulsars we identified radio emission coincident with 33 known stars. These range from M-dwarfs through to magnetic, chemically peculiar A- and B-type stars. Some of these are well known radio stars such as YZ CMi and CU Vir, but 23 have no previous radio detections. We report the flux density and derived brightness

temperature of these detections and discuss the nature of the radio emission. We also discuss the implications of our results for the population statistics of radio stars in the context of future ASKAP and Square Kilometre Array surveys.

2.2 Introduction

While most stars generally have weak radio emission and are undetectable over Galactic distance scales, magnetically active stars are known to exhibit radio bursts with intensities orders of magnitude greater than those produced by the Sun. Radio bursts have been detected from a wide range of stellar types, including chromospherically active M-dwarfs, ultracool dwarfs, close and interacting binaries, and magnetic chemically peculiar (MCP) stars (see Güdel 2002 for a review). Stellar radio bursts are often highly circularly-polarised with brightness temperatures in excess of 10^{12} K, requiring the operation of a non-thermal, coherent emission process. Coherent radio bursts are generally attributed to one of two processes: plasma emission which operates at the fundamental and second harmonic of the local plasma frequency $\omega_p = \sqrt{4\pi n_e e^2/m_e}$, or electron cyclotron maser (ECM) emission at the local relativistic cyclotron frequency $\omega_c = eB/\gamma m_e c$ (see Dulk 1985 for a detailed review of these processes). Here n_e, e, and m_e are the electron density, charge, and mass respectively, B is the magnetic field strength, γ is the Lorentz factor, and c is the speed of light.

If the emission mechanism can be determined, these processes are an excellent measure of either the electron density or magnetic field of the stellar magnetosphere, and provide a means to probe extreme events such as particle acceleration driven by magnetic reconnection (Crosley et al. 2016) and auroral current systems (Leto et al. 2017). Periodic auroral bursts are often highly beamed and modulated by stellar rotation, providing an independent constraint on the stellar rotation period (Zic et al. 2019b). Constraints on the energetics and rates of stellar radio bursts also inform models of magnetospheric topology (Andre et al. 1991), cool star magnetic dynamos (Kao et al. 2016), the origin of strong magnetic fields in hot stars (Schneider et al. 2016), and the habitability of exoplanets (Crosley & Osten 2018b).

Despite the wide variety of stars demonstrating non-thermal radio bursts, studies have typically been limited to targeted observations of a small number of candidates, whose selection is motivated by activity indicators such as prior optical or X-ray flaring (White et al. 1989; Güdel 1992), presence of chromospheric emission lines (Slee et al. 1987), or previously known radio activity (Villadsen & Hallinan 2019). Surveys have also been conducted specifically targeting known classes of radio star such as RS Canum Venaticorum (RS CVn) and Algol binaries (Collier et al. 1982; Morris & Mutel 1988; Umana et al. 1998), hot OB-type stars (Bieging et al. 1989), young stellar objects (YSOs) (Andre et al. 1987; Osten & Wolk 2009), and ultracool dwarfs (Antonova et al. 2013). The selection biases inherent in these targeted searches impact the inference of population statistics, and do not allow for the discovery of new classes of radio stars.

A few volume-limited surveys for radio stars have been conducted, though their success has been limited by the high surface density of background radio sources, resulting in a large number of false-positive matches. Helfand et al. (1999) searched 5000 deg^2 of high Galactic latitude sky to a sensitivity of 0.7 mJy PSF^{-1} in the VLA Faint Images of the Radio Sky at Twenty-cm (FIRST; Becker et al. 1995) survey identifying 26 radio stars. Kimball et al. (2009) further explored FIRST in a comparison with the Sloan Digital Sky Survey (SDSS; Adelman-McCarthy et al. 2008) selecting 112 point radio sources coincident with spectrally confirmed SDSS stars, though a similar number of matches are estimated due to chance alignment with background galaxies. Umana et al. (2015) surveyed a 4 deg^2 field located within the Galactic plane to a sensitivity of 30 µJy PSF^{-1} in a search for stellar radio emission, and identified 10 hot stars producing thermal radio emission out of 614 detected sources. Vedantham et al. (2020a) crossmatched radio sources in the LOFAR Two-Metre Sky Survey (LOTSS; Shimwell et al. 2017) with nearby stars in Gaia Data Release 2 (Andrae et al. 2018), discovering an M-dwarf producing coherent, circularly polarised auroral emission at metre wavelengths.

Circular polarisation surveys are a promising method for wide-field detection of stellar radio bursts, as the synchrotron emission from Active Galactic Nuclei (AGN) that accounts for the majority of unresolved radio sources is typically less than 1–2 % circularly-polarised (Macquart 2002), and thus the number of false-positive matches between stars and unrelated background AGN is significantly reduced. Lenc et al. (2018) performed an all-sky circular polarisation survey at 200 MHz with the Murchison Widefield Array (MWA; Bowman et al. 2013) detecting 33 previously known pulsars and two magnetically-active stars. There have been no other all-sky circular polarisation radio surveys, and none have been conducted at centimetre wavelengths where targeted campaigns of magnetically-active stars have previously been focused (e.g., Antonova et al. 2013; Villadsen & Hallinan 2019).

The Australian Square Kilometre Array Pathfinder (ASKAP; Johnston et al. 2008; Hotan et al. 2021) is a radio telescope array of 36×12-metre antennas located in the Murchison Radio-astronomy Observatory in Western Australia. As part of the Rapid ASKAP Continuum Survey (RACS; McConnell et al. 2020) we have performed the first all-sky circular polarisation survey for radio stars at centimetre wavelengths. In § 2.3 we describe the RACS observations and data processing. In § 2.4 we describe our search procedure for stars with significant circular polarisation. We present the detected radio stars in § 2.5 and discuss the implications of our survey on stellar radio burst statistics and future ASKAP surveys in § 2.6.

2.3 Observations and Data Reduction

RACS is the first all-sky survey performed with the full 36 antenna ASKAP telescope, and covers the entire sky south of $\delta = +41°$. Each antenna in the array is equipped with a Phased Array Feed (PAF; Hotan et al. 2014; McConnell et al. 2016) which allows 36 dual linear polarisation beams to be formed on the sky. All four cross-correlations were recorded, allowing full Stokes I, Q, U and V images to be reconstructed. The antenna roll-axis was adjusted throughout the observations to maintain orientation of the linear feeds with respect to the celestial coordinate frame, so the beam footprint remained fixed on the sky and no correction for parallactic angle was required. RACS observations used a 6×6-beam square footprint giving a 32 deg^2 field of view, and were acquired in 15 minute integrations at a central frequency of 887.5 MHz with 288 channels each 1 MHz wide. RACS observations were conducted from April through May 2019, with fields originally located near the Sun observed in August 2019.

2.3.1 Data Reduction

ASKAP data is calibrated and imaged with the ASKAPsoft package (Cornwell et al. 2011; Guzman et al. 2019) using the *Galaxy* computer cluster that is maintained at the Pawsey Supercomputing Centre. The methods used for RACS data reduction are described in detail by (McConnell et al. 2020), and are summarised here.

Data were prepared for imaging by flagging bad samples and applying a calibration derived from the calibration source PKS B1934−638, which included factors for adjustment of interferometric phase and for setting the absolute flux density scale. Images were formed for each beam as the first two terms (0, 1) of a Taylor series in frequency using multi-frequency synthesis. ASKAPsoft applies weights to the visibility data using *preconditioning* (Rau 2010); RACS data were weighted to achieve the equivalent of a Briggs (1995) 'robust weight' of $r = 0.0$, where r takes values between -2 and 2 corresponding to uniform and natural weighting respectively. All beam images were deconvolved using the BasisfunctionMFS algorithm before being combined into a single image by linear mosaicing. Beam images were made with 6 144 × 6 144 pixels each of size 2″.5, and the final mosaics have approximately[1] 11 800 × 11 800 pixels of the same size.

2.3.2 Data Quality

A complete description of the published RACS images and source catalogue, including final quality control metrics, are presented by McConnell et al. (2020) and Hale et al. (2021) respectively. We describe the main quality metrics relevant to an early processing of the data used in this work.

The mosaic images have a point-spread-function (PSF) that varies over the field of view and between images due to the variation in sampling of the (u,v)-plane by individual beams. The central lobe of the PSF has a typical major axis full width half maximum (FWHM) B_{maj} of 18″.0 and minor axis FWHM B_{min} of 11″.8 with variations of ±4″.3 and ±0″.9 respectively. We assessed the flux density uncertainty introduced by PSF variation by direct comparison to the RACS source catalogue presented in Hale et al. (2021). This catalogue was produced from images that are convolved to a common resolution of 25 arcsec with a uniform PSF, and has a median flux density ratio of $S_{\rm RACS}/S_{\rm SUMSS} \approx 1{\pm}0.20$ derived from comparison to the Sydney University Molonglo Sky Survey (SUMSS; Mauch et al. 2003). We selected a sample of bright, unresolved RACS catalogue sources which are isolated from neighbouring

[1]The mosaic boundary is determined by the values of primary beam weights and is slightly irregular.

components by at least 150″ such that they are free from contamination due to close neighbours, and crossmatched this sample with their counterparts in our images. We find a median ratio between our fluxes and those from the RACS source catalogue of 1.03 ± 0.09. The uncertainty in this ratio contains contributions from random errors attributable to signal to noise ratio (SNR) and position-dependent effects described by McConnell et al. (2020). We scaled our fluxes by this 3 % factor and incorporated the 9 % uncertainty in quadrature with the RACS catalogue flux scale uncertainty, arriving at a cumulative flux density uncertainty of $\Delta S/S = 0.22$.

Our positional accuracy was assessed by comparison to the second realisation of the International Celestial Reference Frame (ICRF2; Fey et al. 2015) catalogue. Although ICRF2 sources are sparsely distributed across the sky, 2059 are a good positional match to the bright, unresolved, and isolated sample described above. The distribution of positional offsets between RACS and ICRF2 for these sources has a systematic shift of $-0\farcs6$ in right ascension and $+0\farcs1$ in declination, and standard deviation of $0\farcs5$ in both coordinates. This positional uncertainty is less than the pixel scale of $2\farcs5$.

The images that we analyse in this work were made before the development of the on-axis polarisation leakage correction described by (McConnell et al. 2020). We assessed the magnitude of leakage between Stokes I and V by assuming all field sources with peak total intensity flux density $S_{888} > 300\,\mathrm{mJy\,PSF^{-1}}$ are unpolarised, such that any observed Stokes V flux is solely due to leakage. A small number of pulsars are brighter than this threshold and intrinsically polarised, though the source density of bright AGN is much greater allowing for a good estimate of the magnitude of leakage. Among 11 974 field sources in negative Stokes V and 1217 in positive[2], we find a median polarisation leakage of 0.65 % and 0.54 % respectively, with hot spots of up to ∼2 % near the mosaic corners.[3]

The properties of the early processing data analysed in this work are summarised in Table 2.1. Further refinements have been applied to the published RACS images and source catalogue, and we refer the reader to McConnell et al. (2020) and Hale et al. (2021) for a complete description of the publicly available data.

2.4 Candidate Search

We used the SELAVY (Whiting & Humphreys 2012) source finder package with default settings to extract source components from the Stokes V images, with source extraction run once to extract 39 553 positive components and a second time on the inverted images to extract 99 647 negative components. We crossmatched the combined 139 200 polarised components against the extracted Stokes I components

[2]Throughout this work we adopt the IAU sign convention for which positive Stokes V corresponds to right handed circular polarisation and negative Stokes V to left handed, as seen from the perspective of the observer.

[3]The asymmetry between the number of negative and positive components is due to a bias in the mosaic Stokes V leakage pattern caused by uncertainty in the shape of the 36 PAF primary beams, resulting in imperfect overlap of the individual beam widefield leakage patterns. The real, polarised sources detected in this work are evenly distributed between positive and negative.

Table 2.1: Summary of early processing RACS data properties.

Property	Value
Sky Coverage	$-90° \leq \delta < +41°$
Central Frequency	887.5 MHz
Bandwidth	288 MHz
Integration Time	15 min
Typical RMS Noise	$250\,\mu$Jy PSF^{-1}
Cumulative Flux Density Accuracy	$\Delta S/S = 0.22$
Polarisation Leakage	0.65% (V negative)
	0.54% (V positive)
Astrometric Accuracy	$\Delta\alpha\cos\delta = -0\farcs6 \pm 0\farcs5$
	$\Delta\delta = +0\farcs1 \pm 0\farcs5$
PSF Central Lobe (FWHM)	$B_{min} = 11\farcs8 \pm 0\farcs9$
	$B_{maj} = 18\farcs0 \pm 4\farcs3$

using a $2''$ match radius. This match radius was chosen to avoid contamination from matches between sidelobes of bright Stokes I components and the leakage of the bright central component into Stokes V, though it is restrictive as positional offsets between Stokes I and V up to $\sim 5''$ exist for genuine circularly polarised source components. We selected this restricted sample to investigate robust methods to reject imaging artefacts in future searches, and to reduce the search volume to a reasonable size.

SELAVY models source components with 2D Gaussians that have an SNR dependent positional error (Condon 1997) of

$$\sigma_\theta = \frac{2\theta_m}{\mathrm{SNR}\sqrt{8\ln 2}} \tag{2.1}$$

where θ_m is the component major axis. We added this uncertainty in quadrature to the astrometric accuracy discussed in § 2.3.2 to determine the positional uncertainty of each radio source, where the positional uncertainty corresponding to a 5σ component with major axis equal to the typical synthesised beam major axis of $18\farcs0$ is approximately $3\farcs2$.

We selected 850 components with fractional polarisation $f_p = |V|/I$ greater than 6 % for visual inspection. This corresponds to 10 times the median circular polarisation leakage, and three times the excess leakage of $\sim$2 % near mosaic corners. The majority of selected sources were either imaging artefacts caused by leakage of bright Stokes I sidelobes, spurious noise near the edge of the image where sensitivity decreases, or components with extended structure associated with radio galaxies, which we excluded by visual inspection of the Stokes V and total intensity images. To aid further classification of our sample, we inspected image cutouts for the SUMSS, second epoch Molonglo Galactic Plane Survey (MGPS-2; Murphy et al. 2007), NRAO VLA Sky Survey (NVSS; Condon et al. 1998), TIFR GMRT Sky Survey (TGSS; Intema et al. 2017), GaLactic and Extragalactic All-sky MWA (GLEAM; Wayth et al. 2015; Hurley-Walker et al. 2017), and VLA Sky Survey (VLASS; Lacy et al.

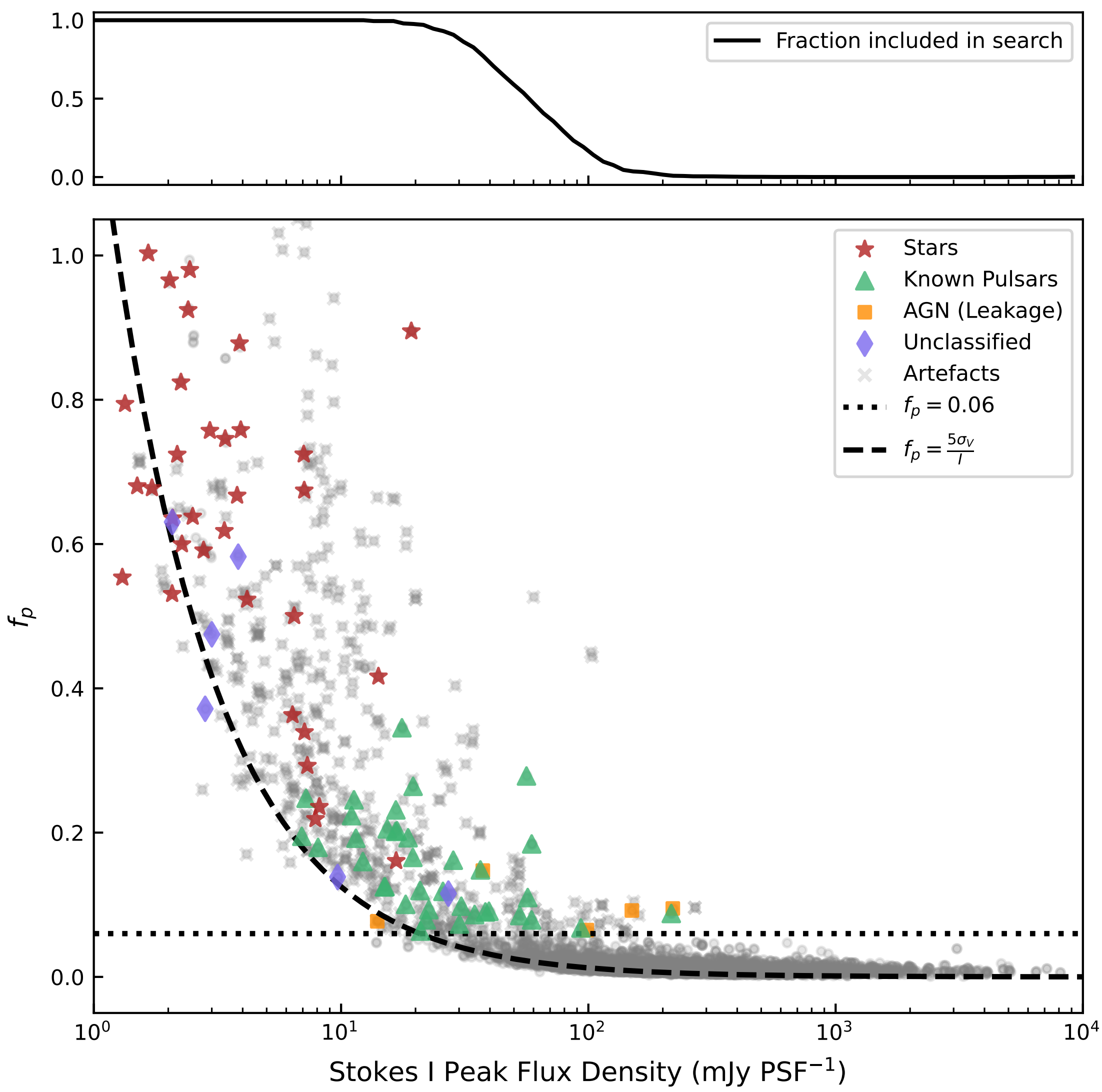

Figure 2.1: Classification of visually inspected candidates. The dotted line indicates a fractional circular polarisation of 6 % below which we excluded all source components, labelled as grey circles. The dashed line indicates a $5\sigma_V$ detection threshold where $\sigma_V = 0.25\,\mathrm{mJy\,PSF^{-1}}$ is the typical RMS noise in the Stokes V data, and represents the minimum fractional polarisation our search is sensitive to. Imaging artefacts are labelled as grey crosses, and polarisation leakage of bright AGN as yellow squares. The radio stars identified in our sample are labelled as red stars, and known pulsars as green triangles. Six circularly polarised sources of unknown classification are labelled as blue diamonds. The top panel shows the fraction of all components selected for visual inspection as a function of flux density.

2020) radio surveys, and produced radio spectral energy distributions (SEDs) and light curves for each candidate using the corresponding radio source catalogues, or 3σ upper limits in the case of a non-detection.

To identify optical and infra-red counterparts to our candidates we generated image cutouts from the *Widefield Infra-red Survey Explorer* (WISE; Wright et al. 2010), 2-Micron All Sky Survey (2MASS; Skrutskie et al. 2006), Panoramic Survey Telescope and Rapid Response System 1 (Pan-STARRS1; Chambers et al. 2016), and Skymapper (Da Costa et al. 2019) surveys. As very few stars are persistent radio sources, detection in multiple other radio surveys is suggestive of emission from background AGN. We calculated the WISE infra-red colours (see fig. 12, Wright et al. 2010) to distinguish these cases, as infra-red sources associated with background galaxies are typically reddened compared to stars. We also looked for evidence of the persistent X-ray and ultraviolet emission associated with some active stars in the *ROSAT* All Sky Survey (RASS; Boller et al. 2016) and *Galaxy Evolution Explorer* (GALEX; Morrissey et al. 2007) surveys.

We excluded five components that were a positional match for previously known radio sources attributed to bright AGN, either due to the shape of the radio SED, the WISE colours, or explicit identification in the literature. We attribute the Stokes V flux density for these sources to polarisation leakage as they are located near the mosaic edge at $\delta = +41^\circ$ where leakage increases, and AGN typically display fractional polarisation of at most 2 % (Macquart 2002). We identified 37 components as known pulsars, and six significantly polarised sources without any multi-wavelength counterpart or catalogued identification, which will be the subject of separate publications.

We queried the SIMBAD and NED databases for stars within a 3.′5 radius of candidate positions, which is sufficient to account for motion of the highest known proper motion stars over a 20 year period. We applied positional corrections to all query results with available proper motion parameters from Gaia Data Release 2, and identified 33 components that were a match with stars to within our positional uncertainty. Our classifications are summarised in Figure 2.1 where we show the fractional polarisation of all extracted components as a function of S_{888}. Below $S_{888} = 20.8\,\mathrm{mJy\,PSF^{-1}}$ the minimum detectable fractional polarisation is determined by the 5σ detection limits in Stokes V rather than contamination from polarisation leakage or the $f_p > 0.06$ filter we applied.

We quantified the false-positive rate for chance-alignment between our sources and unrelated stars by offsetting the positions of all 139, 200 Stokes V components, inclusive of artefacts, in random directions by 5–20 ° and crossmatching the new positions against the SIMBAD database. This procedure produced no matches within 2″, suggesting a false-positive rate of less than 2.2×10^{-5} and an extremely low probability that any of our detections are due to chance alignment with stars.

2.5 Results

Table 2.2 lists the 33 radio stars detected within our sample, 23 of which have not previously been reported as radio-loud in the literature. Figure 2.2 shows a radio-selected Hertzprung-Russell diagram with 231 stars from the Wendker catalogue (Wendker 1995) colour-mapped by observing frequency. Our detections are

Table 2.2: Table of detected radio stars. Columns are stellar name, spectral class, radio coordinates, assumed upper limit to emission region length scale R_e, stellar parallax, 887.5 MHz Stokes I peak flux density S_{888}, signed fractional polarisation, lower limit to brightness temperature, and previous radio detection references.

Name	Spectral Class	RA (J2000)	Dec (J2000)	$R_e(R_\odot)^\dagger$	R_e Ref.	π (mas)	S_{888} (mJy PSF^{-1})	$f_p{}^*$	$\log_{10} T_B$	Radio Ref.
Cool Dwarfs										
G 131–26	M5V	00:08:53.89	+20:50:19.39	0.75 ± 0.27		55.3 ± 0.8	2.68 ± 1.17	0.594 ± 0.211	10.62 ± 0.24	
CS Cet	K0IV(e)	01:06:48.93	−22:51:23.20	11.10 ± 0.27		10.5 ± 0.1	6.19 ± 1.50	0.364 ± 0.083	10.08 ± 0.10	
UPM J0250−0559		02:50:40.29	−05:59:50.89	0.66 ± 0.11		33.2 ± 1.0	2.18 ± 0.85	0.825 ± 0.219	11.08 ± 0.18	
LP 771–50	M5e	02:56:27.19	−16:27:38.53	0.29 ± 0.06		32.6 ± 0.4	1.61 ± 0.89	1.003 ± 0.373	11.68 ± 0.25	
CD−44 1173	K6.5Ve	03:31:55.74	−43:59:14.92	2.35 ± 0.20		22.1 ± 0.0	3.77 ± 1.09	-0.875 ± 0.176	10.57 ± 0.13	
UPM J0409−4435		04:09:32.15	−44:35:38.19	0.59 ± 0.12		68.1 ± 0.0	2.34 ± 0.80	-0.925 ± 0.225	10.59 ± 0.17	
V833 Tau	K2.5Ve	04:36:48.60	+27:07:55.04	2.58 ± 0.14		57.1 ± 0.1	3.82 ± 1.53	-0.758 ± 0.200	9.67 ± 0.17	Güd92
YZ CMi	M4Ve	07:44:39.67	+03:33:01.79	0.72 ± 0.14		167.0 ± 0.1	2.36 ± 1.52	-0.986 ± 0.430	9.64 ± 0.28	Dav78, Vil19
G 41–14	M3.5V	08:58:56.75	+08:28:19.76			147.7 ± 2.0	18.66 ± 4.03	-0.895 ± 0.137		
MV Vir	K5.5Vkee	14:14:21.16	−15:21:25.64	3.57 ± 0.36		34.5 ± 0.2	1.67 ± 0.82	-0.675 ± 0.294	9.47 ± 0.21	
G 165–61	M4.5Ve	14:17:02.04	+31:42:44.26	0.71 ± 0.23		60.0 ± 2.2	1.96 ± 0.84	0.963 ± 0.278	10.46 ± 0.23	
CD−38 11343	M3Ve+M4Ve	16:56:48.49	−39:05:38.96	1.70 ± 0.29		63.8 ± 0.1	7.08 ± 1.96	-0.293 ± 0.096	10.21 ± 0.14	
UCAC4 312–101210		17:02:07.98	−27:40:28.67	0.72 ± 0.18		41.9 ± 0.1	3.31 ± 1.32	0.744 ± 0.231	10.99 ± 0.20	
Ross 867	M4.5V	17:19:52.68	+26:30:09.94	0.98 ± 0.16		93.0 ± 0.1	3.68 ± 1.12	0.667 ± 0.143	10.07 ± 0.15	Jac87, Whi89, Qui20
G 183–10	M3.5Ve	17:53:00.26	+16:54:59.07	0.80 ± 0.20		44.2 ± 1.0	2.01 ± 0.80	0.531 ± 0.200	10.64 ± 0.20	
SCR J1928−3634		19:28:33.74	−36:34:39.21	0.43 ± 0.09		39.5 ± 0.1	2.44 ± 1.05	-0.638 ± 0.214	11.35 ± 0.20	
Ross 776	M3.3	21:16:06.14	+29:51:52.37	1.12 ± 0.17		49.2 ± 0.2	6.26 ± 1.54	0.500 ± 0.094	10.74 ± 0.12	
SCR J2241−6119		22:41:44.80	−61:19:33.24	0.24 ± 0.02		35.2 ± 0.0	4.04 ± 1.09	0.523 ± 0.124	12.18 ± 0.12	
Interacting Binaries										
HR 1099	K2Vnk	03:36:47.19	+00:35:13.52	40.20 ± 0.90	Mut84	33.8 ± 0.1	16.20 ± 3.51	-0.161 ± 0.033	8.37 ± 1.61	Mut84, Whi95, Sle08, Rav10
V1154 Tau	B6III/IV	05:05:37.70	+23:03:41.56	34.1 ± 20.4		3.1 ± 0.9	2.00 ± 0.86	-0.639 ± 0.201	9.67 ± 1.89	
ξ UMa	F8.5V	11:18:10.18	+31:31:31.12	29.95 ± 0.03	Gri98	114.5 ± 0.4	1.45 ± 0.92	-0.680 ± 0.302	6.52 ± 3.29	
BH CVn / HR 5110	A6m+KIV	13:34:47.90	+37:10:56.78	17.10 ± 0.15	Abb15	21.7 ± 0.2	6.92 ± 1.65	-0.338 ± 0.078	9.13 ± 0.25	Mut87, Whi95, Abb15
V851 Cen	K0III	13:44:00.96	−61:21:58.92	66.33 ± 0.49	Kar04	13.5 ± 0.0	6.85 ± 2.17	0.726 ± 0.154	8.36 ± 5.31	
KZ Pav	F6V	20:58:39.76	−70:25:20.58	17.16 ± 0.06	Sur10	8.9 ± 0.0	1.26 ± 0.47	-0.554 ± 0.201	9.16 ± 0.44	Sle87, Ste89
Young Stellar Objects										
ρ Oph S1	B3	16:26:34.11	−24:23:28.19	12.8 ± 4.8	And91	8.2 ± 0.1	7.92 ± 1.77	-0.234 ± 0.063	10.89 ± 0.15	Fal81, And88, And91
EM* SR 20	G7	16:28:32.50	−24:22:45.80	2.39 ± 0.61		7.4 ± 0.1	2.12 ± 0.85	0.719 ± 0.215	11.26 ± 0.20	
Magnetic Chemically Peculiar Stars										
k^2 Pup	B3IV He-W	07:38:49.74	−26:48:12.84	16.07 ± 2.92		9.4 ± 0.8	2.86 ± 0.81	0.757 ± 0.162	9.52 ± 0.15	
OY Vel	ApSi	09:01:44.44	−52:11:19.81	12.44 ± 4.61		8.8 ± 0.4	6.87 ± 1.60	0.675 ± 0.116	10.18 ± 0.19	
V863 Cen	B6IIIe He-S	12:08:05.06	−50:39:40.79	15.62 ± 3.00		9.8 ± 0.3	2.20 ± 0.63	0.600 ± 0.154	9.39 ± 0.15	
CU Vir	ApSi	14:12:15.72	+02:24:34.19	9.62 ± 3.21		12.6 ± 0.2	13.72 ± 3.49	0.416 ± 0.074	10.39 ± 0.18	Tri00, Let06, Rav10, Lo12
V1040 Sco	B2Ve He-S	15:53:55.82	−23:58:41.33	9.30 ± 0.60	Let18	7.6 ± 0.4	7.64 ± 1.75	0.219 ± 0.055	10.61 ± 0.10	Con98, Mur10, Let18
Hot Spectroscopic Binaries										
HD 32595	B8	05:04:49.06	+13:18:32.86	10.44 ± 0.93		3.0 ± 0.2	3.27 ± 1.19	0.618 ± 0.184	10.96 ± 0.16	
Castor A	A1V+dMe	07:34:35.49	+31:53:14.63	6.57 ± 0.12	Tor02	64.1 ± 3.8	1.30 ± 0.69	0.794 ± 0.295	8.29 ± 0.22	Sch94, Hel99

* $f_p > 0$ corresponds to right handed circular polarisation.

† R_e taken as: $3R_\star$ for single stars as calculated from Gaia DR2 photometry (Gaia Collaboration et al. 2018), the inter-binary region for interacting binaries, or otherwise from literature where indicated by a reference code.

Reference codes: Abb15 (Abbuhl et al. 2015), And88 (Andre et al. 1988), And91 (Andre et al. 1991), Con98 (Condon et al. 1998), Dav78 (Davis et al. 1978), Fal81 (Falgarone & Gilmore 1981), Gru12 (Grunhut et al. 2012), Gri98 (Griffin 1998), Güd92 (Güdel 1992), Hel99 (Helfand et al. 1999), Jac87 (Jackson et al. 1987), Kar04 (Karataş et al. 2004), Let06 (Leto et al. 2006), Let18 (Leto et al. 2018), Lo12 (Lo et al. 2012), Mut84 (Mutel et al. 1984), Mut87 (Mutel et al. 1987), Mur10 (Murphy et al. 2010), Qui20 (Quiroga-Nuñez et al. 2020), Rav10 (Ravi et al. 2010), Sch94 (Schmitt et al. 1994), Sle87 (Slee et al. 1987), Sle08 (Slee et al. 2008), Ste89 (Stewart et al. 1989), Tor02 (Torres & Ribas 2002), Tri00 (Trigilio et al. 2000), Sur10 (Sürgit et al. 2010), Vil19 (Villadsen & Hallinan 2019), Whi89 (White et al. 1989), Whi95 (White & Franciosini 1995) overlaid as red stars and span the diagram, including magnetic chemically peculiar stars, young stellar objects, RS CVn and Algol binaries, and both chromospherically active and non-active K- and M-dwarfs. Figures 2.3 to 2.9 show cutout images in Stokes I and Stokes V for each of the stars in our sample, and optical data from Pan-STARRS1 or Skymapper at declinations above and below $-30°$ respectively. We have applied astrometric corrections to the optical data to the RACS epoch to account for proper motion, and all images are centred on the radio position.

2.5.1 Cool Dwarfs

We identify 18 K- and M-dwarf stars within our sample, 15 of which have no previously reported radio detection. Cool dwarfs typically produce non-thermal radio emission in magnetically confined coronae. Non-thermal, incoherent gyrosynchrotron emission dominates at C/X-band, and coherent emission processes at lower frequencies where gyrosynchrotron emission becomes optically thick (Güdel 2002). Our cool dwarf detections have fractional polarisation ranging from 29–100 %. Notes on individual sources are presented below.

G 131–26 (see Figure 2.3) is an M5V flare star demonstrating Hα (Hawley et al. 1996; Newton et al. 2017; Jeffers et al. 2018) and ultraviolet (Jones & West 2016) activity, and is a strong variable X-ray source (Hambaryan et al. 1999).

CS Cet (see Figure 2.3) is a spectroscopic binary with a K0IVe primary which has demonstrated BY Dra type photometric variability due to rotation of starspots (Watson et al. 2000). This system is a bright ultraviolet and X-ray source (Haakonsen & Rutledge 2009; Beitia-Antero & Gómez de Castro 2016) and is chromospherically active in Ca II H and K and Hα lines (Isaacson & Fischer 2010).

LP 771–50 (see Figure 2.3) is an M5Ve-type high-proper-motion star demonstrating Hα line emission (Cruz & Reid 2002).

CD−44 1173 (see Figure 2.3) is a young K6.5Ve star in the Tucana-Horologium moving group with rotationally modulated optical variability (Messina et al. 2010), and has previously exhibited ultraviolet flares (Loyd et al. 2018) and X-ray activity (Haakonsen & Rutledge 2009).

V833 Tau (see Figure 2.4) is an extremely active K2.5Ve BY Dra variable demonstrating both X-ray flares (Fuhrmeister & Schmitt 2003) and photometric variability due to large starspot covering fractions (Oláh et al. 2001). Güdel (1992) reported a radio flux of 5.22 ± 0.07 mJy at 8.5 GHz for this star which they attribute to gyrosynchrotron emission due to the observed $\sim 10^8$ K brightness temperature. We detect 76 % left circularly-polarised emission with $S_{888} = 3.94 \pm 0.46$ mJy PSF^{-1}, which corresponds to a brightness temperature of $\sim 5 \times 10^9$ K and is consistent with optically-thin gyrosynchrotron emission.

YZ CMi (see Figure 2.4) is an M4Ve eruptive variable known to produce bright optical flares (Kowalski et al. 2010), and is a well known radio flare star (Davis et al. 1978; Abada-Simon & Aubier 1997). Highly circularly-polarised radio bursts have

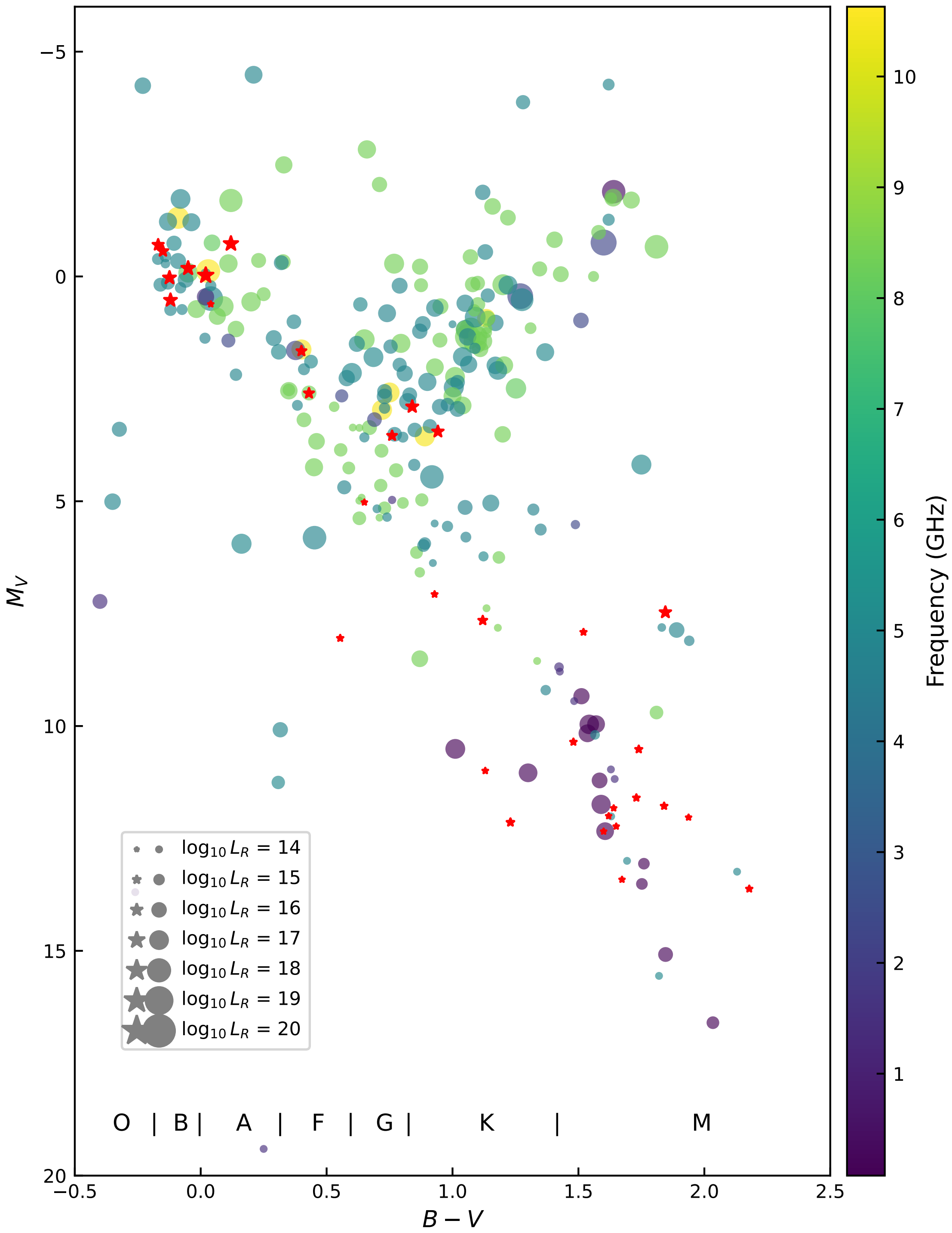

Figure 2.2: Radio-selected Hertzprung-Russell diagram, showing 231 previously detected radio stars (Wendker 1995) as circles with our sample overlaid as red stars. The size of each marker represents the greatest radio luminosity recorded for that star, and the colour-map indicates the observing frequency.

been detected from this star at centimetre wavelengths (Villadsen & Hallinan 2019) attributed to ECM emission from within extreme coronal plasma cavities which is modulated by stellar rotation. We detect 98 % left circularly-polarised emission, consistent with the handedness observed by Villadsen & Hallinan (2019).

G 41–14 (see Figure 2.4) is an M3.5V triple star system with recorded optical flares (Rodríguez Martínez et al. 2020) and Hα (Hawley et al. 1996; Newton et al. 2017; Jeffers et al. 2018) and ultraviolet (Miles & Shkolnik 2017) activity, but no previously reported radio emission. The star was included in a radio interferometric search of nearby stars for planetary companions (Bower et al. 2009) but no detections are reported. A 0.99 ± 0.14 mJy FIRST radio source is reported $7\farcs8$ from the RACS position and attributed to an SDSS galaxy (Thyagarajan et al. 2011). Proper motion correction of G 41–14 to the FIRST epoch results in a $1\farcs35$ separation from the FIRST position, indicating that the star may have been the origin of the radio emission. G 41–14 was detected in RASS (Fuhrmeister & Schmitt 2003) and is flagged as displaying X-ray flares.

MV Vir / HD 124498 (see Figure 2.4) is a binary system with a K5.5Vkee-type primary and an unclassified secondary. The system exhibits strong chromospheric Ca II H and K line emission (Boro Saikia et al. 2018) and is a bright ultraviolet (Ansdell et al. 2015) and X-ray source (Haakonsen & Rutledge 2009). We detect 68 % left circularly-polarised emission with $S_{888} = 1.72\,\mathrm{mJy\,PSF^{-1}}$ positioned $0\farcs9$ from HD 124498A and $2\farcs4$ from HD 124489B. Both components are within our positional uncertainty, so we can not distinguish which component is the source of emission. A neighbouring, unpolarised radio source is also visible in total intensity, with the combined source components resembling the morphology of a double-lobed radio galaxy. The high fractional polarisation of our detection is most easily explained if originating from MV Vir, and as both stars are separated $11\farcs6$ from the neighbouring source we believe it is an unrelated background object.

G 165–61 (see Figure 2.5) is an M4.5V spectroscopic binary that demonstrates both Hα (Newton et al. 2017) and ultraviolet (Jones & West 2016) activity. G 165–61 has a rotational period of 113.6 days (Newton et al. 2016), while M-dwarf radio bursts are typically associated with young, fast rotators (McLean et al. 2012), and only a small fraction of > 100 day period M-dwarfs demonstrate other indicators of magnetic activity (West et al. 2015; Mondrik et al. 2019).

CD−38 11343 (see Figure 2.5) is an M3Ve + M4Ve binary system of flare stars (Tamazian & Malkov 2014). The A component has been associated with flaring X-ray emission (Fuhrmeister & Schmitt 2003; Wright et al. 2011) and periodic optical variability due to rotation of starspots (Kiraga 2012). The angular separation between the stars is of the order of our positional uncertainty at $3\farcs1$, so that it is not clear from which star the emission originates.

Ross 867 and Ross 868 (see Figure 2.5) are a visual binary system of M4.5V and M3.5V flare stars with similar stellar properties. Both components have demonstrated optical flaring (Tamazian & Malkov 2014) and photospheric variability (Kiraga 2012), ultraviolet (Jones & West 2016) and X-ray (Fuhrmeister & Schmitt 2003) variability, and Hα activity (Hawley et al. 1996). Ross 867 is a well known radio-loud star (Jackson et al. 1987; White et al. 1989) and in particular has demonstrated radio bursts with moderate circular polarisation (Quiroga-Nuñez et al. 2020), while Ross 868 has never been detected at radio wavelengths. We detect 67 % right circularly-polarised emission with $S_{888} = 3.80 \pm 0.32$ mJy PSF^{-1} unambiguously associated with Ross 867, which is separated from Ross 868 by $16\farcs7$.

G 183–10 (see Figure 2.5) is an M4V-type star with no significant ultraviolet (Ansdell et al. 2015) or Hα (Jeffers et al. 2018) activity, and no previously reported radio detection.

Ross 776 (see Figure 2.6) is an M3.3V flare star (Tamazian & Malkov 2014) showing both Hα (Hawley et al. 1996; West et al. 2015) and ultraviolet activity (Jones & West 2016), and has previously demonstrated X-ray flaring (Fuhrmeister & Schmitt 2003). This star is a young, rapid rotator, with a 0.586 d photometric rotation period (Newton et al. 2016).

UPM J0250−0559, UPM J0409−4435, UCAC4 312−101210, SCR J1928−3634, and **SCR J2241−6119** (see Figures 2.3 to 2.6) are high proper motion stars without spectral classification, though photometric colour indices imply these are M-class stars (Lépine & Gaidos 2011; Winters et al. 2011; Frith et al. 2013). SCR J2241−6119 has also been proposed as an M7 ultra-cool dwarf from analysis of Gaia colours (Reylé 2018).

2.5.2 Interacting Binaries

We identify 6 interacting binary systems of RS CVn and Algol type, three of which have no previously reported radio detection. RS CVn and Algol binaries are known to possess strong magnetic fields generated by rapid, tidally-induced rotation periods. The radio emission associated with these stars is generally non-thermal with moderate circular polarisation, with both quiescent gyrosynchrotron emission (Jones et al. 1994; Abbuhl et al. 2015) and coherent radio bursts (van den Oord & de Bruyn 1994; White & Franciosini 1995; Slee et al. 2008) observed. Our detections in this category have a fractional polarisation between 16–88 %. Notes on individual sources are presented below.

HR 1099 / V711 Tau (see Figure 2.6) is a K2:Vnk/K4 RS CVn binary with extensive study at radio frequencies, and is known to exhibit both strong radio flaring and periods of quiescent emission. VLBI detections have been made during the quiescent period at 1.65 GHz (Mutel et al. 1984) with a source size comparable to the size of the binary system, and during a flare at 8.4 GHz (Ransom et al. 2002) revealing milliarcsecond structure. HR 1099 is also known to emit highly polarised, coherent radio bursts which are attributed to ECM driven auroral emission (Slee et al. 2008).

V1154 Tau (see Figure 2.6) is a B6III/IV-type eclipsing Algol binary with no previously reported radio detections.

ξ **UMa** (see Figure 2.7) is an F8.5:V+G2V RS CVn binary system with multiple

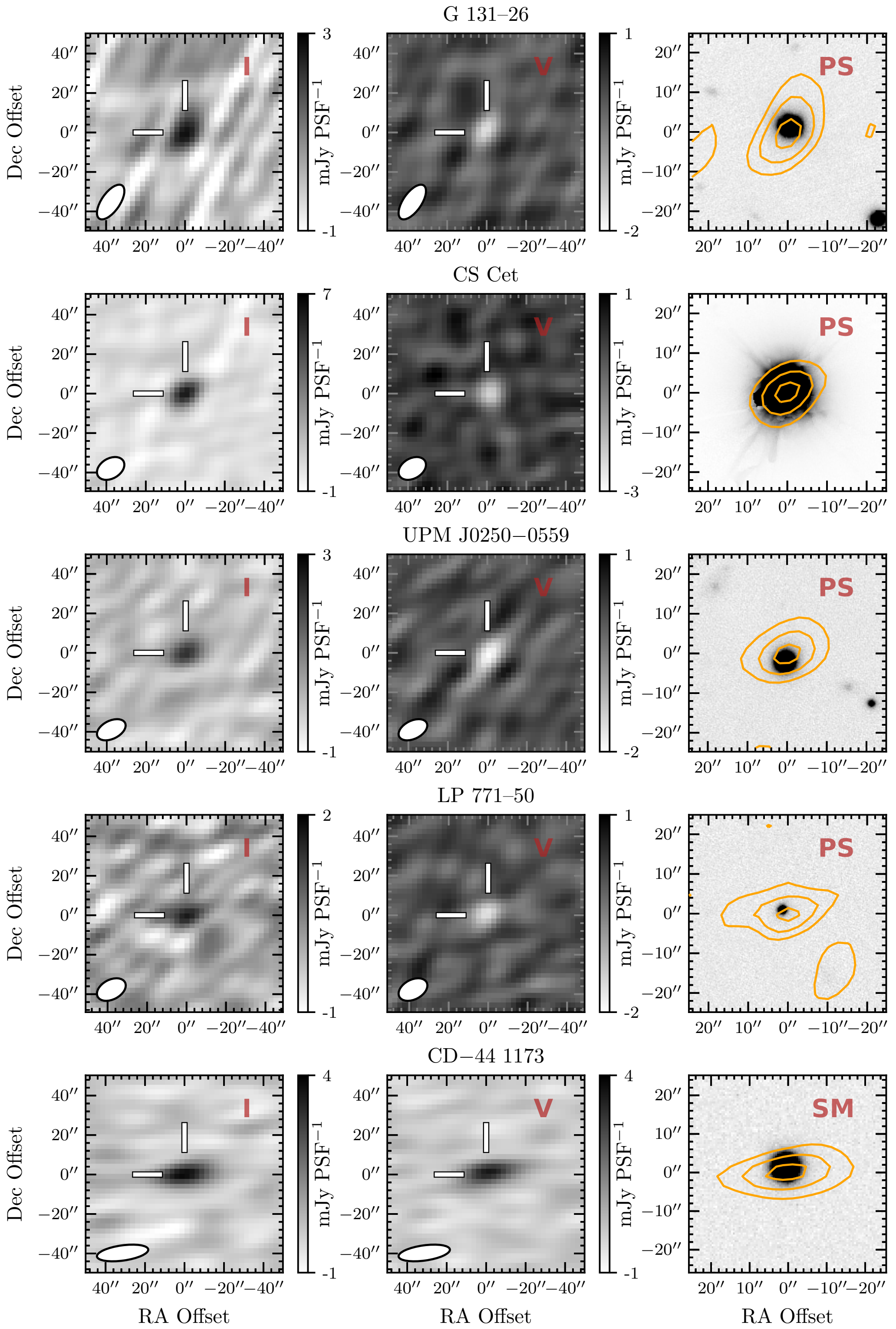

Figure 2.3: Images of G 131–26, CS Cet, UPM J0250−0559, LP 771–50, and CD−44 1173. RACS data is shown in Stokes I (left panels) and Stokes V (middle panels), where positive flux density in the Stokes V map corresponds to right handed circular polarisation and negative to left handed. The ellipse in the lower left corner of each radio image shows the restoring beam. The right panels show Stokes I contours overlaid on optical data from Pan-STARRS1 (g-band) or Skymapper for stars above and below $\delta = -30°$ respectively, with contour levels at 30 %, 60 %, and 90 % of the peak Stokes I flux density. All images have been centred on a frame aligned with the position of the radio source, with North up and East to the left. Optical data has been astrometrically corrected to the RACS epoch according to the proper motion of the target star. For some of the brighter stars the optical data is over-saturated or masked.

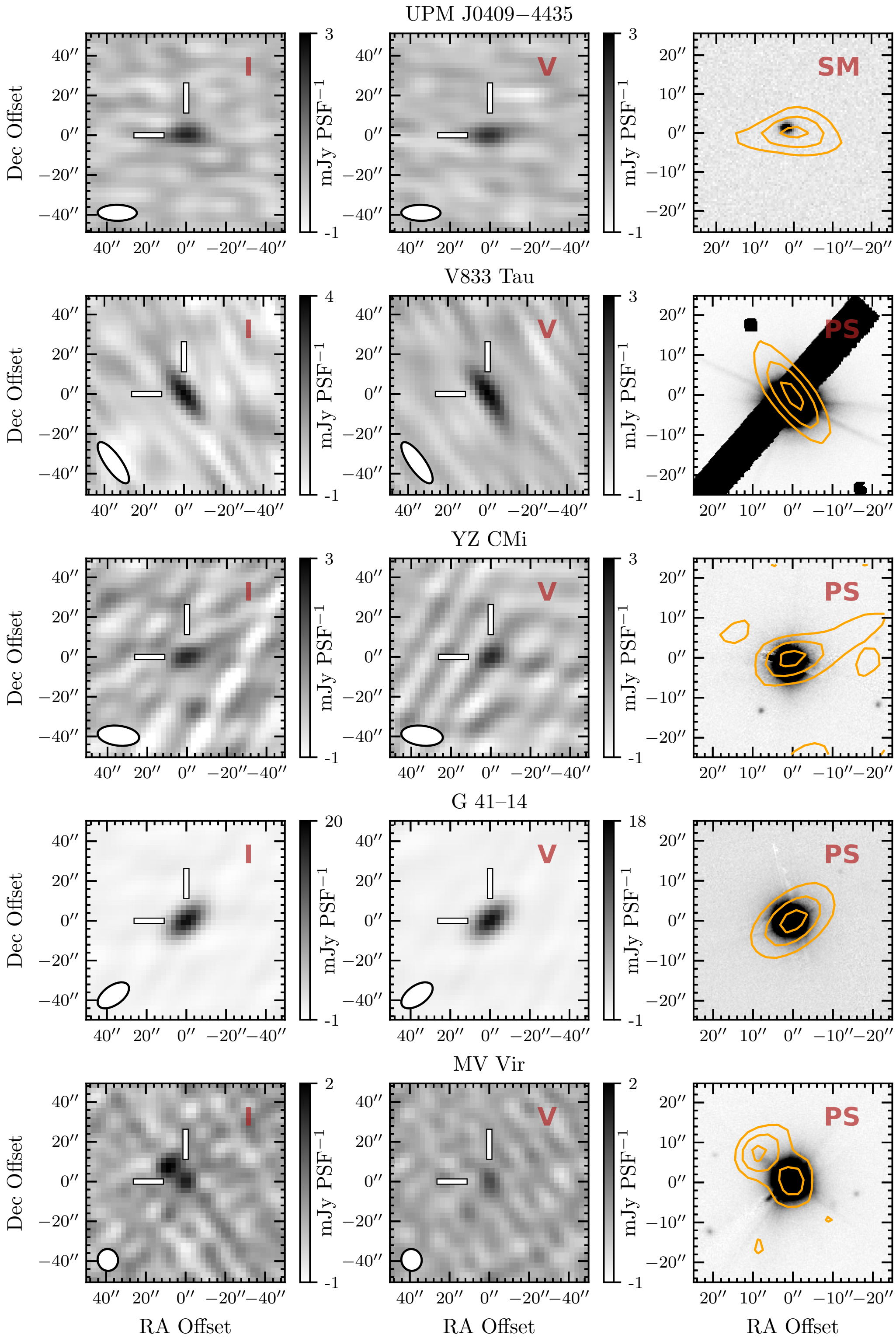

Figure 2.4: Images of UPM J0409−4435, V833 Tau, YZ CMi, G 41–14, and MV Vir. Details as in Figure 2.3.

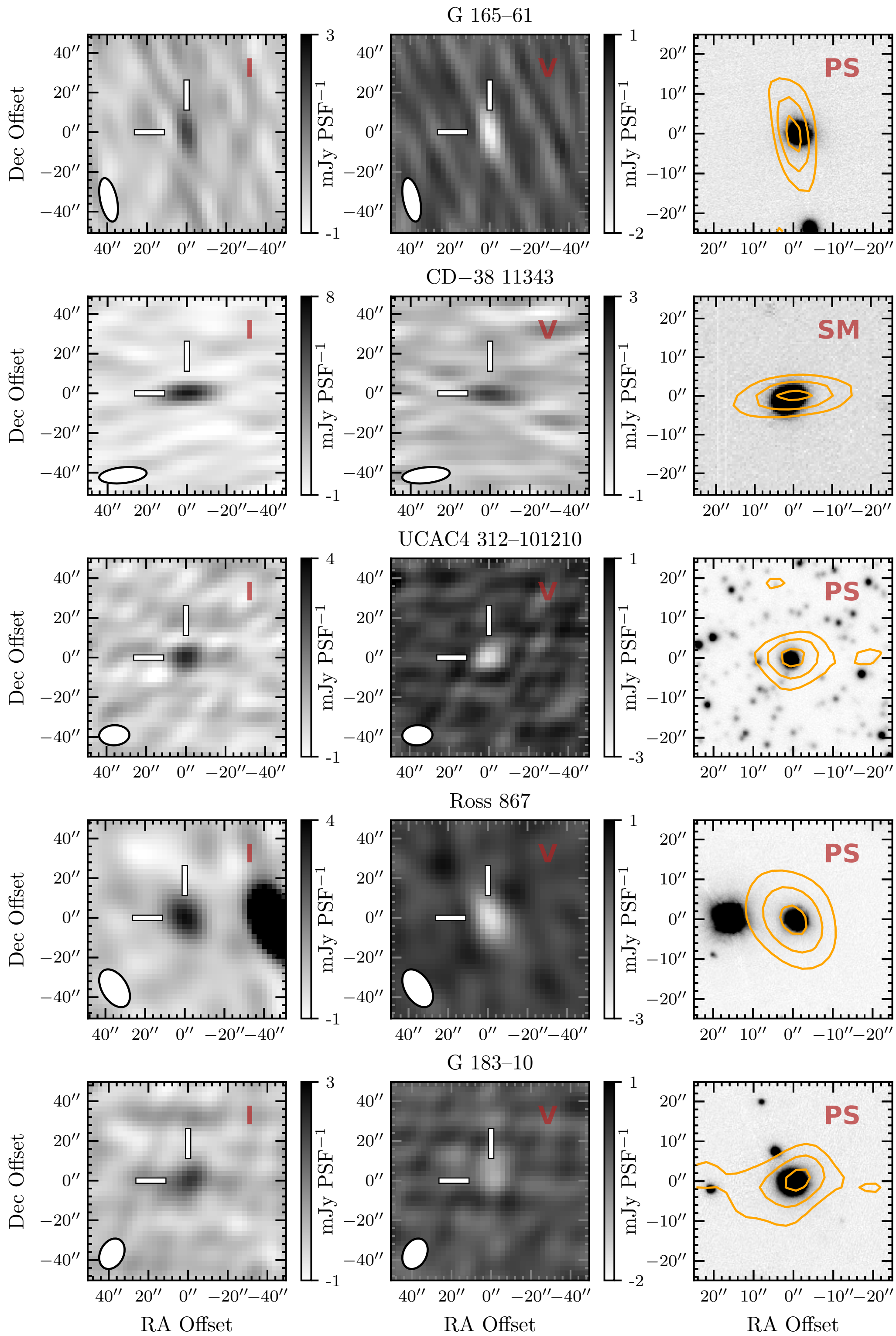

Figure 2.5: Images of G 165–61, CD−38 11343, UCAC4 312–101210, Ross 867, and G 183–10. Details as in Figure 2.3.

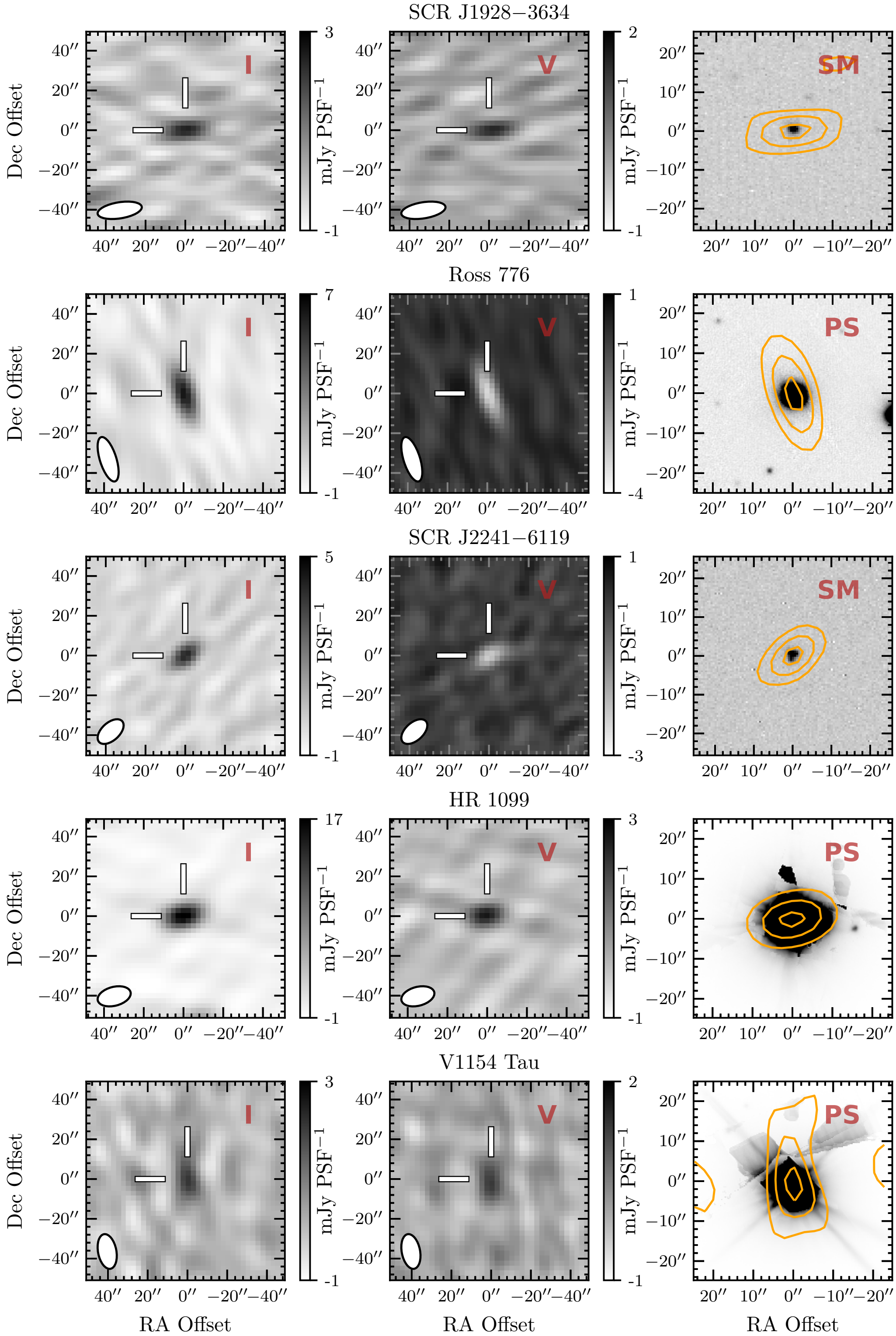

Figure 2.6: Images of SCR J1928−3634, Ross 776, SCR J2241−6119, HR 1099, and V1154 Tau. Details as in Figure 2.3.

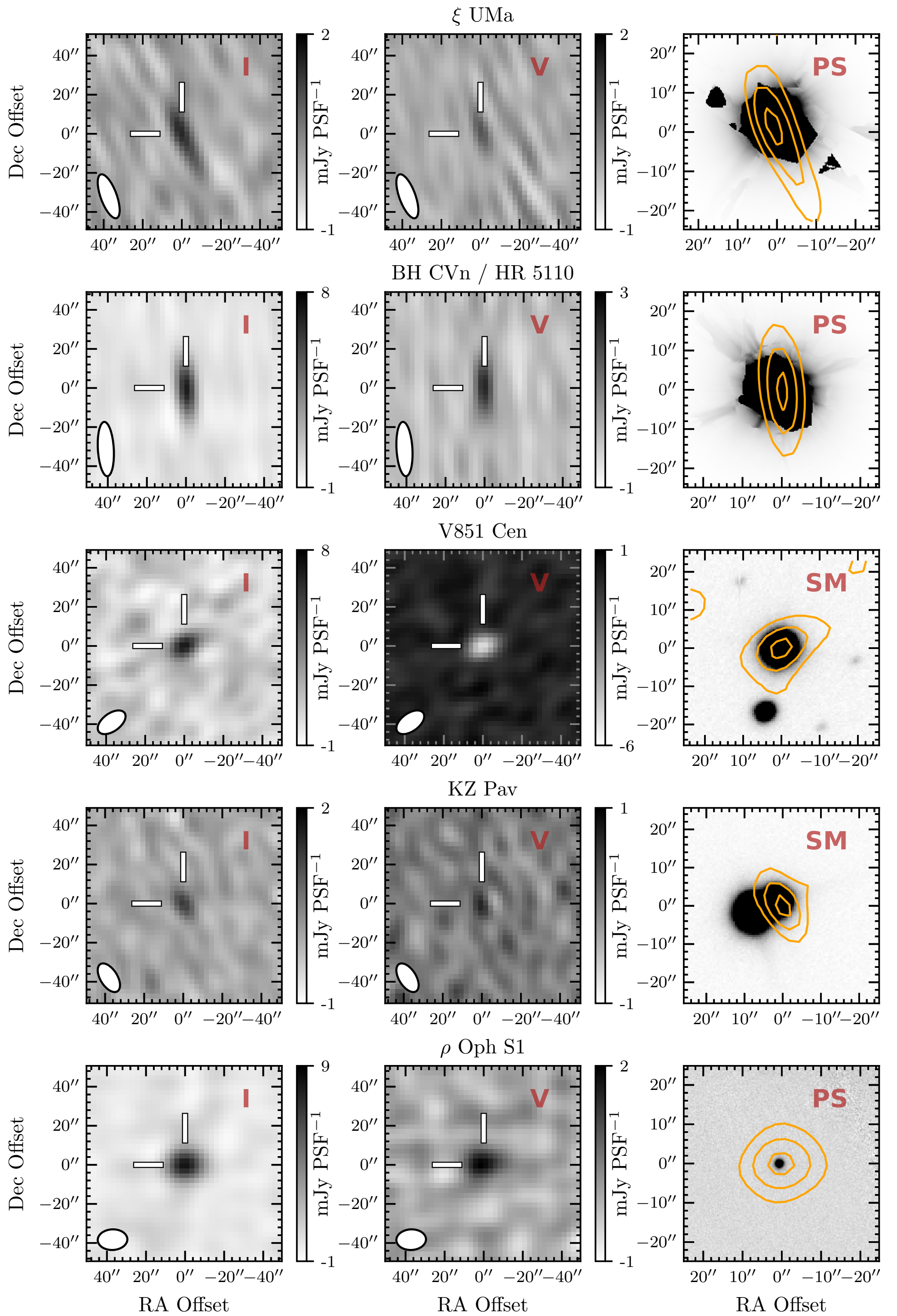

Figure 2.7: Images of ξ UMa, BH CVn, V851 Cen, KZ Pav, and ρ Oph S1. Details as in Figure 2.3.

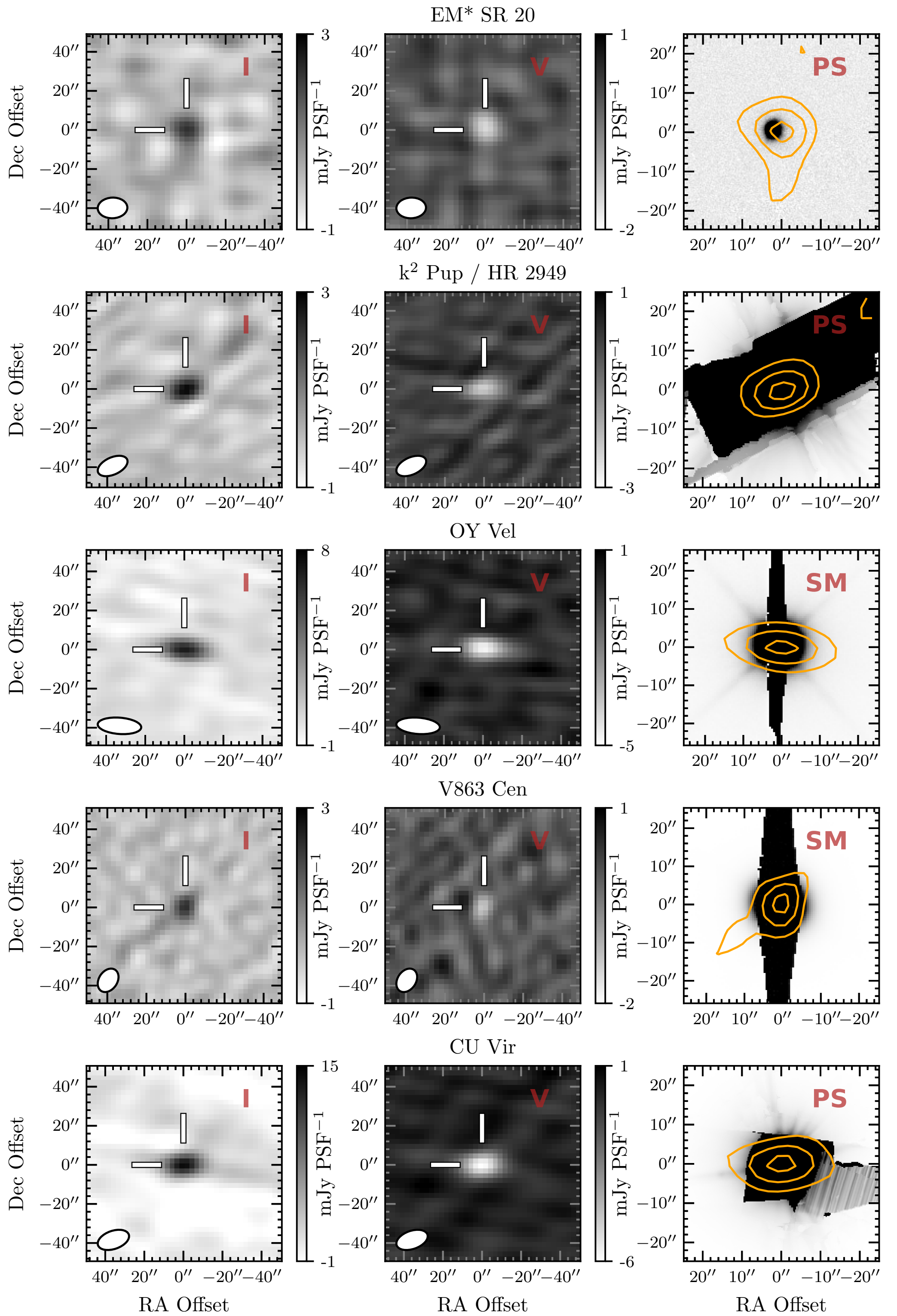

Figure 2.8: Images of EM* SR 20, k^2 Pup, OY Vel, V863 Cen, and CU Vir. Details as in Figure 2.3.

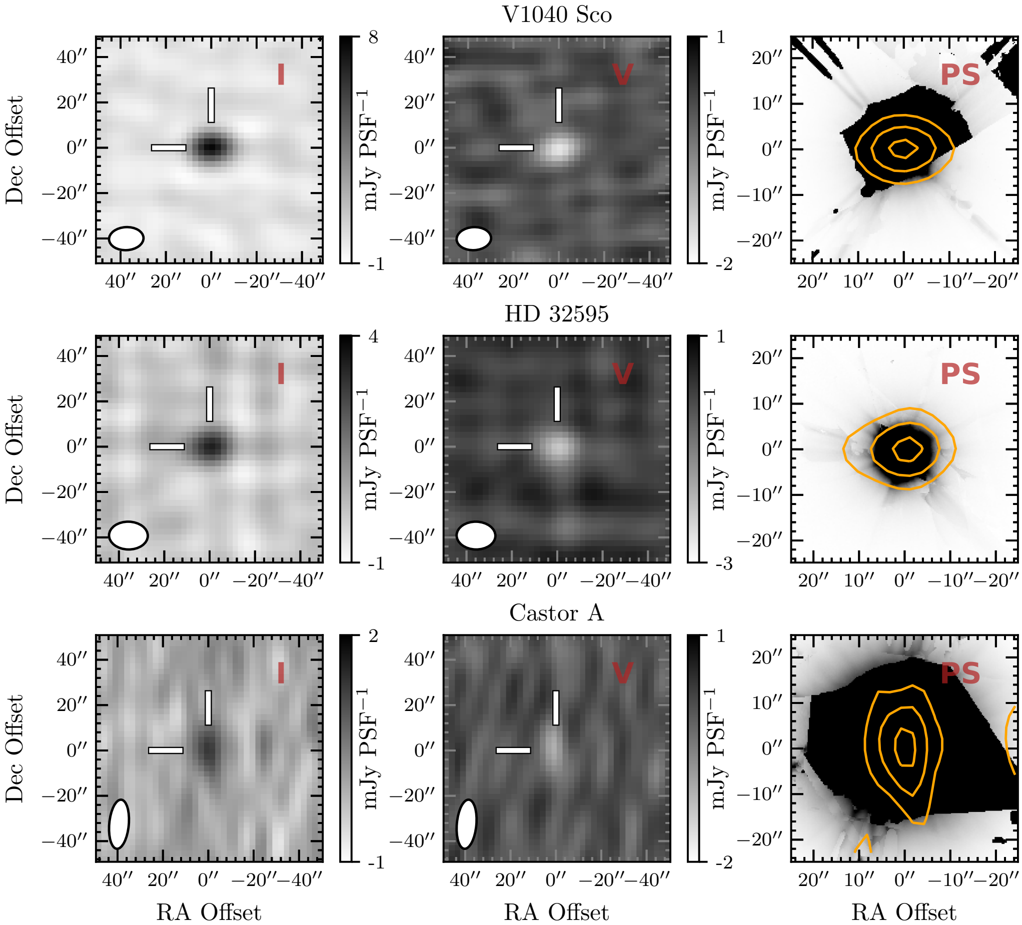

Figure 2.9: Images of V1040 Sco, HD 32595, and Castor A. Details as in Figure 2.3.

sub-components. The cooler secondary component demonstrates X-ray emission (Ball et al. 2005) attributed to activity induced by a 3.98 d orbit with one of its sub-components. This system has been frequently targeted by radio observations (Spangler et al. 1977; Morris & Mutel 1988; Drake et al. 1989, 1992; Bastian et al. 2000) but no detections have previously been reported. The system includes a T8.5 brown dwarf in a wide orbit (Wright et al. 2013), though this companion is separated by 8′.5 from our radio detection and cannot explain the observed emission.

BH CVn / HR 5110 (see Figure 2.7) is an F2IV/K2IV binary known to demonstrate large X-ray flares (Graffagnino et al. 1995), and is one of the most radio active RS CVn systems. VLBI observations at 15.4 GHz show radio emission originating from the K-type secondary (Abbuhl et al. 2015), which is typically unpolarised at 1.5 GHz and consistently right handed at higher frequencies (White & Franciosini 1995). Non-eclipsing RS CVn systems such as this typically demonstrate a reversal in the polarisation sense between 1.4–5 GHz (Mutel et al. 1987), which is consistent with our left handed detection at 887.5 MHz. Our detection is 34 % circularly-polarised, slightly above the 20 % levels detected at higher frequencies (White &

Franciosini 1995).

V851 Cen (see Figure 2.7) is a K0III RS CVn binary with chromospheric activity in both Hα and Ca II H and K lines (Cincunegui et al. 2007), and has previously demonstrated X-ray variability (Kashyap & Drake 1999; Haakonsen & Rutledge 2009; Kiraga 2012). The system has been targeted in two radio surveys due to the chromospheric activity (Collier et al. 1982; Slee et al. 1987) but was undetected.

KZ Pav (see Figure 2.7) is a F6V/K4IV Algol binary of the EA2-type, and has previously demonstrated variable radio emission at 8.4 GHz with one 4.8 ± 1.4 mJy detection in 12 epochs (Slee et al. 1987). The star has also been observed at 4.9 GHz with persistent 0.3 ± 0.1 mJy detections over a 24 hour period (Budding et al. 2001). Both detections correspond to a brightness temperature of order 10^8 K assuming emission originates from the inter-binary region.

2.5.3 Young Stellar Objects

We identify two young stellar objects within our sample. Pre-main sequence stars are magnetically-active and known to produce both highly polarised coherent emission (Smith et al. 2003) and non-thermal gyrosynchrotron emission (Andre 1996). Non-thermal emission is less commonly observed in classical T-Tauri (CTT) stars presumably due to absorption in the ionised circumstellar wind, though exceptions exist associated with extended magnetospheric structures such as the non-thermal radio knots in the jets of DG Tau (Ainsworth et al. 2014). Notes on individual sources are presented below.

ρ **Oph S1** (see Figure 2.7) is a B3 T-Tauri star in the Rho Ophiuchi cloud complex with a kilogauss globally organised magnetic field, and is a persistent radio source with a faint $20''$ wide halo and circularly-polarised core (Falgarone & Gilmore 1981; Andre et al. 1988). A VLBI observation of this star at 4.985 GHz has resolved the core as an $8-15R_\odot$ region of optically-thin gyrosynchrotron emission with brightness temperature of order 10^8 K (Andre et al. 1991). We detect 23 % left circularly-polarised emission with $S_{888} = 8.17 \pm 0.28$ mJy PSF^{-1}, which is comparable to the 5 GHz and 15 GHz measurements by Andre et al. 1988.

EM* SR 20 (see Figure 2.8) is a binary CTT system in the Rho Ophiuchi cloud complex, with the G7 primary embedded in a protostellar disk (McClure et al. 2008). This star has been targeted at millimetre wavelengths for cold dust continuum emission, but is undetected at a 35 mJy limit (Nürnberger et al. 1998).

2.5.4 Magnetic Chemically Peculiar Stars

Compared to later-type stars, magnetically driven, non-thermal emission is less common in hot stars, presumably due to the lack of an interior convective zone. The exception are the MCP stars, which have strong, globally organised magnetic fields, and have been observed to produce both gyrosynchrotron emission driven by equatorial current sheets (Linsky et al. 1992), and coherent auroral emission (Trigilio et al.

2011). We identify five MCP stars within our sample with polarisation fractions between 22–70 %. Notes on individual sources are presented below.

k^2 Pup / HR 2949 (see Figure 2.8) is a helium-weak B3IV star with kilogauss surface magnetic fields and helium spectral line variability suggestive of chemically peculiar spots, in analogue to the cooler Bp/Ap stars (Shultz et al. 2015). There are no previously reported radio detections of this star.

OY Vel (see Figure 2.8) is an ApSi magnetic chemically peculiar star and an α^2 CVn variable with no previously reported radio detections.

V863 Cen (see Figure 2.8) is a chemically peculiar B6IIIe helium-strong star with kilogauss surface magnetic fields (Briquet et al. 2004; Kochukhov & Bagnulo 2006) and no previously reported radio emission. Radio detections of Be stars are typically attributed to interactions between stellar wind outflows and a circumstellar disk resulting in free-free emission with low fractional polarisation, though a few notable detections are suggestive of a non-thermal mechanism (Dougherty et al. 1991; Skinner et al. 1993). Our detection is inconsistent with free-free emission, with 60 % left circularly-polarised emission likely driven by a non-thermal mechanism.

CU Vir (see Figure 2.8) is an ApSi α^2 CVn variable, and a well known radio-loud magnetic chemically peculiar star. Quiescent gyrosynchrotron emission with rotationally modulated variability has been observed from CU Vir (Leto et al. 2006), as well as two 100 % right circularly-polarised pulses that consistently repeat each rotation period (Trigilio et al. 2000; Ravi et al. 2010; Lo et al. 2012) and are attributed to ECM emission.

V1040 Sco (see Figure 2.9) is a helium-strong B2.5V star with a kilogauss global magnetic field, and is the most rapidly rotating magnetic B star known (Grunhut et al. 2012). This star has been detected at radio frequencies from 1.4 to 292 GHz (Condon et al. 1998; Murphy et al. 2010; Leto et al. 2018), with persistent emission attributed to gyrosynchrotron emission in the rigidly rotating magnetosphere. We measure a total intensity flux density of $7.87 \pm 0.20\,\mathrm{mJy\,PSF^{-1}}$ which is in agreement with that expected from extrapolation of the gyrosynchrotron spectrum to 887.5 MHz. Leto et al. (2018) measure circular polarisation of order 10 % at 44 GHz decreasing to order 5 % at 6 GHz, undergoing a sign reversal from left handed at high frequency to right handed below ∼20 GHz. This is also in agreement with our measurement of 22 % right handed circular polarisation.

2.5.5 Hot Spectroscopic Binaries

Two stars in our sample are hot, early-type stars that lack identified global magnetic fields or chemical peculiarities, and which have an unclassified spectroscopic binary companion. Chemically regular early-type stars are not expected to generate flares due to the lack of a conventional dynamo (Pedersen et al. 2017), and do not demonstrate other common features associated with non-thermal, polarised radio emission. Notes on individual sources are presented below.

HD 32595 (see Figure 2.9) is a spectroscopic binary with a chemically regular B8 primary, and no previously reported radio detections.

Castor (see Figure 2.9) is a triple binary system, where Castor A and B are both spectroscopic binaries consisting of A-type primaries and dMe secondaries, and Castor C is a binary dMe system. The Castor A system has been detected previously at 1.4 GHz, 4.9 GHz, and 8.5 GHz (Schmitt et al. 1994). Our detection is separated by $0\farcs83$ from Castor A and $3\farcs94$ from Castor B, so the emission is likely associated with one of the stars in Castor A.

2.6 Discussion

2.6.1 Emission Mechanism

We calculated the brightness temperature of our detections according to

$$T_B = \frac{S_{888} c^2}{2\pi k_B \nu^2} \frac{D^2}{R_e^2}, \tag{2.2}$$

where k_B is the Boltzmann constant, $\nu = 887.5$ MHz is the observing frequency, R_e is the length scale of an assumed emission region and D is the stellar distance. We have assumed an upper limit to the emission region of $R_e = 3R_\star$ for detections associated with single stars, and three times the binary separation distance for interacting binary systems, except where the emission region has been previously determined with VLBI. As the true emission region may be smaller than our assumed upper limit, the derived brightness temperature for each of our detections are lower limits, and range from 10^6–10^{12} K.

In Figure 2.10 we show the position of our detections in a brightness temperature–fractional polarisation phase space. We show empirical models of the maximum brightness temperature of optically-thin, non-thermal gyrosynchrotron emission derived from Dulk (1985) at viewing angles of 20–80°, and electron power-law energy index δ of $2 - 5$. Each model is limited to the cyclotron harmonic number range $10 < \omega/\omega_c < 100$, with harmonic number increasing monotonically along the curves from lower right to upper left.

The fractional polarisation of optically-thick gyrosynchrotron emission is typically less than 20 % (Dulk & Marsh 1982) and insufficient to explain the majority of our detections. The RS CVn and Algol type binary detections are consistent with optically-thin, non-thermal gyrosynchrotron emission, while the majority of K- and M- dwarf, YSO, and MCP star detections occupy a region with T_B too high to explain the observed fractional polarisation, and are likely driven by a coherent emission process.

Our upper limit assumptions on the emission region require that the orientation of the magnetic field varies significantly in the source region, which in turn limits the fractional circular polarisation due to contributions from both left and right hand

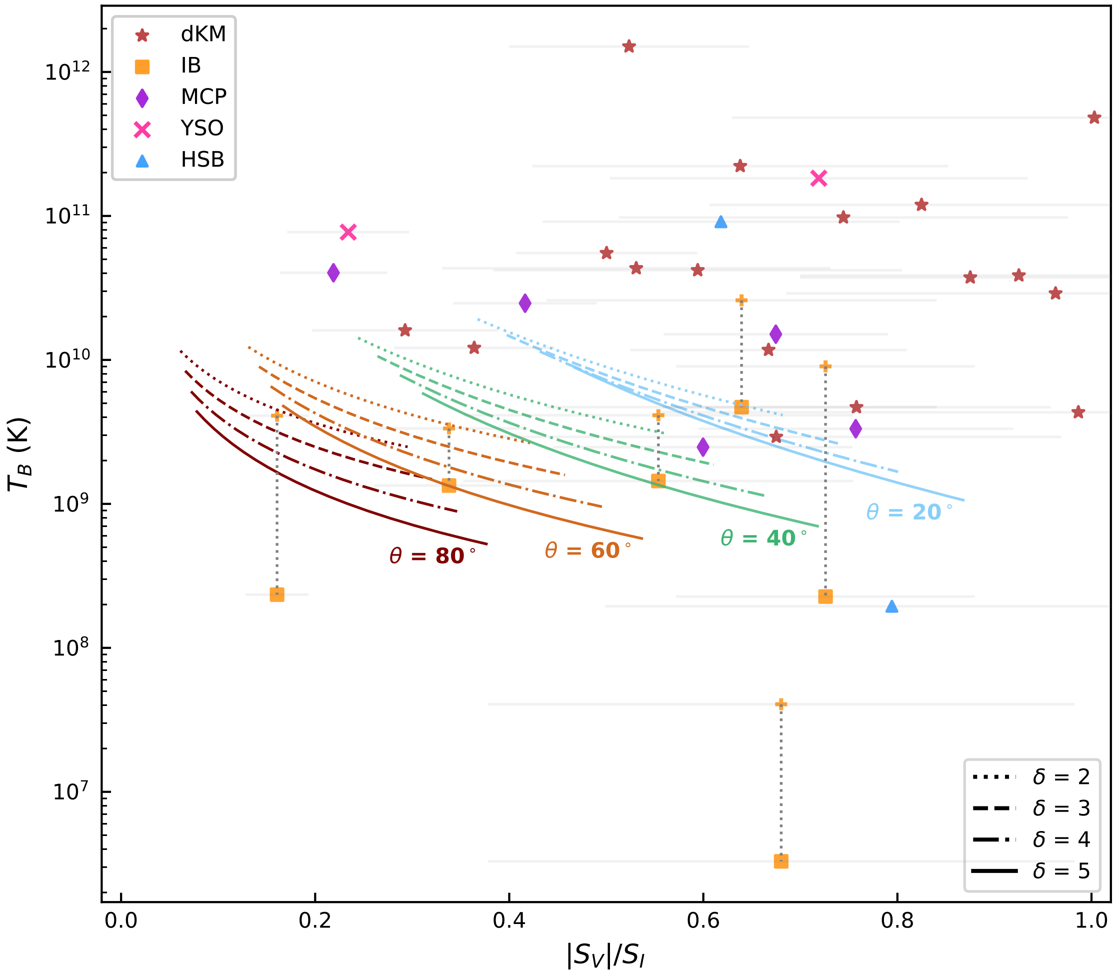

Figure 2.10: Phase diagram of brightness temperature and fractional polarisation. Brightness temperatures correspond to lower limits assuming the observed emission originates from a $3R_\star$ disk, with K- and M-dwarfs represented by red circles, YSOs by green stars, MCP stars by purple diamonds, and hot spectroscopic binaries as blue rightward pointing triangles. For RS CVn and Algol binaries we show two brightness temperatures: yellow squares represent emission originating from the inter-binary region and yellow crosses represent a $3R_\star$ disk. Empirical models (Dulk 1985) are plotted approximating the maximum brightness temperature of optically-thin gyrosynchrotron emission for viewing angles θ of 20°, 40°, 60°, and 80°, and electron power law energy indices of $\delta = 2 - 5$.

polarised emission. Our detections with high degrees of circular polarisation are therefore likely driven by sources in a much smaller region with a correspondingly higher brightness temperature, further suggesting a coherent emission process.

2.6.2 Detection Rates

We detected 33 radio stars within the covered RACS survey area of 34 159 deg^2 with detections evenly distributed on the sky, corresponding to a surface density of

$9.66^{+3.91}_{-3.01} \times 10^{-4}\,\mathrm{deg}^{-2}$ with errors given by 95 % Poisson confidence intervals. Our survey was limited to $f_p > 0.06$ due to the lack of on-axis polarisation leakage calibration which has now been applied to available RACS data, and we further restricted our search to positional offsets between Stokes I and V of less than $2''$ to reduce contamination from imaging artefacts. Our detection rate is therefore a lower limit to the surface density of radio stars at 887.5 MHz.

As all detected stars are located within a distance of 150 pc, we assume they sample a Euclidean population of radio stars and follow a cumulative flux density distribution $N(>S) \propto S^{-3/2}$. The FIRST survey for radio stars (Helfand et al. 1999) detected 26 stars in a survey area of 5000 deg^2 above a flux density of 0.7 mJy. Once scaled to the RACS sensitivity, this corresponds to a surface density of $2.18^{+1.73}_{-1.10} \times 10^{-3}\,\mathrm{deg}^{-2}$ which is comparable to our result.

We extrapolate the number of radio stars detected in this survey to hypothetical future surveys with ASKAP. Scaling our results to a deep 20 µJy PSF^{-1} RMS survey of the entire sky south of $\delta = +41°$ implies a surface density of detectable radio stars of $4.27^{+0.23}_{-0.22} \times 10^{-2}\,\mathrm{deg}^{-2}$ and $1400 - 1500$ total detections. A shallow but frequent survey covering 10 000 deg^2 to an RMS noise of 0.5 mJy PSF^{-1} should produce $6-20$ detections per epoch with a surface density of $1.17^{+0.89}_{-0.57} \times 10^{-3}\,\mathrm{deg}^{-2}$, and would probe the duty cycle and luminosity distribution of individual variable radio stars.

As the majority of our K- and M-type dwarf detections are inconsistent with incoherent gyrosynchrotron emission and are likely driven by coherent bursts, we also calculate the surface density of these detections alone for comparison to previous flare rate estimates in the literature. We detected 18 K- and M-type dwarfs, assuming the detection of Castor A can be attributed to the dMe companion, which results in a surface density of radio-loud cool dwarfs at 887.5 MHz of $5.27^{+3.06}_{-2.15} \times 10^{-4}\,\mathrm{deg}^{-2}$. In comparison, Villadsen & Hallinan (2019) report an M-dwarf transient density at 1.4 GHz of $2.26 \times 10^{-3}\,\mathrm{deg}^{-2}$ once scaled to the RACS sensitivity, which implies RACS should produce ∼80 M-dwarf detections. This difference may reflect an increase in cool star radio activity at 1.4 GHz, or the selection of six highly active M-dwarfs in the Villadsen & Hallinan (2019) study which are not representative of radio flare rates in the larger population.

2.7 Conclusions

We have completed the first all-sky circular polarisation search for radio stars at centimetre wavelengths within the Rapid ASKAP Continuum Survey, identifying 10 known radio stars and a further 23 with no previous radio detection. Our sample includes late-type dwarfs, interacting and chromospherically active binaries, young stellar objects, and magnetic chemically peculiar stars, demonstrating the variety of magnetically-active stars detectable with this technique. Many of our detections are highly polarised with brightness temperatures that are inconsistent with an incoherent emission mechanism. These stars are attractive targets for followup observations to determine the emission mechanism and further constrain the magnetospheric properties of the emission environment.

This survey represents a sample of polarised radio stars without any other selection bias and implies a lower limit to the surface density of radio stars above 1.25 mJy at 887.5 MHz of $9.66^{+3.91}_{-3.01} \times 10^{-4}\,\mathrm{deg}^{-2}$. Application of on-axis polarisation calibration to publicly released ASKAP data will allow lower fractional polarisation and fainter emission to be detected, and extension of this search technique to future ASKAP surveys will produce a significantly larger sample and the potential for detections in multiple epochs. These observations will present an opportunity to determine improved population statistics for the stellar parameters associated with non-thermal radio emission, and to study burst rates and energetics for thousands of stars.

Acknowledgements

We thank the anonymous referee for feedback that strengthened this work. We also thank Phil Edwards and Alec Thomson for helpful comments and suggestions. TM acknowledges the support of the Australian Research Council through grant FT150100099. JP, AZ, and JKL are supported by Australian Government Research Training Program Scholarships. DLK was supported by NSF grant AST-1816492. The Australian Square Kilometre Array Pathfinder is part of the Australia Telescope National Facility which is managed by CSIRO. Operation of ASKAP is funded by the Australian Government with support from the National Collaborative Research Infrastructure Strategy. ASKAP uses the resources of the Pawsey Supercomputing Centre. Establishment of ASKAP, the Murchison Radio-astronomy Observatory and the Pawsey Supercomputing Centre are initiatives of the Australian Government, with support from the Government of Western Australia and the Science and Industry Endowment Fund. We acknowledge the Wajarri Yamatji as the traditional owners of the Murchison Radio-astronomy Observatory site. The International Centre for Radio Astronomy Research (ICRAR) is a Joint Venture of Curtin University and The University of Western Australia, funded by the Western Australian State government. Parts of this research were supported by the ARC Centre of Excellence for All Sky Astrophysics in 3 Dimensions (ASTRO 3D), through project number CE170100013. This research made use of the following PYTHON packages: ASTROPY (Astropy Collaboration et al. 2013, 2018), a community-developed core Python package for Astronomy, MATPLOTLIB (Hunter 2007), a Python library for publication quality graphics, NUMPY (van der Walt et al. 2011; Harris et al. 2020), and PANDAS (Wes McKinney 2010; McKinney 2011).

Data Availability

The data analysed in this work are accessible through the CSIRO ASKAP Science Data Archive (CASDA; Chapman et al. 2017) under project code AS110. Note that the images used in this work may have properties that differ slightly from the publicly released versions.

Chapter 3

Multi-epoch sampling of the radio star population with the Australian SKA Pathfinder

JOSHUA PRITCHARD,[1,2,3] TARA MURPHY,[1,3] GEORGE HEALD,[4] MICHAEL S. WHEATLAND,[1] DAVID L. KAPLAN,[5] EMIL LENC,[2] ANDREW O'BRIEN,[2,5] ZITENG WANG,[1,3]

[1]Sydney Institute for Astronomy, School of Physics, University of Sydney, NSW 2006, Australia
[2]CSIRO Space and Astronomy, PO Box 76, Epping, NSW 1710, Australia
[3]ARC Centre of Excellence for Gravitational Wave Discovery (OzGrav), Hawthorn, Victoria, Australia
[4]CSIRO Space and Astronomy, PO Box 1130, Bentley, WA 6102, Australia
[5]Department of Physics, University of Wisconsin-Milwaukee, P.O. Box 413, Milwaukee, WI 53201, USA

This Chapter was published as Pritchard et al. (2024), doi:10.1093/mnras/stae127. All content included in this chapter is my own work unless otherwise stated—including writing the manuscript, production of tables and figures, development of the circular polarisation search code, candidate selection and classification, and analysis, with specific contributions from co-authors described below. Michael Wheatland provided guidance on the statistical framework presented in § 3.6.2, Ziteng Wang contributed to initial processing of the Stokes V images, and all other authors contributed to the observation, data reduction, and quality analysis of the VASTP-low data products that this work is based upon.

3.1 Abstract

The population of radio-loud stars has to date been studied primarily through either targeted observations of a small number of highly active stars or widefield, single-epoch surveys that cannot easily distinguish stellar emission from background extragalactic sources. As a result it has been difficult to constrain population statistics such as the surface density and fraction of the population producing radio emission in a particular variable or spectral class. In this paper we present a sample of 36 radio stars detected in a circular polarisation search of the multi-epoch Variables and Slow Transients (VAST) pilot survey with ASKAP at 887.5 MHz. Through repeat sampling of the VAST pilot survey footprint we find an upper limit to the duty cycle of M-dwarf radio bursts of 8.5 %, and that at least 10 ± 3 % of the population should produce radio bursts more luminous than $10^{15}\,\mathrm{erg\,s^{-1}\,Hz^{-1}}$. We infer a lower limit on the long-term surface density of such bursts in a shallow $1.25\,\mathrm{mJy\,PSF^{-1}}$

sensitivity survey of $9^{+11}_{-7} \times 10^{-3}$ deg^{-2} and an instantaneous radio star surface density of $1.7 \pm 0.2 \times 10^{-3}$ deg^{-2} on 12 min timescales. Based on these rates we anticipate $\sim$200 $\pm$ 50 new radio star detections per year over the full VAST survey and $41\,000^{+10\,000}_{-9\,000}$ in next-generation all-sky surveys with the Square Kilometre Array.

3.2 Introduction

A wide variety of stellar systems produce magnetically driven non-thermal radio emission, featuring a high degree of fractional circular polarisation and large brightness temperatures. In analogy to solar radio activity, K- and M-type dwarfs produce slowly varying or "quiescent" emission as well as stochastic bursts associated with magnetic reconnection and space weather (e.g. Villadsen & Hallinan 2019; Zic et al. 2020). Close-in RS Canum Venaticorum (RS CVn) and Algol binary systems produce both quiescent and bursty emission associated with the coupling of their magnetospheres (e.g. Morris & Mutel 1988; White & Franciosini 1995; Toet et al. 2021), which feature strong magnetic fields due to tidally induced rapid rotation of the component stars. Non-thermal emission has also been observed from young stellar objects (YSOs), as magnetic structures connecting the star and proto-planetary disk undergo co-rotation breakdown and reconnect (e.g. Andre 1996). B- and A-type main-sequence stars are too hot to support a convective zone and hence lack a conventional $\alpha - \Omega$ or α^2 dynamo mechanism to generate strong magnetic fields; however highly circularly polarised pulses are none the less observed from a small number of strongly magnetic early-type chemically peculiar stars (MCPs) (e.g. Trigilio et al. 2000; Das et al. 2022). See reviews by Güdel (2002) and Matthews (2019) for comprehensive overviews of the radio properties of each of these systems.

In addition to Solar-type radio activity, cool stars are known to produce highly circularly polarised pulses of radio emission analogous to Jupiter's auroral decametric radiation. These pulses have been observed from early M-dwarfs (e.g. Zic et al. 2019b; Bastian et al. 2022) to ultracool dwarfs (e.g. Hallinan et al. 2006; Lynch et al. 2015; Dobie et al. 2023) and brown dwarfs (e.g. Route & Wolszczan 2012; Williams & Berger 2015; Kao et al. 2016, 2018; Vedantham et al. 2020b, 2023; Rose et al. 2023) at the end of the main sequence where stellar interiors become fully convective. Auroral pulses are widely believed to be generated by the electron cyclotron maser instability (ECMI; Treumann 2006), a coherent emission process in which gyro-phase angle bunching of electrons along with a positive gradient in the electron velocity distribution provides free energy to drive the amplification of circularly polarised radio emission. The ECMI operates at the local relativistic cyclotron frequency $\omega_c = \frac{eB}{\gamma m_e c}$ where e is the elementary charge, m_e is the electron mass, B is the magnetic field strength, γ is the Lorentz factor, and c is the speed of light. Auroral radio pulses thus offer a direct measurement of the magnetic field strength in the source region, providing insights into the origin and evolution of magnetic fields in cool stars. This information helps to constrain the plausible dynamo mechanisms responsible for generating strong magnetic fields (e.g. Kao et al. 2016), map the configuration of active coronal loops in the magnetosphere (e.g. Lynch et al. 2015), and inform models of the evolution and dissipation of magnetic fields by stellar winds and space weather (e.g. Vidotto et al. 2012).

Most of the previous studies of stellar radio activity have been limited to targeted observations and monitoring campaigns of stars with previously identified indicators of magnetic activity; such as strong radio activity (e.g. Villadsen & Hallinan 2019), flaring or variability in optical, ultra-violet, and X-ray bands (e.g. White et al. 1989), or the presence of chromospheric emission or absorption lines (e.g. Slee et al. 1987). While these studies are ideal for modeling the complex electrodynamic environments that drive the radio properties of individual systems, the inherent selection bias prevents inference of statistical properties in the unobserved population, such as the burst luminosity and rate distributions, and the fraction of the population producing radio activity. For example White et al. (1989) found a radio-loud fraction of 40 % in a survey of optical flare stars within 10 pc at 6 cm and 20 cm wavelengths, though this result may over-estimate the radio-loud fraction by ignoring the many late-type stars without optical flare activity that have been discovered to demonstrate similar radio burst phenomena (e.g. Pritchard et al. 2021; Callingham et al. 2021a). Villadsen & Hallinan (2019) surveyed a sample of five active M-dwarfs at 1–1.4 GHz over 13 epochs and detected 22 coherent radio bursts inferring a burst duty cycle of 25 %, though again the behaviour of these highly active targets is difficult to extrapolate to the unobserved population.

A small number of widefield, untargeted searches for radio stars have been conducted, though the high surface density of active galactic nuclei (AGN) typically results in a large number of false-positive matches to foreground stars. Helfand et al. (1999) searched 5000 deg^2 of high Galactic latitude sky to a sensitivity of 0.7 $\mathrm{mJy\,PSF}^{-1}$ in the VLA Faint Images of the Radio Sky at Twenty-cm (FIRST; Becker et al. 1995) survey identifying 26 radio stars. Kimball et al. (2009) further explored FIRST identifying 112 matches to spectrally confirmed stars in the Sloan Digital Sky Survey (SDSS; Adelman-McCarthy et al. 2008), though a similar number of matches are estimated due to chance alignment with background radio galaxies. Vedantham et al. (2020a) crossmatched radio sources detected by the LOw-Frequency ARray (LOFAR; van Haarlem et al. 2013) in the LOFAR Two-Metre Sky Survey (LoTSS; Shimwell et al. 2017) with nearby stars in Gaia Data Release 2 (Andrae et al. 2018), discovering an M-dwarf producing coherent, circularly polarised auroral emission at metre wavelengths.

Circular polarisation searches have been demonstrated as an excellent method for unambiguous identification of stellar radio bursts, as the synchrotron emission produced by AGN is typically at most 2 % circularly polarised (Macquart 2002), and therefore the false-positive associations that dominate widefield searches in total intensity are negligible in circular polarisation. The first all-sky circular polarisation transient survey was conducted by Lenc et al. (2018) at 200 MHz with the Murchison Widefield Array (MWA; Bowman et al. 2013), and resulted in detection of 33 previously known pulsars and two tentative star detections. We previously reported results (Pritchard et al. 2021) from an all-sky circular polarisation search at 887.5 MHz with the Australian Square Kilometre Array Pathfinder (ASKAP; Johnston et al. 2008; Hotan et al. 2021) as part of the low-band Rapid ASKAP

Continuum Survey (RACS-low; McConnell et al. 2020), with detection of 33 stars including 23 which had not been previously detected. Callingham et al. (2023) conducted a widefield circular polarisation search at 144 MHz as part of LoTSS with detection of 37 stars, including a sample of 19 radio loud M-dwarfs (Callingham et al. 2021a) and 14 RS CVn systems (Toet et al. 2021).

Due to the variable nature of stellar radio bursts, population studies are fundamentally limited in single epoch surveys, where a non-detection may either represent a radio quiet star or simply a low burst duty cycle and thus only provide an upper limit on the burst rate of $\sim 1/T_{\text{obs}}$ where T_{obs} is the observing time. Telescopes such as LOFAR, ASKAP, and the MWA have large fields of view enabling widefield single epoch surveys with a significant overlap in sky coverage between individual pointings (e.g. Lenc et al. 2018; Pritchard et al. 2021; Callingham et al. 2021a, 2023; Duchesne et al. 2023), and therefore some variability information is provided for stars detected in these regions. However without dedicated multi-epoch observations these surveys are only able to acquire a small number of repeat samples within a subset of the survey footprint, making it difficult to extrapolate detection rates to the undetected population. In contrast multi-epoch surveys can both directly measure the high end of the burst rate distribution from repeat detection counts, and more strongly constrain the low end through statistical analysis of non-detection rates. These parameters are important inputs to forecasts of the surface density of stellar radio bursts in current and next-generation radio transient surveys.

In this paper we present the results of a multi-epoch circular polarisation search for radio stars across RACS-low and the low-band of the VAST Pilot Survey (VASTP-low; Murphy et al. 2021). In § 3.3 we summarise the RACS-low and VASTP-low observations and data processing; in § 3.4 we describe our circular polarisation search procedure and candidate selection; in § 3.5 we present the radio luminosity and polarisation properties of our sample of detected stars; and in § 3.6 we use the subset of stellar detections within the repeat-sampled VASTP-low footprint to derive statistical properties of the radio loud M-dwarf population.

3.3 Observations and Data Reduction

3.3.1 Standard Processing

Full details of RACS-low and VASTP-low observations and standard processing are provided in McConnell et al. (2020) and Murphy et al. (2021) respectively, but we summarise them here. Observations from both RACS-low and VASTP-low use a 6×6-beam square footprint with a $66\,\text{deg}^2$ field of view at a central frequency of 887.5 MHz with 288 channels each 1 MHz wide. RACS-low and VASTP-low observations were acquired with 15 min and 12 min integrations reaching a median RMS noise σ_I of $250\,\mu\text{Jy PSF}^{-1}$ and $240\,\mu\text{Jy PSF}^{-1}$ respectively. The observing parameters are summarised in Table 3.1, and the temporal and sky coverage of each epoch is listed in Table 3.2.

Each ASKAP antenna is equipped with a Phased Array Feed (PAF; Hotan et al.

Table 3.1: Summary of RACS-low and VASTP-low observing parameters.

Property	Value	Survey
Central Frequency	887.5 MHz	
Bandwidth	288 MHz	
Integration Time	12 min	VASTP-low
	15 min	RACS-low
Median RMS Noise	240 µJy PSF^{-1}	VASTP-low
	250 µJy PSF^{-1}	RACS-low
Polarisation Leakage	0.6 % (V positive)	VASTP-low
	0.7 % (V negative)	VASTP-low
	0.5 % (V positive)	RACS-low
	0.6 % (V negative)	RACS-low
Astrometric Accuracy	$\Delta\alpha\cos\delta = -0.19 \pm 0.53''$	VASTP-low
	$\Delta\delta = 0.07 \pm 0.48''$	VASTP-low
	$\Delta\alpha\cos\delta = -0.60 \pm 0.50''$	RACS-low
	$\Delta\delta = 0.10 \pm 0.50''$	RACS-low
PSF Central Lobe (FWHM)	$B_{\rm min} = 11.3 \pm 0.6''$	VASTP-low
	$B_{\rm max} = 13.7 \pm 4.2''$	VASTP-low
	$B_{\rm min} = 11.8 \pm 0.9''$	RACS-low
	$B_{\rm max} = 18.0 \pm 4.3''$	RACS-low

2014; McConnell et al. 2016) which allows the formation of 36 dual linear polarisation beams on the sky. All four cross-correlations are recorded allowing calibration of the frequency-dependent XY phases and full reconstruction of Stokes I, Q, U, and V images. The antenna roll-axis is adjusted throughout each observation to maintain orientation of the linear feeds with respect to the celestial coordinate frame so that no correction for parallactic angle is required, and keeping the beam footprint fixed on the sky. ASKAP data are calibrated and imaged with the ASKAPsoft package (Cornwell et al. 2011; Guzman et al. 2019) which generates full Stokes image products and uses the selavy (Whiting & Humphreys 2012) source finder package to extract a catalogue of 2D Gaussian source components from the Stokes I images. We determined the signal-to-noise dependent astrometric uncertainty of extracted selavy components following Condon (1997) as

$$\sigma_\theta = \frac{2\theta_m}{\frac{S_I}{\sigma_I}\sqrt{8\ln 2}}, \tag{3.1}$$

where θ_m is the component major axis and σ_I is the local RMS noise. We added this uncertainty in quadrature to the astrometric accuracies listed in Table 3.1 to determine the positional uncertainty of each radio source, with uncertainties of $2''.3$ and $3''.1$ for a $5\sigma_I$ detection in RACS-low and VASTP-low respectively.

3.3.2 Stokes V Processing

We ran SELAVY on the Stokes V images with standard ASKAPSOFT settings, with two extractions to collect both positive and negative sources. Throughout this paper we adopt the IAU/IEEE convention for Stokes V, in which positive and negative Stokes V correspond to right and left handed circular polarisation respectively (Robishaw & Heiles 2021). We checked that our fluxes are consistent with this convention by comparison to a selection of 25 pulsars reported in Han et al. (1998) and Johnston & Kerr (2018) which are persistently detected with the same circular polarisation handedness at ∼1 GHz. All 25 pulsars are in agreement with our measured polarisation handedness after accounting for the opposite convention used in pulsar astronomy. We also checked the consistency of Stokes V sign across the duration of the pilot survey through the star HR 1099, an RS CVn binary system that is detected in every epoch and maintains a negative Stokes V sign in all detections. This is consistent with the expected polarisation of gyrosynchrotron emission from this system which is left handed below ∼1.5 GHz (White & Franciosini 1995).

We characterised the degree of polarisation leakage by crossmatching selavy components in Stokes I with their counterpart in Stokes V, requiring each match to have no neighbouring components within 30″, Stokes I flux density S_I of >100 mJy PSF^{-1}, and Stokes V flux density S_V greater than $5\sigma_V$ where σ_V is the local Stokes V RMS noise. We removed sources associated with stars and pulsars so that the sampled points are associated with AGN with no intrinsic circular polarisation, and are thus a measurement of the degree of polarisation leakage from Stokes I into Stokes V.

We made 28 149 leakage measurements from all images within the survey with 7 852 positive and 20 297 negative Stokes V measurements respectively. In Figure 3.1 we show the fractional circular polarisation of each leakage measurement as a function of angular distance to field centre along with the median leakage in 10 field centre distance bins. The larger count of negative leakage measurements is visible as a bias towards negative Stokes V leakage near to field centre at a level of ∼0.5 % with very few positive leakage measurements in this range. At distances of greater than ∼3° from field centre both positive and negative leakage begin to increase to a level of ∼1 % at ∼4° towards the field edges, and ∼3 % at ∼5° in the corners.

We transformed the position of each sample into the image-centred frame to visualise the leakage pattern across the ASKAP field of view. In Figure 3.2 we show these samples alongside a Gaussian Process regression fit to the data with the position of all star and pulsar detections overlaid. Within the central 3.75° from field centre the leakage has median positive and negative values of 0.6 % and −0.7 %. In this region the leakage pattern towards the edge of individual beams overlaps and suppresses the mosaiced leakage, with a small bias towards negative Stokes V caused by imperfect overlap due to uncertainty in the primary beam response pattern. The tile edges have no overlapping beams and a residual leakage pattern is visible alternating between positive and negative Stokes V. We note that more recent ASKAP observations such as the mid-band epoch of RACS at 1367.5 MHz (RACS-mid; Duchesne et al. 2023) implement widefield leakage corrections that remove both the bias and residual leakage pattern.

Table 3.2: Observing dates and sky coverage of VASTP-low epochs. Epochs labeled with an x only partially cover the survey footprint, see Murphy et al. (2021) for details.

Epoch	Start Date	End Date	Area (deg^2)	Fields
0^a	2019 Apr 25	2019 May 03	5 131	113
1	2019 Aug 27	2019 Aug 28	5 131	113
2	2019 Oct 28	2019 Oct 31	4 905	108
3x	2019 Oct 29	2019 Oct 29	2 168	43
4x	2019 Dec 19	2019 Dec 19	1 672	34
5x	2020 Jan 10	2020 Jan 11	3 818	81
6x	2020 Jan 11	2020 Jan 12	2 400	49
7x	2020 Jan 16	2020 Jan 16	1 666	33
8	2020 Jan 11	2020 Feb 01	5 097	112
9	2020 Jan 12	2020 Feb 02	5 097	112
10x	2020 Jan 17	2020 Feb 01	803	13
11x	2020 Jan 18	2020 Feb 02	695	11
12	2020 Jan 19	2020 Jun 21	5 100	112
13	2020 Aug 28	2020 Aug 30	5 028	104
17	2021 Jul 21	2021 Jul 24	5 131	114^b
19	2021 Aug 20	2021 Aug 24	5 131	115^b

[a] Listed values for epoch 0 are for the 113 RACS-low fields within the VASTP-low footprint.
[b] Epochs 17 and 19 include one and two repeat observations respectively, but have the same sky coverage as epoch 1.

3.4 Candidate Search

3.4.1 Candidate Selection

We generated associations between the extracted Stokes I and V components with a many-to-many crossmatch using a match radius of $6''$. Many-to-many association allows for one Stokes I component to match to multiple Stokes V components within the match radius (and vice versa), ensuring that all possible I-V associations within the match radius are considered at the cost of an increased number of false-positive associations. This choice is made to avoid missing edge cases in which a near neighbour in Stokes I matches on to the Stokes V component and produces a lower $|S_V|/S_I$ than the correct Stokes I component.

We then crossmatched the I-V associations between each epoch to track individual candidates over the duration of the survey. Beginning with an initial epoch A each I-V association is assigned a unique association ID. We then generate an initial many-to-many crossmatch of I-V associations between epoch A and the subsequent epoch B using the Stokes I coordinates with a $6''$ match radius.

Many-to-many association across N_e epochs results in $\mathcal{O}\left((n_I n_V)^{N_e-1}\right)$ total candidates, with n_I and n_V selavy components within the match radius in Stokes I

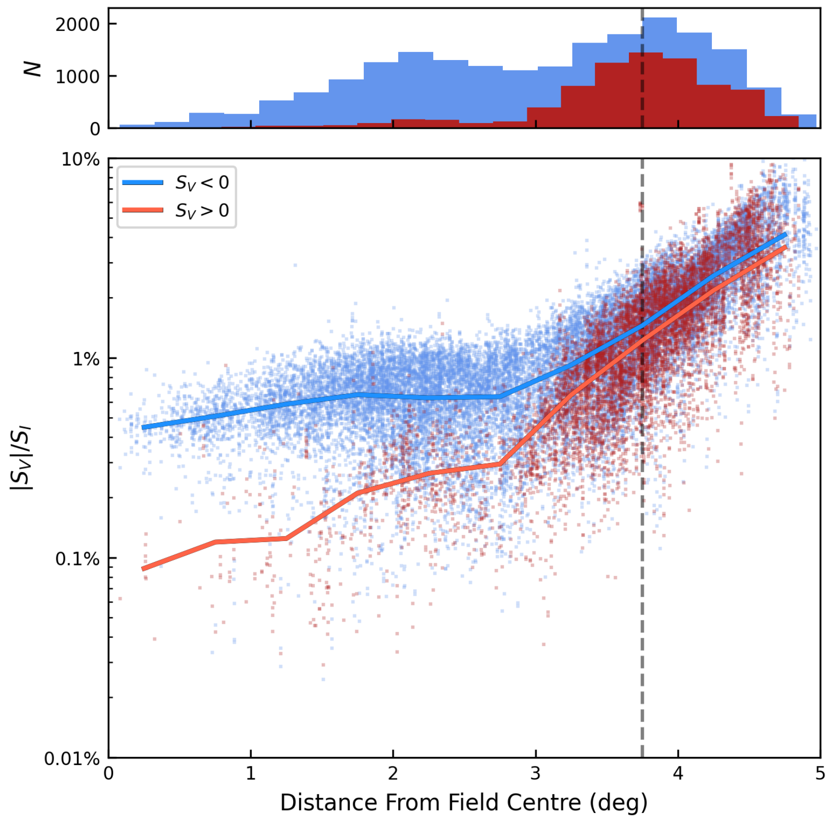

Figure 3.1: Leakage from Stokes I into V ($|S_V|/S_I$) as a function of angular distance from field centre. The points represent Stokes I-V matches between isolated point sources with $S_I > 100\,\mathrm{mJy\,PSF^{-1}}$ with red and blue corresponding to matches with positive and negative Stokes V flux respectively. The histograms show the distribution of positive and negative matches with angular distance with a bias towards negative leakage towards the field centre. The black dashed line indicates a field centre distance of 3.75°, within which the positive and negative leakage has median values of 0.6 % and −0.7 % respectively.

and V respectively. We de-duplicate these candidates by retaining only the A-B associations whose match distance is the minimum of all duplicate candidates such that there is no other copy of an epoch A or B I-V association with a closer match, reducing the number of candidates to $\mathcal{O}\,(\max(n_I, n_V))$. This step greatly reduces the number of artefacts produced around bright sources, where I-V associations between sidelobes shift position between epochs.

We create a running list of candidates for the epoch A-B associations including epoch A I-V associations with no match in epoch B, and also add all epoch B I-V associations with no match in epoch A, assigning a new association ID. Finally we re-calculate the average Stokes I coordinates of each candidate and use these to perform the next round of epoch-association. Using this procedure we performed association between the 15 epochs of VASTP-low, resulting in a list of 9 818 candidates. We then filtered this list to candidates both greater than 5σ in both Stokes I and V where σ is the local RMS noise, and with at least one I-V association with fractional circular

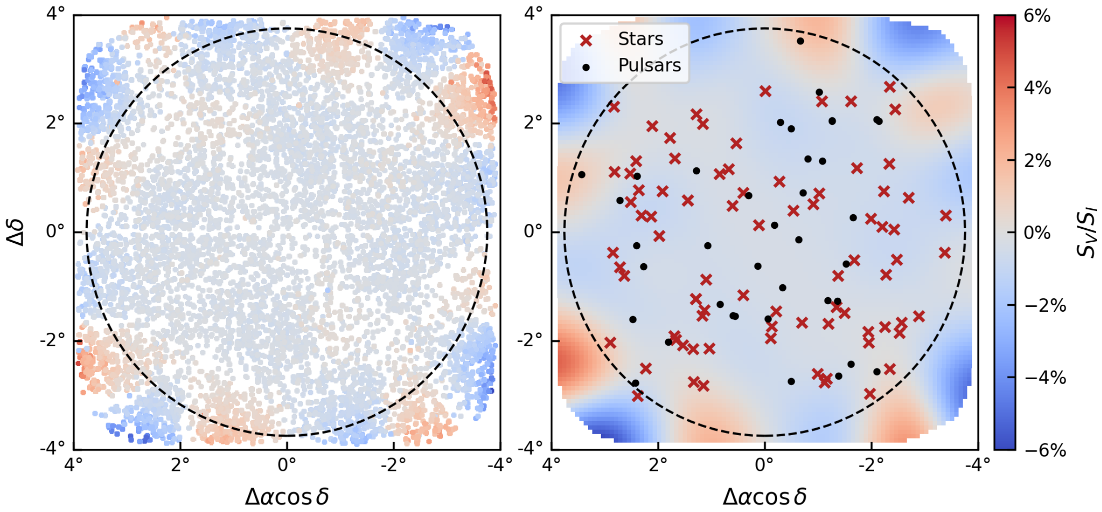

Figure 3.2: Map of leakage from Stokes I into Stokes V across the ASKAP field of view in VASTP-low. The left panel shows position and leakage of Stokes I-V matches in the field-centred frame. The right panel shows a Gaussian Process regression model fit to these measurements, with the positions of all star and pulsar detections overlaid. The black dashed circle indicates an angular distance from the field centre of 3.75°.

polarisation $|S_V|/S_I > 6$ percent, corresponding to 10 times the median polarisation leakage of Stokes I into V and three times the typical leakage of $\sim$2 % in image corners. Our final list contains 1 188 candidates.

3.4.2 Artefact Rejection

Through visual inspection of the Stokes I and V images we rejected I-V associations with artificially high $|S_V|/S_I$ caused by imaging artefacts and spurious noise. In Figure 3.3 we show a selection of example image cutouts of rejected artefacts as well as legitimately polarised sources. These artefacts are typically caused by one of the following situations:

- a match between a low flux component of a multi-component source in Stokes I to leakage of a brighter component in Stokes V,
- a match between components of an extended source in Stokes I and leakage in Stokes V, indicated by the presence of multiple nearby components and mismatched component shape parameters,
- a match to a spurious noise peak in Stokes V, indicated by a combination of low signal to noise ratio of $< 6\sigma_V$ along with an offset between Stokes I and V position of $> 4''$ and source morphology resembling noise rather than a point source,
- a match between the sidelobes and leakage of a poorly deconvolved bright source.

In total we removed 837 candidates based on these criteria, with the majority caused by matches between the sidelobes of bright sources in Stokes I and their leakage in

Stokes V as shown in panels (a) and (b) of Figure 3.3, or association between leakage from the sub-components of an extended, multi-component source as shown in panel (c). We further removed 296 candidates with $|S_V|/S_I > 0.06$ caused by polarisation leakage towards the image corners, where leakage is less well suppressed than the central region of the image.

3.4.3 Classification

We classified each of the remaining 54 candidates following the same procedure detailed by Pritchard et al. (2021); using radio and multi-wavelength image cutouts, queries to the SIMBAD and NED databases, and radio lightcurves and spectral energy distributions derived from archival radio data. We identified 85 total detections of 11 known pulsars, including the Large Magellanic Cloud pulsar PSR J0523−7125 discovered by Wang et al. (2022b), and seven highly circularly polarised transients with no multi-wavelength counterpart, including the Galactic Centre transient J1736−3216 discovered by Wang et al. (2021).

We queried SIMBAD and the Gaia Data Release 3 (Gaia DR3; Gaia Collaboration et al. 2023) catalogue for stars within a $3\overset{\prime}{.}5$ radius of candidate positions. From this sample we removed sources with parallax over error $\pi/\sigma_\pi < 10$ and distance $d < 500\,\mathrm{pc}$ in order to reject false positive alignments to distant stars in high source density regions such as the Galactic plane. We then applied positional corrections to the radio epoch using Gaia proper motion parameters, identifying 36 matches to stars within the SNR dependent astrometric uncertainty determined by Equation (3.1).

Combined with the stars detected in our circular polarisation search of RACS-low we have detected a total of 76 radio stars. We quantified the rate of false-positive association between foreground stars and extragalactic radio sources by offsetting the positions of all 76 stars by 5–20$'$ in random directions and crossmatching against SIMBAD and Gaia DR3 with the same selection criteria as above. Ten runs of this procedure resulted in zero matches, suggesting a false-positive rate of less than 0.2 % and an extremely low probability that any of our detections are due to chance alignment.

3.5 Radio Properties

In our combined circular polarisation searches of RACS-low and VASTP-low we have detected 76 radio stars a total of 229 times in Stokes I and 113 times in Stokes V. The majority of detected stars are M-dwarfs (dM) or interacting RS CVn / Algol binary systems (IB), with a small number of K-dwarfs (dK), YSOs, and MCP stars, and two white dwarfs (WD). We summarise the detection counts of each variable class detected in RACS-low and VASTP-low in Table 3.3, and in Table 3.4 we list the radio properties of each star.

We detect a higher proportion of dM to IB systems in comparison to radio stars detected in FIRST by Helfand et al. (1999) and LoTSS by Callingham et al. (2023),

Table 3.3: Count summary of radio stars in RACS-low and VASTP-low. Columns indicate the abbreviated class name, number count of unique stars, total individual detections $N_d[I]$ and $N_d[V]$ in Stokes I and V respectively, and total observations N_o for each variable class of radio star.

Variable Class		Stars	$N_d[I]$	$N_d[V]$	N_o
M-dwarfs	(dM)	45	96	65	417
RS CVn / Algol binaries	(IB)	9	52	23	74
Magnetic chemically peculiar	(MCP)	7	17	7	17
Young stellar objects	(YSO)	5	34	7	48
Hot spectroscopic binaries	(HSB)	4	23	4	32
K-dwarfs	(dK)	4	5	5	16
White dwarfs	(WD)	2	2	2	14

whose samples are each approximately 50 % comprised of IB stars. This can be explained by the differences in survey strategy along with the relative timescales of dM and IB radio emission, where dM stars generally feature faint quiescent emission and radio bursts lasting seconds to hours (e.g. Villadsen & Hallinan 2019), while IB systems typically have brighter, long-duration quiescent emission (e.g. Chiuderi Drago & Klein 1990). FIRST observations are composed of 165 s snapshots co-added to an effective duration of ∼35 min while the VASTP-low survey footprint is sampled a median of 14 times in 12 min snapshots, increasing the likelihood of detecting M-dwarf bursts. Moreover, FIRST observations covered a narrow bandwidth of 42 MHz which may have limited the capability to detect coherent M-dwarf bursts with sharp spectral cutoffs, while the detectability of broadband gyrosynchrotron emission associated with IB systems is less affected by bandwidth. LoTSS images are constructed with an integration time of 8 h, and the M-dwarfs reported by Callingham et al. (2023) all feature long-duration emission spanning the full observation (Callingham et al. 2021b). Short time-scale bursts are likely to be missed in long integration images due to dilution of the burst flux with lengthy periods in which burst activity is low or absent. Alternatively, the difference in dM and IB detection counts may be explained by a change in the emission characteristics of each source class between the LoTSS frequency of 144 MHz and VASTP-low frequency of 887.5 MHz, though further analysis of the radio stars detected in each band is required to disentangle survey biases from intrinsic changes in the emission physics.

In Figure 3.4 we show the fractional circular polarisation $|S_V|/S_I$ as a function of Stokes I flux density for all star detections in RACS-low and VASTP-low. We also show detected pulsars that are well separated in this space from the majority of single star detections, having lower $|S_V|/S_I$ of ∼10–30 %. This is slightly higher than the fractional circular polarisation of pulsars detected in LoTSS by Callingham et al. (2023), who find most pulsars below the $|S_V|/S_I \sim 10\,\%$ level, however this is likely just a selection effect due to the $|S_V|/S_I \sim 6\,\%$ limit of our search. For a more complete analysis of known pulsars detected in RACS-low we refer the reader to Anumarlapudi et al. (2023), who find a mean pulsar $|S_V|/S_I$ of $\sim 5\,\%$.

Table 3.4: Table of radio stars detected in the VASTP-low and RACS-low surveys. Listed columns are stellar name, radio variable and spectral classes, radio coordinates, proper motion parameters $\mu_\alpha \cos\delta$ and μ_δ, parallax π, upper limit to emission region length scale R_e, 887.5 MHz Stokes I peak flux density S_I, fractional circular polarisation $|S_V|/S_I$, lower limit to brightness temperature $\log_{10} T_B$, radio luminosity $\log_{10} L_\nu$, and the number of Stokes I and V detections $N_d[I]$ and $N_d[V]$, and total number of observations N_o of each star over the survey. S_I, $|S_V|/S_I$, T_B, and L_ν are reported as ranges over the detections of each star.

Name	Variable Type	Spectral Class	RA	Dec	$\mu_\alpha \cos\delta$ mas/yr	μ_δ mas/yr	π mas	R_e[a] $R_\odot$	S_I mJy PSF^{-1}	$\lvert S_V\rvert/S_I$	$\log_{10} T_B$ K	$\log_{10} L_\nu$ erg s^{-1} Hz^{-1}	$N_d[I]$	$N_d[V]$	N_o
G 131-26	dM	M5V	00:08:53.88	+20:50:19.36	−48.64	−260.19	55.26 ± 0.76	1.0	2.78	0.57	10.3	15.0	1	1	1
1RXS J001650.6-071013	dM	M0	00:16:50.11	−07:10:15.19	39.84	9.74	14.01 ± 0.06	2.3	0.85–3.07	0.19–1.00	10.3–10.9	15.7–16.3	8	4	11
CF Tuc	IB	G2/5V+F0	00:53:09.12	−74:39:05.75	243.13	21.62	11.37 ± 0.03	11.3	1.31–10.98	0.06–0.62	9.3–10.2	16.1–17.0	10	1	10
CS Cet	dK	K0IV(e)	01:06:48.93	−22:51:23.22	−38.15	−81.19	10.50 ± 0.06	12.3	6.32–7.30	0.37–0.39	10.0–10.1	16.8–16.9	2	2	2
BI Cet	IB	G5V	01:22:50.09	+00:42:39.60	−114.59	−238.95	15.98 ± 0.05	4.8	1.20–3.45	0.21–0.99	9.7–10.2	15.8–16.2	7	2	9
RX J0143.7-0602	dM	M3.5	01:43:45.14	−06:02:40.27	52.26	−27.07	46.85 ± 0.07	1.2	2.89	0.56	10.4	15.2	1	1	13
WISEA J014358.01-014930.3	dM		01:43:58.02	−01:49:28.73	60.35	3.77	24.80 ± 0.02	1.0	1.44	0.84	10.7	15.4	1	1	12
SDSS J020648.78-061416.3	IB		02:06:48.76	−06:14:16.30	6.13	−24.34	2.25 ± 0.04	4.8	1.64	0.96	11.6	17.6	1	1	21
UPM J0250-0559	dM		02:50:40.29	−05:59:50.89	67.31	10.17	33.20 ± 0.96	1.2	2.25	0.82	10.6	15.4	1	1	24
LP 771-50	dM	M5e	02:56:27.19	−16:27:38.53	212.29	−55.25	32.56 ± 0.41	0.6	1.65	1.00	11.1	15.3	1	1	1
CD-44 1173	dM	K6Ve	03:31:55.73	−43:59:14.91	88.47	−3.50	22.17 ± 0.03	2.5	3.87	0.88	10.5	16.0	1	1	19
HD 22468	IB	K2:Vnk	03:36:47.19	+00:35:13.52	−32.89	−161.77	33.75 ± 0.09	9.1	6.92–78.17	0.03–0.54	9.3–10.3	15.9–16.9	13	13	13
RX J0348.9+0110	dK	K3V:/E	03:48:58.83	+01:10:54.83	29.73	−22.72	9.11 ± 0.33	0.9	1.42	0.93	11.8	16.3	1	1	12
HD 24681	YSO	G5V	03:55:20.61	−01:43:46.58	43.33	−91.49	17.82 ± 0.04	2.6	1.88	0.54	10.3	15.9	1	1	13
HD 24916B	dM	M2.5V	03:57:28.66	−01:09:27.07	−209.41	−139.73	65.49 ± 0.04	1.3	1.02	0.91	9.5	14.5	1	1	13
UPM J0409-4435	dM		04:09:32.15	−44:35:38.19	−16.86	115.59	68.07 ± 0.04	0.7	1.27–2.42	0.73–1.00	10.2–10.4	14.5–14.8	3	1	23
RX J0419.2-7120	dM		04:19:13.35	−71:21:12.05	−52.92	−46.71	18.77 ± 0.13	1.1	1.45	0.58	10.9	15.7	1	1	1
HD 283750	dK	K2.5Ve	04:36:48.60	+27:07:55.01	232.87	−148.14	57.10 ± 0.06	2.0	3.94	0.76	9.9	15.2	1	1	1
CD-56 1032	dM	M3Ve+M4Ve	04:53:31.02	−55:51:35.10	126.12	76.86	90.12 ± 0.03	1.3	0.96–12.38	0.16–0.98	9.3–10.4	14.1–15.3	14	2	23
HD 32595	HSB	B8	05:04:49.06	+13:18:32.86	1.83	−5.18	3.40 ± 0.28	6.5	3.36	0.62	11.2	17.5	1	1	1
V1154 Tau	IB	B5	05:05:37.70	+23:03:41.59	0.27	−6.89	3.59 ± 0.46	8.9	2.07	0.64	10.7	17.3	1	1	1
AB Dor	YSO	K0V	05:28:44.98	−65:26:51.35	29.15	164.42	65.32 ± 0.14	4.5	1.83–7.73	0.16–1.00	8.7–9.4	14.7–15.3	29	2	31
HD 36150	MCP	A5III/IV	05:29:41.78	−00:48:07.66	71.34	−47.04	8.93 ± 0.18	8.9	1.99	1.00	9.9	16.5	1	1	1
SCR J0533-4257	dM	M4.5	05:33:28.01	−42:57:18.93	−17.58	39.51	96.63 ± 0.34	1.4	0.85–6.32	0.57–1.00	9.1–10.0	14.0–14.9	7	4	12
[W60] D43	dM	M	05:35:36.96	−67:05:23.00					1.41	0.74			1	1	10
Ross 614	dM	M4.5V	06:29:24.31	−02:49:03.32	750.14	−802.95	242.97 ± 0.88	0.8	2.75–3.84	0.39–0.55	9.3–9.5	13.7–13.9	2	2	2
Gaia DR3 2930889294867085440	WD		07:15:31.16	−19:39:53.82	−6.06	16.22	5.52 ± 0.21	0.03	12.39	0.43	16.0	17.7	1	1	1
alf Gem	HSB	A1V+A2Vm	07:34:35.49	+31:53:14.63			64.12 ± 3.75	6.8	1.35	0.78	8.3	14.6	1	1	1
k02 Pup	MCP	B5IV	07:38:49.74	−26:48:12.84	−17.54	21.36	8.81 ± 0.20	5.3	2.93	0.76	10.5	16.7	1	1	1
YZ CMi	dM	M4.0Ve	07:44:39.66	+03:33:01.74	−348.10	−445.88	167.02 ± 0.06	1.1	2.66	1.00	9.3	14.1	1	1	1
HD 67951	MCP	ApSiCr	08:08:23.62	−45:47:43.16	−4.29	9.96	2.65 ± 0.04	1.8	3.13	0.40	12.6	17.7	1	1	1
G 41-14	dM	M3.5V	08:58:56.75	+08:28:19.76			147.66 ± 1.98	0.8	19.19	0.89	10.6	15.0	1	1	1
HD 77653	MCP	ApSi	09:01:44.44	−52:11:19.82			8.85 ± 0.42	4.7	7.06	0.67	11.0	17.0	1	1	1
WT 2458	dM	M4.5	09:45:57.98	−32:53:26.40	−300.41	146.02	83.23 ± 0.09	0.7	1.54	0.83	10.1	14.4	1	1	1
PM J09551-0819	dM	M1e	09:55:09.49	−08:19:23.93	−135.78	−7.16	31.49 ± 0.04	0.8	1.81	0.84	10.9	15.3	1	1	25
LP 610-59	dM		10:43:37.55	−00:48:09.06	−184.94	14.43	19.53 ± 0.15	0.6	2.05	0.76	11.6	15.8	1	1	24
WISEA J105315.25-085941.5	dM		10:53:15.20	−08:59:42.22	30.96	−0.67	29.38 ± 0.06	1.0	1.07–3.43	0.59–0.95	10.5–11.0	15.2–15.7	3	1	11
ksi UMa	IB	F8.5:V+G2V	11:18:10.18	+31:31:31.12	−339.40	−607.89	114.49 ± 0.43	11.3	1.49	0.68	7.4	14.1	1	1	1
WISEA J114020.71-330519.4	dM		11:40:20.68	−33:05:19.22	−62.94	−29.30	12.94 ± 0.08	0.9	2.54	0.63	11.7	16.3	1	1	1

Table 3.5: Table 3.4 continued.

Name	Variable Type	Spectral Class	RA	Dec	$\mu_\alpha \cos\delta$ mas/yr	μ_δ mas/yr	π mas	R_e[a] $R_\odot$	S_I mJy PSF^{-1}	$\lvert S_V \rvert / S_I$	$\log_{10} T_B$ K	$\log_{10} L_\nu$ erg s^{-1} Hz^{-1}	$N_d[I]$	$N_d[V]$	N_o
PM J11422-0122	dM	M5e	11:42:12.84	−01:22:05.61	−98.06	−4.86	54.07 ± 0.66	0.3	2.31	0.41	11.3	15.0	1	1	14
HD 105382	MCP	B5V	12:08:05.06	−50:39:40.79	−34.35	−11.51	9.85 ± 0.32	5.0	2.28	0.59	10.4	16.4	1	1	1
WISEA J122501.45-521614.6	dM		12:25:01.37	−52:16:14.58	−30.86	−11.29	8.14 ± 0.30	0.4	3.40	0.86	13.0	16.8	1	1	1
WISEA J123623.17-074508.2	dM		12:36:23.03	−07:45:06.81	−83.14	−34.91	25.17 ± 0.06	0.7	2.28	0.60	11.2	15.6	1	1	10
UCAC4 129-071513	YSO		12:52:22.67	−64:18:38.92	−38.42	−14.69	9.70 ± 0.06	2.0	1.38–3.36	0.84–1.00	11.0–11.4	16.2–16.6	2	2	2
HD 115247	HSB	F5V	13:16:02.96	−05:40:07.91	−83.66	−40.39	8.41 ± 0.06	10.4	2.23–9.87	0.06–0.53	9.9–10.5	16.6–17.2	20	1	21
BH CVn	IB	A6m	13:34:47.90	+37:10:56.77	85.61	−9.71	21.67 ± 0.16	9.8	6.64–7.16	0.35–0.37	9.6–9.6	16.2–16.3	2	2	2
V851 Cen	IB	K0III	13:44:00.95	−61:21:58.92	21.07	13.80	13.50 ± 0.04	10.6	7.68	0.69	10.0	16.7	1	1	1
CU Vir	MCP	ApSi	14:12:15.72	+02:24:34.21	−43.05	−26.08	13.94 ± 0.26	6.3	2.17–13.83	0.16–0.64	9.9–10.7	16.1–16.9	11	1	11
HD 124498	dK	K5.5Vkee	14:14:21.74	−15:21:17.96	−128.33	−164.99	34.53 ± 0.18	2.3	2.17	0.62	10.0	15.3	1	1	1
WISEA J141443.13+261639.7	dM		14:14:43.16	+26:16:40.45	55.60	−3.50	21.26 ± 0.06	0.8	2.65–3.08	0.62–0.72	11.3–11.4	15.8–15.9	2	2	2
G 165-61	dM	M4.5Ve	14:17:02.04	+31:42:44.31			60.00 ± 2.20	0.6	2.02	0.96	10.6	14.8	1	1	1
G 124-43	dM	M4.65	14:27:55.67	−00:22:26.29	−361.50	41.64	57.08 ± 0.06	1.0	1.30–2.97	0.40–1.00	10.0–10.4	14.7–15.0	9	5	22
LP 325-68	dM	M4.5Ve	14:37:18.08	+26:53:00.87	−227.64	84.35	27.29 ± 0.06	0.8	3.01	0.55	11.2	15.7	1	1	1
HD 142184	MCP	B2V	15:53:55.82	−23:58:41.33	−13.47	−23.97	7.08 ± 0.14	11.7	7.84	0.22	10.5	17.3	1	1	1
GSS 35	YSO	B3	16:26:34.11	−24:23:28.17	−2.17	−23.56	8.17 ± 0.11	2.5	8.18	0.23	11.7	17.2	1	1	1
EMSR 20	YSO	G7	16:28:32.50	−24:22:45.81	−9.47	−28.06	7.35 ± 0.06	2.4	2.24	0.72	11.3	16.7	1	1	1
CD-38 11343	dM	M3Ve+M4Ve	16:56:48.49	−39:05:38.96	47.00	−113.26	63.63 ± 0.08	1.3	7.29	0.29	10.4	15.3	1	1	1
PM J17021-2740	dM		17:02:07.97	−27:40:28.71	−129.85	−220.40	41.86 ± 0.09	0.9	3.99	0.68	10.9	15.4	1	1	1
Ross 867	dM	M4.5V	17:19:52.68	+26:30:09.94	−226.13	355.28	92.97 ± 0.06	0.9	3.79	0.67	10.2	14.7	1	1	1
G 183-10	dM	M3.5Ve	17:53:00.25	+16:54:59.05	−243.94	−240.05	44.15 ± 1.02	0.8	2.09	0.51	10.6	15.1	1	1	1
2MASS J18040683-1211342	dM		18:04:06.89	−12:11:35.71	−28.06	−6.91	18.52 ± 0.04	0.9	2.71	0.64	11.4	16.0	1	1	1
UCAC3 152-281176	dM	M5	18:45:00.95	−14:09:04.59	47.60	−85.72	54.97 ± 0.09	0.9	5.73	0.79	10.8	15.4	1	1	2
SCR J1928-3634	dM		19:28:33.74	−36:34:39.21	95.72	−453.66	39.55 ± 0.06	0.7	2.51	0.64	10.9	15.3	1	1	1
2MASS J19551247+0045365	WD		19:55:12.45	+00:45:36.33	−2.55	−29.55	5.85 ± 0.08	0.07	2.19	0.69	14.6	16.9	1	1	13
bet Aql B	dM	M3	19:55:18.83	+06:24:28.14	22.62	−472.30	73.61 ± 0.05	1.2	2.85	0.74	9.9	14.8	1	1	1
SCR J2009-0113	dM	M5.0V	20:09:18.16	−01:13:45.36	−43.63	−373.73	92.52 ± 0.12	0.6	1.86–10.30	0.73–0.92	10.3–11.0	14.4–15.2	5	5	12
LEHPM 2-783	dM	M6	20:19:49.81	−58:16:49.89	−24.64	−340.82	61.18 ± 0.10	1.0	2.43	0.81	10.2	14.9	1	1	12
2MASS J20390476-4117390	dM		20:39:04.97	−41:17:38.95	58.05	−47.38	25.63 ± 0.06	0.7	1.67	0.99	11.1	15.5	1	1	12
Ross 776	dM	M3.3V	21:16:06.14	+29:51:52.37	204.61	24.16	49.21 ± 0.24	1.3	6.44	0.50	10.6	15.5	1	1	1
UCAC3 89-412162	dM		21:22:17.56	−45:46:31.42	−53.47	−34.00	31.55 ± 0.04	0.8	2.31	0.87	11.0	15.4	1	1	12
HD 210547A	HSB		22:13:00.08	−61:58:53.05	−13.18	0.79	5.82 ± 0.03	5.7	1.44	0.94	10.5	16.7	1	1	9
Wolf 1561 A	dM	M4V	22:17:18.29	−08:48:18.13	−458.51	−291.85	89.80 ± 0.09	0.7	1.74–1.85	0.69–1.00	10.0–10.1	14.4–14.4	2	1	14
LAMOST J221747.87-030039.0	dM	M5	22:17:47.86	−03:00:38.82	21.79	−9.96	6.71 ± 0.08	1.3	5.50	0.77	12.2	17.2	1	1	36
UPM J2224-5826	dM		22:24:24.51	−58:26:14.13	−75.71	−37.18	62.38 ± 0.19	1.5	4.12–5.45	0.85–1.00	10.1–10.2	15.1–15.2	2	1	20
SCR J2241-6119A	dM		22:41:44.76	−61:19:33.18	150.23	−87.90	35.19 ± 0.05	0.9	1.38–5.44	0.39–1.00	10.6–11.2	15.1–15.7	6	4	9
SZ Psc	IB	G5Vp	23:13:23.70	+02:40:33.01	27.03	27.33	11.10 ± 0.08	13.7	2.07–11.89	0.03–0.84	9.4–10.1	16.3–17.1	16	1	16

[a] R_e taken as: $3R_\star$ for single stars as calculated from Gaia DR3 photometry (Gaia Collaboration et al. 2023) and the inter-binary region for interacting binaries.

In Figure 3.5 we show the Stokes I radio luminosity distribution of our sample, with M-dwarfs tending to group around $L_\nu = 10^{15}\,\mathrm{erg\,s^{-1}\,Hz^{-1}}$ while other variable types group around $L_\nu = 10^{16}$–$10^{17}\,\mathrm{erg\,s^{-1}\,Hz^{-1}}$. Radio luminosity is also shown as a function of stellar distance in Figure 3.6. The hatched region represents flux densities below our 5σ detection threshold of $1.25\,\mathrm{mJy\,PSF^{-1}}$ in Stokes I, which preferentially suppresses counts at the low end of the L_ν distribution. The completeness of our sample is further dependent upon fractional circular polarisation, with lower $|S_V|/S_I$ shifting the detection threshold to higher L_ν, indicated by the dashed line at $|S_V|/S_I = 0.5$.

To place constraints on plausible radio emission mechanisms we calculated the brightness temperature

$$T_B = \frac{Sc^2}{2\pi k_B \nu^2} \frac{d^2}{R_e^2} \tag{3.2}$$

where k_B is the Boltzmann constant, ν is the observing frequency of 887.5 MHz, d is the stellar distance, and R_e is the length scale of the emission region. We have assumed an upper limit of $R_e = 3R_\star$ for each star, and additionally calculate T_B for interacting binaries with R_e equal to three times the binary separation distance. The true emission region is likely much smaller than these limits, particularly for detections with large $|S_V|/S_I$ as they require a consistent orientation of the magnetic field within the emission region to produce predominantly right or left handed circular polarisation.

In Figure 3.7 we show all star detections in a brightness temperature–fractional circular polarisation phase space alongside empirical models of the maximum effective temperature of optically thin gyrosynchrotron emission (Dulk 1985). Most interacting binary systems feature minimum T_B of 10^6–10^{10} K and $|S_V|/S_I < 0.8$ and are plausibly driven by gyrosynchrotron emission which is commonly detected from RS CVn systems, though we note that coherent emission from the ECMI is also possible (e.g. Slee et al. 2008; Toet et al. 2021). The majority of other detections including one RS CVn, however, feature minimum T_B of order 10^{10}–10^{16} K, and as these detections feature high fractional circular polarisation the emission necessarily originates from a compact region in which the magnetic field is nearly uniform. This constraint on the size of the emission region further increases the minimum brightness temperature, and combined with the large fractional circular polarisation makes gyrosynchrotron emission unlikely. These detections are therefore likely driven by a coherent emission process such as the ECMI or plasma emission.

3.6 Population Statistics

3.6.1 Detection Counts

We detected a total of 36 stars within the VASTP-low footprint over 15 epochs. Due to slight variations in the survey footprint between epochs and overlap between neighbouring tiles, each star was observed between 9–36 times with a median of 14

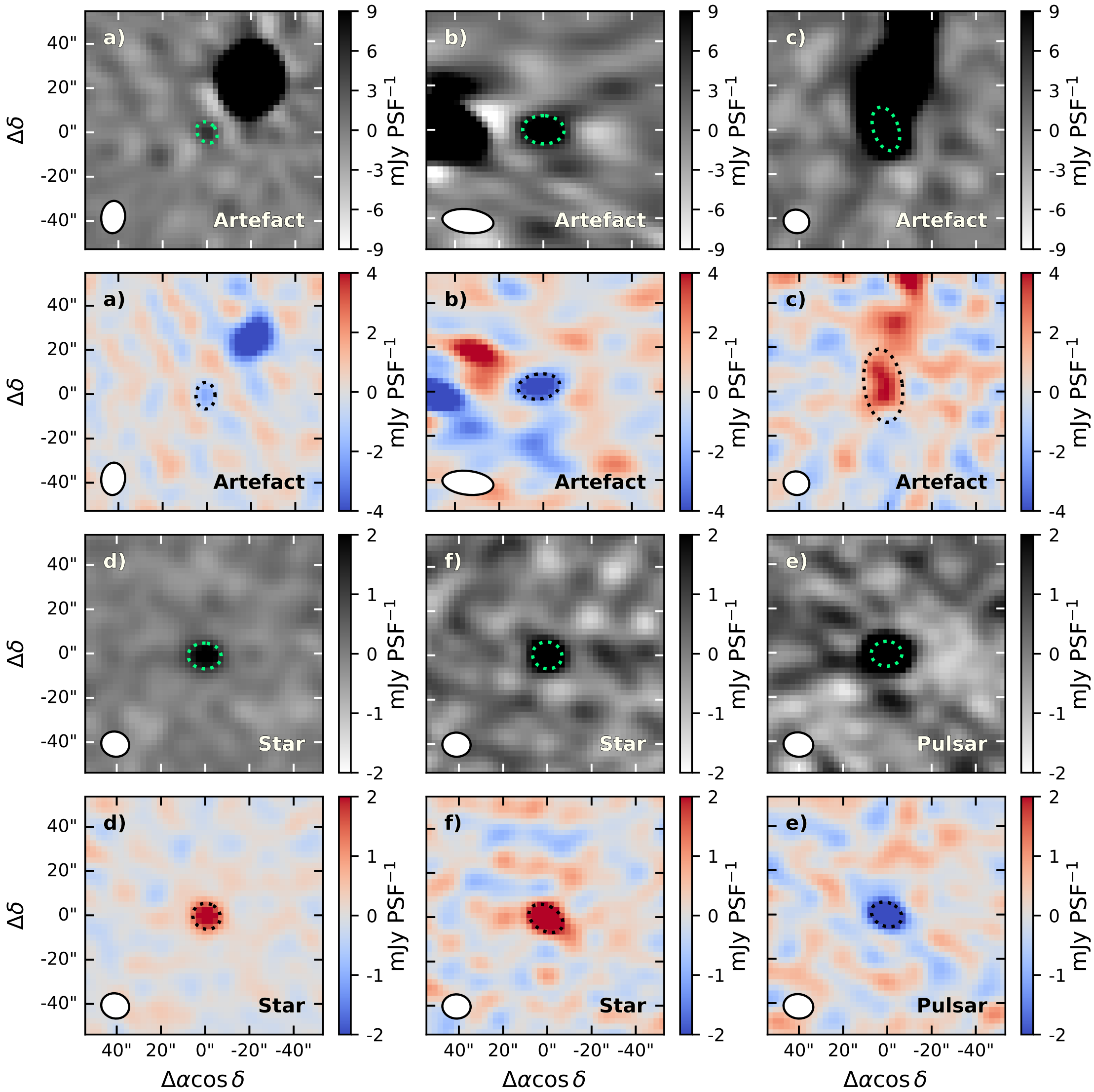

Figure 3.3: Stokes I (top panel) and V (bottom panel) cutouts of six candidates inspected during classification. The top pair of rows shows candidates rejected due to I-V association between either the sidelobes of a bright source (panels a) and b)) or leakage from a multi-component extended source (panel c)). The bottom pair of rows show two identified stars (panels d) and e)) and a pulsar (panel f)) for comparison. The restoring beam is shown as the ellipse in the lower left of each panel, and green and black dotted ellipses trace the shape of the Stokes I and V SELAVY components in each association respectively.

observations. To characterise the repeat detection rates of each star we calculate the detection fraction $DF = N_d/N_o$ where N_o and N_d are the respective number of observations and detections of each star. These counts only consider observations in which the local 3-sigma RMS noise is less than the flux density of the weakest detection, removing observations in which the star is located toward the image edges or corners where sensitivity degrades.

In Figure 3.8 we show the detection fraction as a function of fractional polarisation.

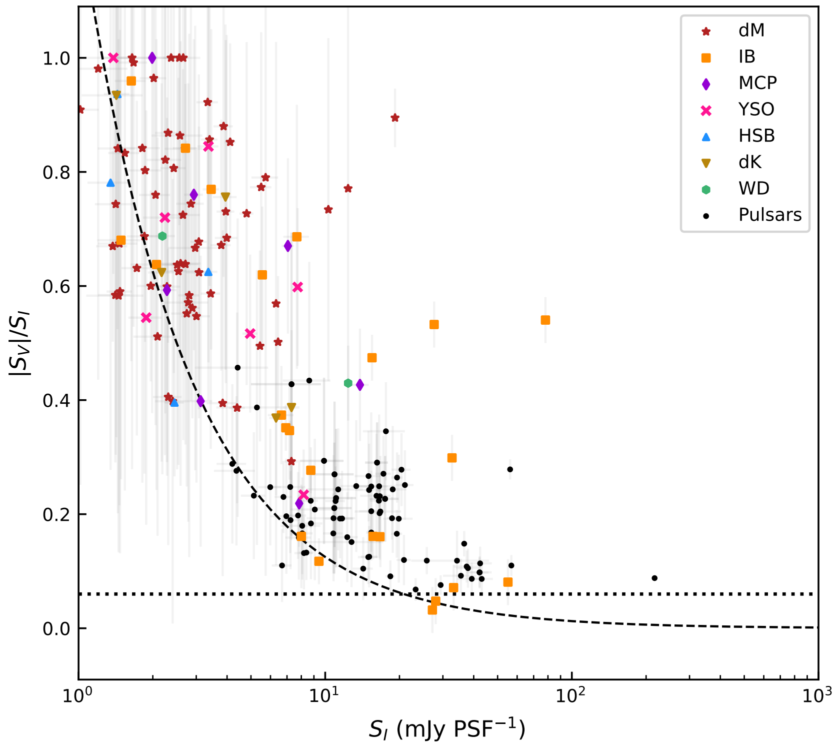

Figure 3.4: Fractional circular polarisation and flux density phase space, with the radio stars in our sample labelled according to variable class. M-dwarfs (dM) are shown as red stars, K-dwarfs (dK) as brown stars, interacting binaries (IB) as yellow squares, magnetic chemically peculiar (MCP) stars as purple diamonds, young stellar objects (YSO) as fuchsia crosses, hot spectroscopic binaries (HSB) as blue triangles, and white dwarfs (WD) as green hexagons. The dotted line indicates a fractional circular polarisation of 6 % below which we excluded candidates from initial classification, retaining only the low $|S_V|/S_I$ detections of previously classified sources. The dashed line indicates a $5\sigma_V$ detection threshold where $\sigma_V = 0.25\,\mathrm{mJy\,PSF^{-1}}$ is the median RMS noise in Stokes V, and represents the average sensitivity limit in fractional polarisation across our survey. Local variations in RMS result in a few detections below this threshold.

Most of the stars with high DF are interacting binaries that feature a quiescent component to the radio emission, along with one YSO (AB Dor) and one MCP star (CU Vir) that are both well-known, persistent radio emitters. We find the majority of highly circularly polarised detections are associated with single detections of M-dwarfs with a median DF of 8.5 %, and take this as an upper limit on the average population detection fraction $\langle DF \rangle$. This upper limit is consistent with previous estimates of the duty cycle of both stochastic radio bursts (Villadsen & Hallinan 2019) and rotationally modulated auroral emission (Hallinan et al. 2007; Nichols et al. 2012).

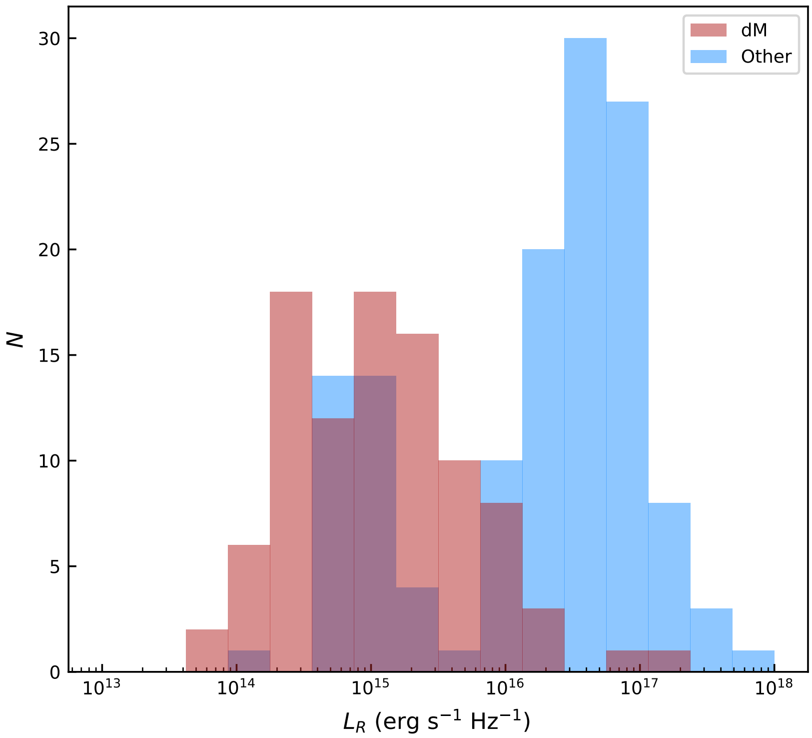

Figure 3.5: Stokes I radio luminosity distribution of all star detections in RACS-low and VASTP-low. M-dwarfs are shown in red and all other stars are combined and shown in blue, as the sample sizes of individual variable and spectral classes are too low to meaningfully show them separately.

3.6.2 Radio Activity Fraction of the M-Dwarf Population

As we detect new stars in each successive analysed epoch, an upper limit to the detection fraction implies the existence of low burst-rate stars within the population that produce detectable radio bursts but have not been sufficiently sampled to produce a detection. We define a burst to be detectable if it has a radio luminosity sufficient to be detected above our 5σ detection threshold of $1.25\,\mathrm{mJy\,PSF^{-1}}$, which corresponds to a detectability horizon d_{max} for a particular burst radio luminosity. In this section we use the repeat detection rates of stars within the VASTP-low footprint to estimate the size of the detectable population. We limit our analysis to M-dwarfs due to the low sample size of other variable and spectral classes. We further restrict our sample to $d_{\mathrm{max}} < 25\,\mathrm{pc}$ within which bursts above the typical M-dwarf radio luminosity of $10^{15}\,\mathrm{erg\,s^{-1}\,Hz^{-1}}$ are detectable, as our sample becomes increasingly incomplete in radio luminosity at greater distances.

We assume there are n detectable M-dwarfs per unit solid angle, each with a burst rate λ sampled from the population distribution $f(\lambda)$ such that $nAf(\lambda)\,\mathrm{d}\lambda$ is the number of detectable M-dwarfs with burst rates between λ and $\lambda + \mathrm{d}\lambda$ in a solid angle A. For a star with rate λ the number of detectable bursts in an epoch of duration Δt is $\lambda\Delta t$. Hence the expected number of bursts detected in the epoch from all stars in a solid angle A is

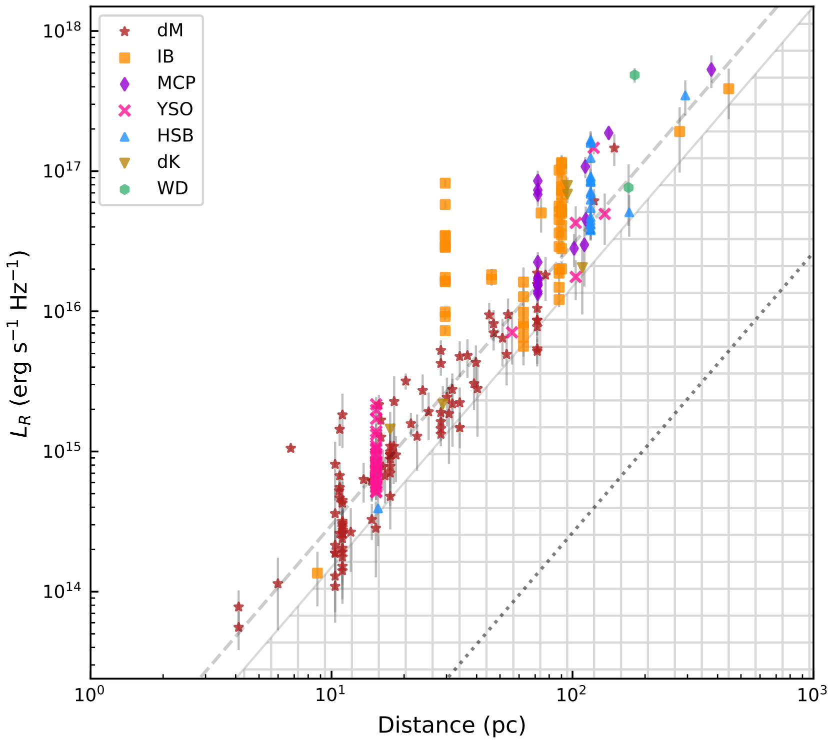

Figure 3.6: Stokes I radio luminosity of each star detection as a function of distance. The hatched region corresponds to Stokes I flux densities below the 5σ detection threshold of 1.25 mJy PSF^{-1}. The dashed line indicates the 5σ Stokes V detection threshold for $|S_V|/S_I = 0.5$, with lower $|S_V|/S_I$ shifting the threshold to higher L_ν. The dotted line represents the projected 5σ detection threshold of 22 µJy PSF^{-1} in a 1 h observation with SKA-mid (Braun et al. 2019). Repeat detections are visible as vertically aligned points.

$$N_d = \int_0^\infty nA\lambda\Delta t f(\lambda)\,\mathrm{d}\lambda \tag{3.3}$$
$$= nA\Delta t\langle\lambda\rangle \tag{3.4}$$

where $\langle\lambda\rangle = \int_0^\infty \lambda f(\lambda)\,\mathrm{d}\lambda$ is the average burst rate over the observed stars. The expected number of bursts in M epochs is then

$$\sum_{i=1}^{M} N_{d,i} = n\langle\lambda\rangle \sum_{i=1}^{M} A_i\Delta t_i \tag{3.5}$$

where A_i and Δt_i are the solid angle coverage and observation duration of epoch i.

None of our detections show evidence of bursts on timescales shorter than the observation time so we assume each detection represents a single burst, and as our RACS-low detections are all bright enough to be detected in a 12 min observation

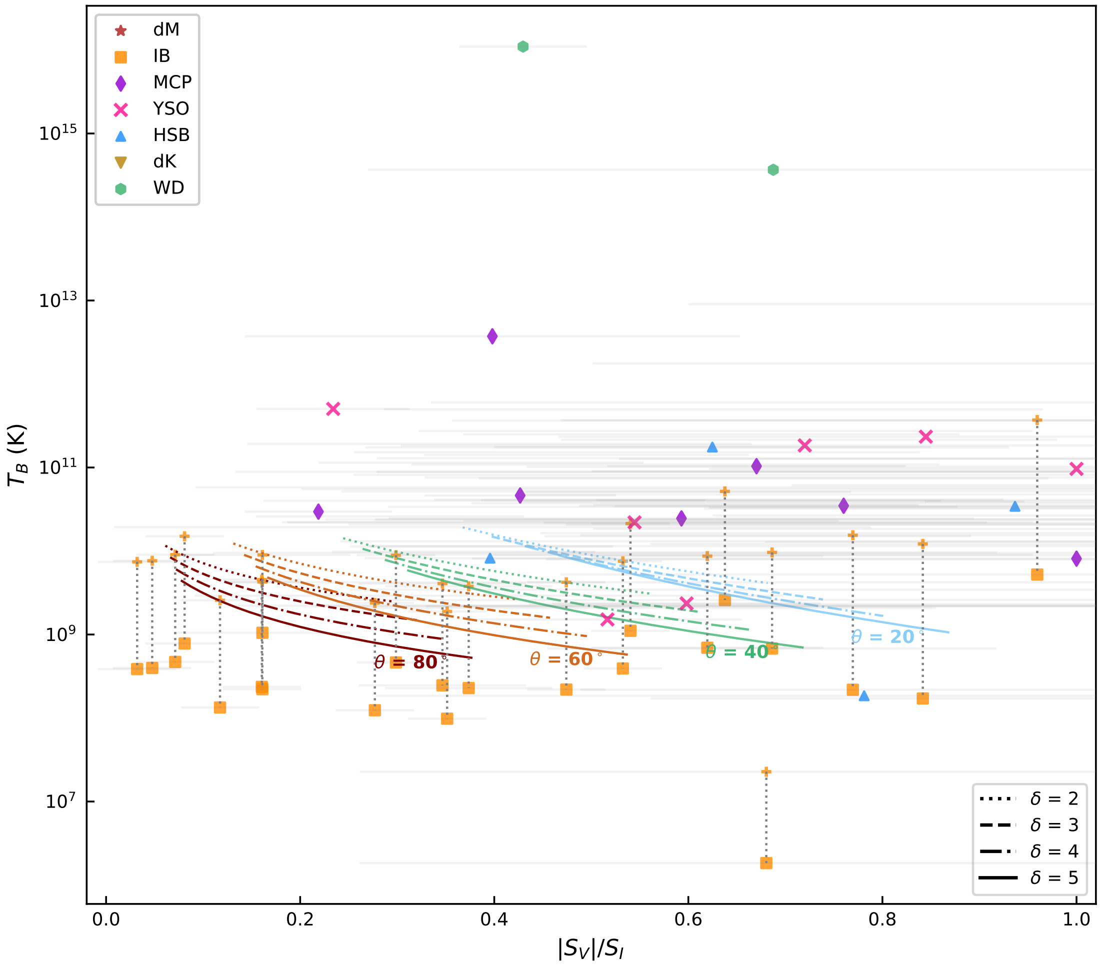

Figure 3.7: Brightness temperature and fractional circular polarisation phase space, with stars labelled according to variable class (see Figure 3.4). Vertical dotted lines connect two T_B estimates for interacting binary systems, with estimated emission regions of the inter-binary region and stellar disk represented as yellow squares and crosses respectively. Empirical models of the maximum effective temperature of optically thin gyro-synchrotron emission (Dulk 1985) are shown for a range of electron energy index δ and viewing angle θ.

we adopt a common $\Delta t = 12\,\text{min}$ for all epochs. The average detection fraction $\langle DF \rangle$ is then an estimate of the average burst rate:

$$\langle \lambda \rangle = \frac{\langle DF \rangle}{\Delta t}, \tag{3.6}$$

and the total number of detectable M-dwarfs in the VASTP-low footprint of area $A_S = 5131\,\text{deg}^2$ is then, using Equations (3.5) and (3.6):

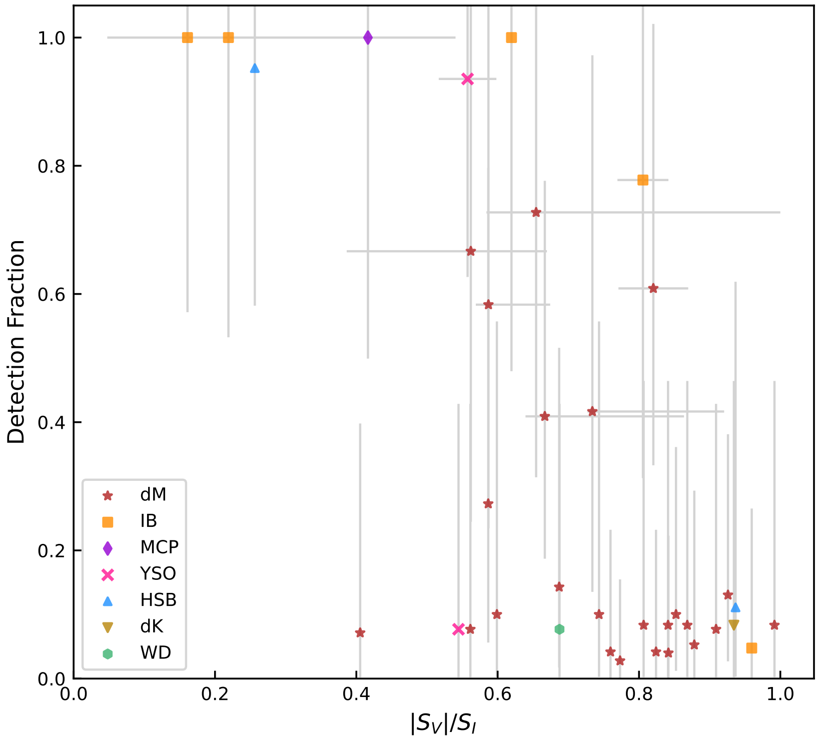

Figure 3.8: Detection fraction as a function of fractional circular polarisation for our sample of repeat observed stars in the VASTP-low footprint. The $|S_V|/S_I$ error bars indicate the range of observed fractional circular polarisation for each star, and the detection fraction error bars are derived from 95 % Poisson confidence intervals on the number of detections. Markers denote the sub-type of variable star (see Figure 3.4).

$$\mathcal{N} = nA_S = \frac{A_S}{\sum_{i=1}^{M} A_i} \frac{1}{\langle DF \rangle} \sum_{i=1}^{M} N_{d,i}. \tag{3.7}$$

Within 25 pc we detect 11 M-dwarfs a total of 46 times. Using the solid angle coverage of each epoch listed in Table 3.2 with Equation (3.7) we estimate at least $\mathcal{N} = 47^{+16}_{-13}$ M-dwarfs within the VASTP-low footprint should produce detectable radio bursts, where the uncertainties are derived from a 95 % Poisson confidence interval on the detection counts. We compare this to the total number of M-dwarfs in this volume from the Fifth Catalogue of Nearby Stars (CNS5; Golovin et al. 2023). This catalogue is statistically complete out to 25 pc for spectral types earlier than L8 and contains 471 M-dwarfs within the VASTP-low footprint. Our analysis therefore indicates that at least 10 ± 3 % of M-dwarfs should produce radio bursts more luminous than $10^{15}\,\mathrm{erg\,s^{-1}\,Hz^{-1}}$. Given the footprint area of $5131\,\mathrm{deg}^2$ this estimate corresponds to a surface density of $n = 9^{+11}_{-7} \times 10^{-3}\ \mathrm{deg}^{-2}$, such that at least one M-dwarf within 25 pc should be detectable per $66\,\mathrm{deg}^2$ low-band field.

These results are derived for our sample within 25 pc, while including the more dis-

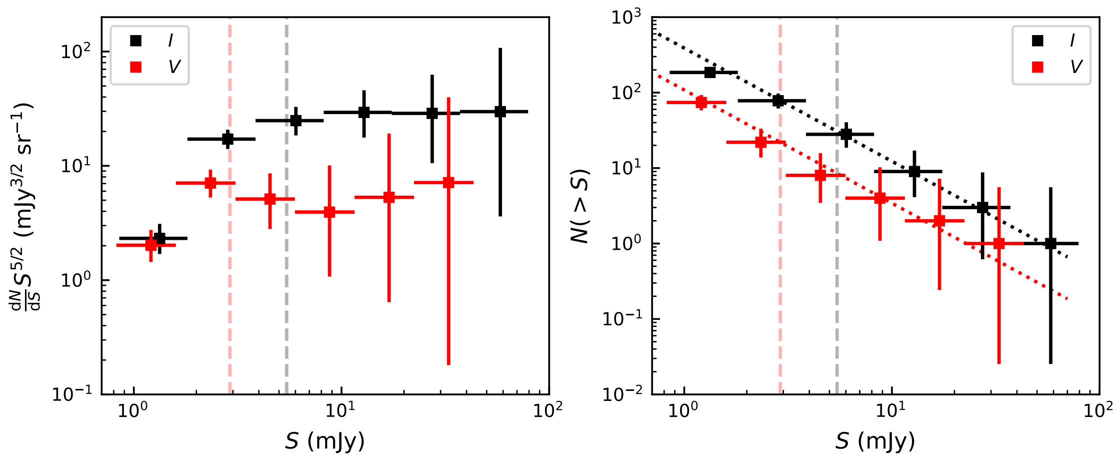

Figure 3.9: Differential (left) and cumulative (right) source counts for all star detections in RACS-low and VASTP-low, with Stokes I and V shown in black and red respectively. The red dashed line represents the RACS-low 95 % completeness limit (Hale et al. 2021) which we take as an estimate of the Stokes V completeness limit in our survey, and the black dashed line is the corresponding Stokes I completeness limit for a median fractional polarisation of 50 %. Differential counts are multiplied by a $S^{5/2}$ Euclidean normalisation, and the cumulative counts are shown alongside dotted lines representing a Euclidean source distribution with power law slope of $N(>S) \propto S^{-3/2}$.

tant high luminosity bursts we detect twice as many events. Due to incompleteness in the luminosity distribution below $10^{15}\,\mathrm{erg\,s^{-1}\,Hz^{-1}}$ and the DF distribution below $DF \sim 0.07$, these values should be interpreted as lower limits. Extending this analysis to future epochs in the full VAST survey will push the DF incompleteness to lower thresholds and allow sampling of stars with lower burst rates, probing the true turnover in the burst rate distribution and providing a more accurate estimate of the surface density and activity fraction of radio loud M-dwarfs.

3.6.3 Instantaneous Surface Density

In Figure 3.9 we show the differential and cumulative source counts for all star detections in our sample in Stokes I and V, with detections combined into six logarithmically spaced flux density bins between 1–60 mJy. Counts in both polarisations are reduced at low flux densities due to incompleteness. RACS-low sources in Stokes I have a 95 % completeness limit of 2.9 mJy (Hale et al. 2021) which we take as an estimate of the 95 % Stokes V completeness limit, indicated by the dashed red line.[1] The completeness limit in Stokes I varies due to the range of fractional polarisation in our sample, so we show the limit for the median $|S_V|/S_I$ of 50 % as the black dashed line. Above these thresholds the source counts are in agreement with a Euclidean source distribution, with flat slope in the normalised differential counts and

[1]The Stokes V RMS noise is slightly lower than in Stokes I, particularly towards poorly deconvolved bright sources or highly confused regions with diffuse Galactic emission, and the true Stokes V completeness limit is therefore lower than this estimate.

cumulative counts $N(>S) \propto S^{-3/2}$. This is consistent with expectations as our sample is contained within ∼500 pc and therefore any directional bias in counts due to Galactic plane structure is minimal (West et al. 2008).

Between RACS-low and VASTP-low our circular polarisation search has covered a total area of 135 498 deg^2 and resulted in 229 radio star detections, 96 of which are of M-dwarfs with the majority of detections attributable to coherent radio bursts. This corresponds to an instantaneous radio star detection surface density of $1.7 \pm 0.2 \times 10^{-3}$ deg^{-2} on 12 min timescales, and $7.1^{+1.6}_{-1.4} \times 10^{-4}$ deg^{-2} considering only M-dwarf detections. The full VAST survey with ASKAP will run with similar observing parameters to VASTP-low with a plan to conduct 5953 12 min observations annually, and should therefore detect $\sim 200 \pm 50$ radio stars including $\sim 130 \pm 40$ M-dwarfs each year. Scaling our measured surface densities to the expected SKA-mid 770 MHz 1-hour sensitivity of 4.4 µJy PSF^{-1} (Braun et al. 2019) and accounting for the factor of five increase in integration time, we expect a radio and M-dwarf surface density of 1.2 ± 0.3 deg^{-2} and 0.7 ± 0.2 deg^{-2} respectively. All-sky surveys with SKA-mid should therefore expect to detect $41\,000^{+10\,000}_{-9\,000}$ radio stars, with a 10^{15} erg s^{-1} Hz^{-1} completeness horizon of ∼200 pc and 10^{17} erg s^{-1} Hz^{-1} bursts detectable out to ∼2 kpc.

3.7 Conclusions And Outlook

As part of the ASKAP pilot survey program we have conducted a multi-epoch circular polarisation search for radio stars. Between RACS-low and VASTP-low we have made 229 detections of a sample of 76 stars, with the majority of detections attributed to coherent M-dwarf radio bursts. Through repeat observations of the VASTP-low survey footprint we constrain the typical duty cycle of radio bursts in the M-dwarf population to less than 8 %, and find that at least 10±3 % of the population should produce bursts with a radio luminosity greater than 10^{15} erg s^{-1} Hz^{-1}.

Circular polarisation searches have been well demonstrated as a discovery tool for radio stars, and full ASKAP surveys will produce hundreds of new radio star detections per year helping to build larger statistical samples. The full VAST survey is underway, and with further repeat sampling we will be able to better characterise the rate and luminosity distributions of M-dwarf radio bursts and extend this analysis to other radio star classes. Repeat detections will provide insight into the range of burst parameters in individual stars and their relationship with other stellar activity parameters, such as rapid rotation, chromospheric activity, and multi-wavelength transient behaviour.

These surveys will also provide a large number of candidates for targeted followup with wide-bandwidth, high instantaneous sensitivity instruments such as the Australia Telescope Compact Array (ATCA) and MeerKAT, allowing the phenomenology of their activity to be further characterised with dynamic spectroscopy and polarimetry. Identification of the emission processes responsible for coherent stellar radio bursts will provide important insights into the magnetospheric processes present in these systems, helping to distinguish whether they more resemble the stochastic radio activity observed from the Sun, rotationally modulated pulses driven by auroral current systems, or other magnetospheric processes unobserved in the Solar system.

Acknowledgements

JP is supported by Australian Government Research Training Program Scholarships. DK and AO are supported by NSF grant AST-1816492. This scientific work uses data obtained from Inyarrimanha Ilgari Bundara / the Murchison Radio-astronomy Observatory. We acknowledge the Wajarri Yamaji People as the Traditional Owners and native title holders of the Observatory site. CSIRO's ASKAP radio telescope is part of the Australia Telescope National Facility (https://ror.org/05qajvd42). Operation of ASKAP is funded by the Australian Government with support from the National Collaborative Research Infrastructure Strategy. ASKAP uses the resources of the Pawsey Supercomputing Research Centre. Establishment of ASKAP, Inyarrimanha Ilgari Bundara, the CSIRO Murchison Radio-astronomy Observatory and the Pawsey Supercomputing Research Centre are initiatives of the Australian Government, with support from the Government of Western Australia and the Science and Industry Endowment Fund. This research made use of the following PYTHON packages: ASTROPY (Astropy Collaboration et al. 2013, 2018), a community-developed core Python package for Astronomy, MATPLOTLIB (Hunter 2007), a Python library for publication quality graphics, NUMPY (van der Walt et al. 2011; Harris et al. 2020), and PANDAS (Wes McKinney 2010; McKinney 2011).

Data Availability

The ASKAP data analysed in this paper (RACS-low and VASTP-low) can be accessed through the CSIRO ASKAP Science Data Archive (CASDA[2]) under project codes AS110 and AS107.

[2] https://data.csiro.au/domain/casdaObservation

Chapter 4

Two year monitoring of auroral pulses from the slowly rotating ultracool dwarf SCR J1845−6357

This chapter is being prepared for submission to the Monthly Notices of the Royal Astronomical Society. All content included in this chapter is my own work unless otherwise stated—including writing the manuscript, production of tables and figures, ATCA observations, development of the DStools *package, data reduction and formation of dynamic spectra for all ASKAP and ATCA data, analysis of the dynamic spectra and writing the manuscript—with specific contributions from co-authors described below. Dougal Dobie and Andrew Zic contributed to writing the ATCA observing proposal (C3486; PI Dougal Dobie) and contributed to performing the observations. Tim White made contributions to this work by processing the TESS lightcurve data.*

4.1 Introduction

Ultracool dwarfs (UCDs) are fully convective dwarf stars with spectral type later than ∼M7. These stars are known to produce highly circularly polarised radio emission in broadband pulses with a periodicity driven by stellar rotation (e.g. Hallinan et al. 2006; Lynch et al. 2015; Rose et al. 2023). The emission is widely believed to be powered by the electron cyclotron maser instability (ECMI; Wu & Lee 1979), a coherent emission mechanism that produces highly circularly polarised emission beamed into the walls of a hollow cone with opening angle near perpendicular to the local magnetic field (Treumann 2006). The ECMI operates at the local relativistic cyclotron frequency $\omega_e = eB/\gamma m_e c$ where B is the local magnetic field strength, c is the speed of light, γ is the Lorentz factor, and e and m_e are the electron charge and mass respectively, and is therefore an excellent tracer of stellar magnetism.

Analogous emission is produced in auroral density cavities near the polar caps of the magnetised Solar system bodies—in particular Earth, Jupiter, and Saturn—where auroral current systems drive instabilities in the electron velocity distribution providing free energy to the maser (Zarka 1998; Ergun et al. 2004). The origin of auroral currents in these systems can be traced to either magnetic reconnection with the Solar wind (Desch & Rucker 1983; Borovsky et al. 1998; Nichols & Milan 2016) or electrodynamic interaction with a local source of plasma such as the volcanic outflows from Io and Enceladus (Hill 2001; Cowley & Bunce 2001, 2003). In the Jovian context, radio emissions are produced from the polar magnetic caps due to field aligned currents that are driven by a breakdown in co-rotation between the planet and surrounding plasma (Cowley & Bunce 2001). Auroral radio emission is also produced along localised magnetic flux tubes, whose field aligned currents are generated by sub-Alfvénic interaction with Io (Saur et al. 2013). The localised nature of Io-controlled auroral emission results in beamed ECMI emission that is modulated at the Io orbital period rather than the Jupiter rotation period, and results in prominent arcs in dynamic spectra (Hess et al. 2008; Louis et al. 2017).

Ultracool dwarf auroral activity traces the presence of strong magnetic fields (Berger 2006), while other indicators of coronal magnetic activity—such as chromospheric line emission and X-ray emission—decline in the increasingly neutral atmospheres of these systems (Mohanty et al. 2002). These stars are beyond the fully convective boundary at spectral type M3 (Jao et al. 2018), and hence lack the tachocline that is a central component to the $\alpha-\Omega$ dynamo widely believed to generate the Solar magnetic field. Fully convective dynamo models either predict weak, disorganised fields (e.g. Durney et al. 1993), or strong global fields that depend upon rapid stellar rotation (e.g. Chabrier & Küker 2006; Dobler et al. 2006; Browning 2008; Christensen 2010). McLean et al. (2012) compiled a sample of 167 ultracool dwarfs with measured rotation periods and radio observations, finding a relationship between the ratio of radio to bolometric luminosity $L_\nu/L_{\rm bol}$ and Rossby number $R = P/\tau_c$, where P is the stellar rotation period and τ_c is the timescale of convective turnover in the stellar interior. This relationship spans stars of type G to L, reinforcing the importance of rapid stellar rotation in magnetic field production.

In this chapter I report the discovery of rotationally modulated auroral pulses from SCR J1845−6357, an M9.5 ultracool dwarf featuring the slowest rotation period among aurorally active ultracool dwarfs reported to date. I present results from a two year monitoring campaign with the Australian Square Kilometre Array Pathfinder (ASKAP; Johnston et al. 2008) and the Australia Telescope Compact Array (ATCA), with description of the observations and data reduction provided in § 4.2. In § 4.3 I summarise the known properties of SCR J1845−6357. In § 4.4 I describe the post-processing of ASKAP and ATCA data and formation of dynamic spectra, which I present in § 4.5 featuring a wide range of radio burst features, including highly circularly polarised, periodic auroral pulses and stochastic bursts. Finally, in § 4.6 I conclude with an outlook to future work on this dataset.

4.2 Observations and Data Reduction

4.2.1 ASKAP Observations

As part of the Deeper Wider Faster program (DWF; Andreoni & Cooke 2019) we conducted ASKAP observations of the NGC 6744 group centred on 19:08:00 −64:30:00 (J2000) for 80 min per night on six consecutive nights from 2021 September 5 to 10. The primary goal of the DWF program is the discovery of extragalactic transients. We additionally used five test observations of similar length conducted a week earlier and triggered three target-of-opportunity observations during and after the main DWF 2021 run, following the discovery of SCR J1845−6357. NGC 6744 was observed due to it being a nearby Milky-Way like galaxy at a declination that is suitable to observe simultaneously from Australia and Chile.

Observations were acquired with the CLOSEPACK36 Phased Array Feed (PAF; Hotan et al. 2014; McConnell et al. 2016) configuration of 36 dual-linear polarisation beams at 943.5 MHz with 288 channels each of 1 MHz width. The roll-axis of each ASKAP antenna is rotated during each observation to keep the beam footprint fixed on the sky and maintain the orientation of the linear feeds with respect to the celestial coordinate frame. Roll-axis adjustment also prevents the need for parallactic angle correction, simplifying the calibration of frequency-dependent XY phases and formation of data products in Stokes I, Q, U, and V polarisations. Data were calibrated and imaged with the ASKAPSOFT package (Cornwell et al. 2011; Guzman et al. 2019) and used the SELAVY source finder to extract a catalogue of 2D Gaussian source components from each Stokes I image. We ran SELAVY on the Stokes V images with the same, standard ASKAPSOFT settings, and used the FLAGNEGATIVE option to generate component lists in both positive and negative Stokes V.

We searched for transients in the DWF 2021 observing run through three independent search techniques: a standard variability search between nightly observations using the Variables And Slow Transients (VAST) pipeline (Murphy et al. 2021; Pintaldi et al. 2022), a high-time resolution variability search for short-duration transients with the VAST 'fast-imaging' pipeline (Wang et al. 2022b), and a search for sources with significant fractional circular polarisation with the VAST Stokes V pipeline. A full analysis and description of the DWF 2021 dataset and transient search are presented in Dobie et al. (2023).

Table 4.1: Summary of 943 MHz ASKAP observations. Columns are the observation Scheduling Block ID (SBID), start time, and duration.

SBID	UT Start Time	t_{obs} (min)
31349	2021–08–27 16:38	80
31584	2021–09–02 05:43	80
31640	2021–09–03 05:17	80
31651	2021–09–03 09:28	80
31700	2021–09–04 05:24	60
31750	2021–09–05 05:01	80
31821	2021–09–06 05:01	80
31882	2021–09–07 05:05	80
31944	2021–09–08 05:01	80
32015	2021–09–09 05:06	80
32018	2021–09–09 12:10	420
32035	2021–09–10 05:01	80
32039	2021–09–10 12:10	420
32235	2021–09–10 05:21	600

During the 2021–09–05 observation we detected a 100 % circularly polarised 3 mJy point source at 18:45:13.7784−63:57:34.9632 (J2000) that showed variability over the duration of the observation. The astrometric accuracy of this detection is $\sim 2''$, incorporating both the systematic astrometric accuracy and SNR dependent positional uncertainty. Using proper motion parameters from Gaia Data Release 3 (Gaia DR3; Gaia Collaboration et al. 2023), we applied astrometric corrections to stars within $3'$ of the radio position and associated the source with the ultracool dwarf star SCR J1845−6357 with a match separation of $0.32''$.

Following initial detection we monitored the source over each subsequent DWF 2021 epoch and triggered three longer target-of-opportunity observations of roughly 8 h duration to search for further evidence of variability on short timescales. The observing parameters for all ASKAP observations presented in this work are summarised in Table 4.1.

4.2.2 ATCA Monitoring

Following initial discovery we conducted regular monitoring of SCR J1845−6357 with the Australia Telescope Compact Array (ATCA) from 2021 September 15 to 2023 August 27. We conducted six target-of-opportunity observations under project code CX488, and 13 observations under the full proposal project code C3486. Observations were conducted primarily with the 16 cm (L-band) receiver with a 2048 MHz band centred at 2100 MHz, with a few observations using the 4 cm (C/X-band) receiver with two simultaneous 2048 MHz bands centred at 5500 MHz and 9000 MHz. We determined the bandpass response and flux scale of each observation with the ATCA primary calibrator PKS B1934−638, and tracked the evolution of complex gains with interleaved scans of either PKS B1934−638, or 1814−637 when PKS B1934−638 was at low elevation, with early observations using 20–30 min target scans interleaved with 120 s scans of the gain calibrator. From 2022 Oct onwards we adapted to 2 h target scans interleaved with 90 s calibrator scans to reduce the probability of missing or interrupting observations of short duration pulses, and relied upon self-calibration to solve for the time-dependent antenna gains. The observing parameters and dates for all ATCA observations are summarised in Table 4.2.

We performed basic flagging and calibration of all ATCA observations with the MIRIAD software package. From 2023 January onwards we conducted observations with the array phase-centre shifted 120″ to the south of the pointing centre—which was kept aligned with both target and calibrator scans—in order to avoid corruption by phase-centre errors that became noticeable in observations from 2022 October. Prior to flagging and calibration we shifted the phase-centre of all visibilities back 120″ to the north with the MIRIAD task UVEDIT. We then flagged visibilities affected by radio frequency interference (RFI) via manual inspection and the 'sumthreshold' autoflagging routine with the PGFLAG task. We derived corrections to the bandpass response and flux scale from PKS B1934−638 and copied solutions to 1814−637, then used the GPCAL task to determine time-dependent complex gain corrections from PKS B1934−638 and 1814−637, and finally applied all calibration solutions to SCR J1845−6357.

4.3 SCR J1845−6357 Properties

SCR J1845−6357 is a binary system consisting of a type M9.5V ultracool dwarf (Koen et al. 2017) and T6.5V brown dwarf (Vigan et al. 2012) separated by ∼4 AU. The binary is located at a distance of 4.005 ± 0.002 pc resulting in an angular separation at the DWF 2021 epoch of ∼1″. The system age is estimated at 1.8–3.1 Gyr, based on brown dwarf evolutionary models (Burrows et al. 1997) and the derived SCR J1845−6357B temperature of 950–1000 K and radius of $0.88R_\mathrm{J}$. SCR J1845−6357 demonstrates multiple indicators of strong magnetic activity, with frequent optical flares and an active chromosphere (Koen et al. 2017). We summarise the known stellar properties of SCR J1845−6357A in Table 4.3.

SCR J1845−6357 was covered by sector 13 of the Transiting Exoplanet Survey Satellite (TESS; Ricker 2015) telescope between 2019-06-19 and 2019-07-17 at a 120 s cadence with photometry acquired in a 600–1000 nm passband. As the large proper motion of SCR J1845−6357 can result in significant misalignment of target pixels with the position assumed by the TESS pipeline, we manually selected target pixels at the SCR J1845−6357 position proper motion corrected to the beginning of the TESS epoch and extracted the Pre-search Data Conditioning Simple Aperture Photometry (PDCSAP) time-series, and cleaned the data of samples with poor quality flags. Multiple optical flares are visible throughout the lightcurve as well as a periodic modulation. We computed a Lomb-Scargle periodogram on the TESS lightcurve, revealing a clear dominant period of 14.1 h that we interpret as the stellar rotation period modulating an uneven distribution of starspots. The TESS lightcurve and Lomb-Scargle periodogram are displayed in Figure 4.1.

Table 4.2: Summary of ATCA observations. Columns are the UTC date and time at the beginning of each observation, observation duration t_{obs}, central observing frequency ν, ATCA array configuration code, and shortened names of the gain calibrator used in each observation.

UT Start Time		t_{obs} (min)	ν (GHz)	Array	Gain Calibrator[a]
2021–09–15	14:27	202	5.5/9	6A[b]	1934
2021–09–16	08:32	554	2.1	6A[b]	1934
2021–10–18	05:15	100	5.5/9	H168	1814, 1934
2021–10–18	22:31	133	5.5/9	H168	1814, 1934
2021–10–20	04:05	170	5.5/9	H168	1814, 1934
2021–10–22	22:47	178	5.5/9	H168	1814, 1934
2022–04–08	12:34	890	2.1	6A	1934
2022–04–09	11:30	957	2.1	6A	1814, 1934
2022–09–22	00:25	948	2.1	6D	1814, 1934
2022–09–23	00:37	1 016	2.1	6D	1814, 1934
2022–10–01	00:19	937	2.1	6D	1814, 1934
2022–11–11	22:17	915	2.1	6C	1814, 1934
2023–01–01	18:18	943	2.1	6C	1814, 1934
2023–02–05	15:35	955	2.1	6C	1814, 1934
2023–05–30	08:46	937	2.1	6D	1814, 1934
2023–07–01	06:19	941	2.1	6D	1814, 1934
2023–07–23	04:41	1 002	2.1	6D	1814, 1934
2023–08–27	02:27	959	2.1	6D	1814, 1934

[a] Calibrator shorthands 1814 and 1934 correspond to 1814−637 and PKS B1934−638 respectively.

[b] September 2021 observations were conducted during a maintenance period, with only three antennas available on 2021–09–15 and four antennas available on 2021–09–16.

4.4 Dynamic Spectrum Processing

We further processed calibrated ASKAP and ATCA visibilities with DStools [1], a custom CASA and python package for production of dynamic spectra. We formed dynamic spectra by rotating the phasecentre to the position of SCR J1845−6357 and averaging the time and frequency dependent complex visibilities over all baselines, generating a 2D array representing the received flux at the phasecentre as a function of time and frequency. Below we describe each processing stage.

[1] github.com/askap-vast/dstools

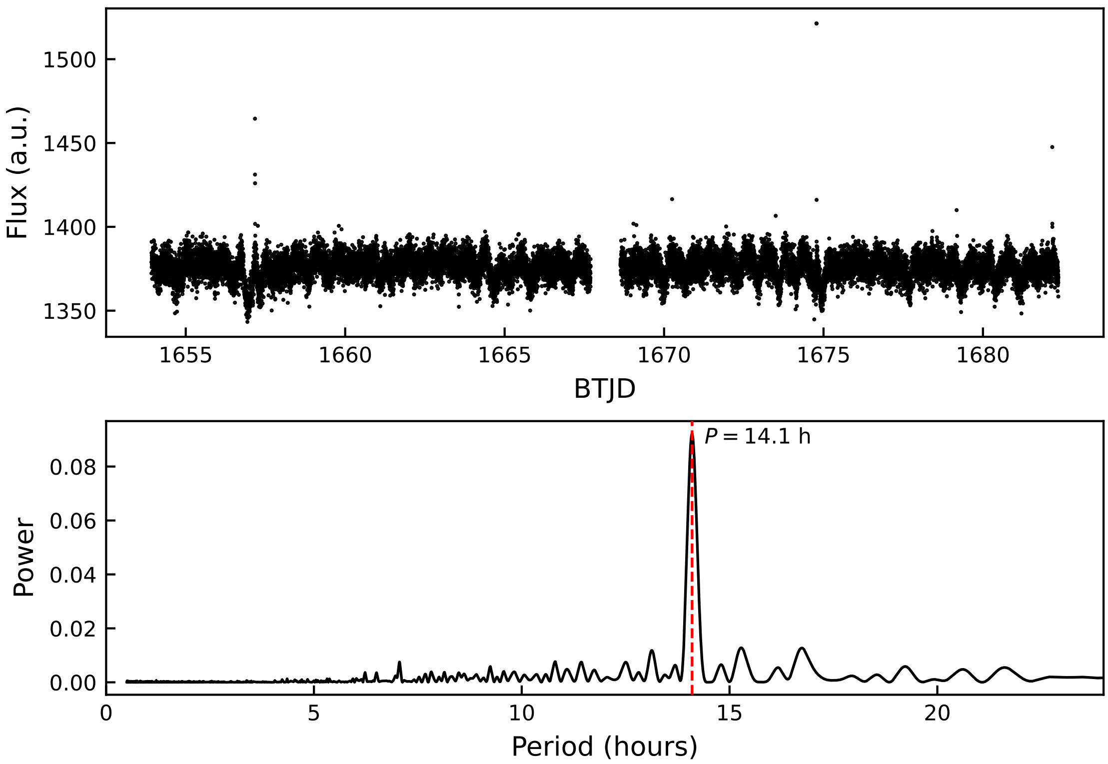

Figure 4.1: Lightcurve and Lomb-scargle periodogram from sector 13 TESS observations of SCR J1845−6357. Time is reported in the Barycentric TESS Julian Day (BTJD) format where BTJD = BJD − 2 457 000 d. The peak at 14.1 h is highlighted as the stellar rotation period, visible as a modulation in the lightcurve due to uneven starspot coverage.

4.4.1 Formation of Dynamic Spectra Data Products

Field Modelling and Subtraction

The flux received at the phasecentre is contaminated by the frequency dependent sidelobe patterns of other sources in the field, which rotate over the phasecentre with time and result in arc-like patterns in the time-frequency plane. To remove sidelobe contamination we modeled sources in the field with the CASA task TCLEAN, using the multi-term multi-frequency synthesis deconvolver. This algorithm decomposes the gridded data into multiple Taylor terms and splits the data into multiple separate planes, each representing a smoothed copy of the Taylor term image at a supplied spatial scale, and improves the deconvolution of sources with extended and spectral structure. We modeled the SCR J1845−6357 field with spatial scales of 0, 4, and 8 pixels and a cell size of 0.66″, using three Taylor terms to capture both a spectral slope and curvature in field sources. We gridded the visibilities using ‘briggs’ weighting with a robust parameter of 0.5, and enabled w-projection to appropriately capture the effect of sky curvature and reduce widefield imaging artefacts. This is particularly important for the observed SCR J1845−6357 field with ATCA, which contains a bright ∼0.6 Jy source at the edge of the primary beam that is poorly modeled with standard gridding.

Table 4.3: Summary of SCR J1845−6357A properties.

Property	Value		Reference
Spectral Type	M8.5e–M9.5Ve		Kasper et al. (2007); Koen et al. (2017)[a,b]
Age	1.8–3.1	Gyr	Kasper et al. (2007); Vigan et al. (2012)
$P_{\rm rot}$	14.100 ± 0.005	h	This work
$T_{\rm eff}$	2600	K	Kasper et al. (2007)[a]
$L_{\rm bol}$	10^{30}	erg/sec	Robrade et al. (2010)
α (J2000)	18:45:05.2532		Gaia Collaboration et al. (2023)
σ_α	0.0713	mas	Gaia Collaboration et al. (2023)
δ (J2000)	−63:57:47.4501		Gaia Collaboration et al. (2023)
σ_δ	0.0831	mas	Gaia Collaboration et al. (2023)
π	249.661 ± 0.133	mas	Gaia Collaboration et al. (2023)
d	4.005 ± 0.002	pc	Gaia Collaboration et al. (2023)
$\mu_\alpha \cos\delta$	2583.378 ± 0.091	mas/yr	Gaia Collaboration et al. (2023)
μ_δ	588.504 ± 0.103	mas/yr	Gaia Collaboration et al. (2023)

[a] Spectral type and $T_{\rm eff}$ of M8.5e / 2600 K from Kasper et al. (2007) using 8.7 Å resolution optical spectra.

[b] Spectral type of M9.5e from Koen et al. (2017) using 1 Å resolution NIR spectra.

Using the above settings along with other standard TCLEAN options we produced 4500 × 4500 pixel images of the ATCA L-band data and cleaned the field down to a threshold of 80 µJy. We used the resulting field model to perform phase-only self-calibration and repeated rounds of cleaning and self-calibration until solutions converged, typically two rounds. We then performed a final deep clean to a threshold of 30 µJy to produce a model of all sources in the field and masked clean components corresponding to SCR J1845−6357 in each Taylor term model image. We then inserted each model image into the visibilities using TCLEAN, and subtracted the masked model from the data with the UVSUB task to produce visibilities representing emission coming from SCR J1845−6357 alone.

Extraction of Dynamic Spectra Products

We rotated the phasecentre of the subtracted visibilities to the proper motion corrected position of SCR J1845−6357 for each epoch and averaged along the baseline axis, discarding visibilities with a projected baseline distance of less than 500 m to mitigate excess contamination due to RFI that preferentially affects short baselines. The amplitude of the baseline-averaged visibilities then represents the received flux at the phasecentre as a function of time and frequency, while the phase component represents emission away from the phasecentre. Finally, we extracted the time and frequency arrays and complex visibilities for the XX, XY, YX, and YY instrumental polarisations into numpy arrays for further post-processing.

4.4.2 Post-processing of Dynamic Spectra

Final presentation of a dynamic spectrum requires various stages of post-processing depending upon the quality and content of the data. Here we describe the post-processing stages which we used selectively on our ASKAP and ATCA observations of SCR J1845−6357.

Formation of Stokes Products

Instrumental polarisations are formed into the Stokes products with the following definitions to align with the IAU/IEEE Stokes V convention:

$$\begin{aligned} I &= (XX + YY)/2 \\ Q &= (XX - YY)/2 \\ U &= (XY + YX)/2 \\ V &= i(YX - XY)/2 \end{aligned}$$

Time and Frequency Binning

Faint features in a dynamic spectrum require binning in time and/or frequency to increase SNR. A standard approach to binning a 2D array along one axis is to reshape the array into a 3D cube with the third axis representing the flux to be binned, average along the third axis, and then reshape back to a 2D array with smaller, binned dimensions. However, this approach is limited to using bin sizes that are factors of the original array dimensions. This can be problematic for the formation of dynamic spectra of stellar radio bursts, where maximising SNR while still resolving the time and frequency structure present in a burst requires finer control over the level of binning.

DStools employs time and frequency averaging using a weighted re-distribution of flux density into arbitrary new array dimensions while preserving the mean flux in each time and frequency slice. The time-weight matrix $\mathbf{W_t}$ is computed as a t_c-diagonal matrix so that each row sums to 1 and each column sums to the time compression factor $t_c = m_b/m_o$, where m_o and m_b are the respective number of time samples in the original and binned array. The frequency-weight matrix $\mathbf{W_f}$ is constructed similarly for the frequency axis, and then the binned array $\bar{\mathbf{A}}$ is computed as

$$\bar{\mathbf{A}} = \mathbf{W_t} \mathbf{A} \mathbf{W_f^T}. \tag{4.1}$$

This transformation symmetrically aggregates flux density from neighbouring time and frequency bins to boost SNR without affecting the mean flux density or central time and frequency of emission features, and is equivalent to the standard 2D binning approach when using integer time and frequency compression factors.

Folding

Often dynamic spectra of radio stars show features that are periodic in time, such as beamed auroral pulses that are modulated by stellar rotation. Folding the data on the relevant time period can boost SNR to allow detailed inspection of time and frequency structure without the loss in temporal resolution caused by binning. DStools employs folding of dynamic spectra to a specified period and phase offset by splitting the data into periodic chunks which are then stacked and averaged. This can be incorporated alongside time / frequency binning to fine-tune the balance of SNR and spectral / temporal resolution.

4.5 Results

4.5.1 ASKAP Pulses

Throughout the ASKAP DWF 2021 run we made a detection of SCR J1845−6357 in Stokes I every epoch with a flux density of $\sim$0.5 mJy, and in five observations we detected brighter emission at the $\sim$2 mJy level with 100 % fractional circular polarisation. These properties are suggestive of highly polarised auroral pulses along with slowly variable quiescent emission—which is a ubiquitous component to the radio emission of aurorally pulsing ultracool dwarfs (Williams 2018). To search for periodicity in the pulsed emission we produced visibility lightcurves for all DWF 2021 observations by first forming dynamic spectra with DSTOOLS then averaging over all frequency channels. We then computed a Lomb-Scargle periodogram (Lomb 1976; Scargle 1982) with the combined visibility lightcurves using three Fourier terms to appropriately fit an asymmetric pulse profile, shown in the top panel of Figure 4.2 with a peak period of 14.09 ± 0.06 h.

In the middle and bottom panels of Figure 4.2 we show the visibility lightcurves from all ASKAP observations of SCR J1845−6357 folded to the peak period of 14.09 h. The middle panel shows the pulse profile in Stokes I and V, with an unpolarised 0.5 mJy quiescent state visible underneath a 100 % circularly polarised pulse lasting for 2 h. The bottom panel shows the Stokes I lightcurve colourmapped by time since the first ASKAP observation SB31349. The pulse profile is stable over a timescale of two weeks, with the final two pulse detections at 14 and 21 d beginning to quench back to a quiescent state.

4.5.2 ATCA Dynamic Spectra

Our observations with ASKAP demonstrate a clear rotational modulation of the pulsed emission with the ASKAP derived radio period in close agreement to the 14.100 ± 0.005 h rotation period inferred from TESS, and also showed signs of a transient nature to the pulse with a weakening of the pulse profile in the final two observations. ASKAP lacks the instantaneous sensitivity required to resolve time and frequency structure in dynamic spectra of the 2 mJy pulses, so we monitored SCR J1845−6357 with ATCA over a period of two years to search for continued pulse emission, make improved measurements of the pulse sub-structure, polarisation, duration, and frequency cutoffs, and track the evolution of these properties over timescales of weeks to years. We generated dynamic spectra and visibility lightcurves for all ATCA observations using DSTOOLS, and discuss the properties of emission features captured in each observation in the following section.

September 2021: We acquired the first followup observations of SCR J1845−6357 with ATCA five days after the final DWF 2021 pulse detection with ASKAP, with

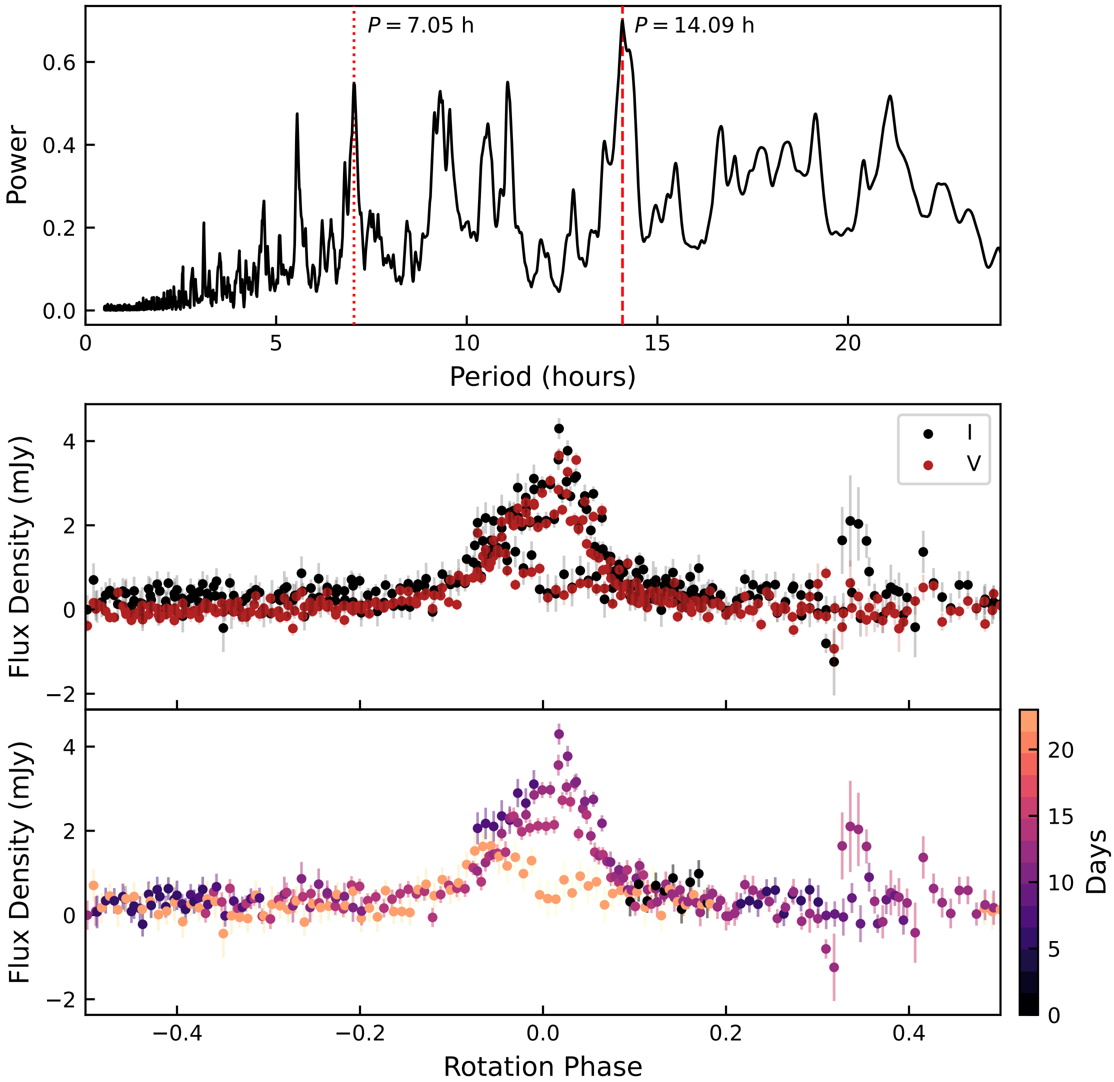

Figure 4.2: Pulse periodicity in visibility lightcurves from all DWF 2021 ASKAP observations. Top: Lomb-Scargle periodogram showing a peak power at a period of 14.09 h. Middle: Stokes I and V visibility lightcurves folded to 14.09 h. Bottom: Folded Stokes I visibility lightcurve colourmapped by days since the first observation SB31349 on 2021 Aug 27. Lightcurves are binned to 7.5 min time samples and averaged over the full 288 MHz bandwidth.

a ~3.5 h observation with the C/X band receiver at 5500 and 9000 MHz on 2021–09–15 and ~10 h observation with the L-band receiver at 2100 MHz on 2021–09–16. Both observations were conducted under a target of opportunity application during a maintenance period, with only three antennas available at C/X-band and four antennas at L-band.

In Figure 4.3 we show dynamic spectra and lightcurves of the 2021–09–16 L-band observation in Stokes I and V, binned to a time and frequency resolution of 150 s and 25 MHz respectively. Despite limited uv-coverage and sensitivity with two missing antennas, we detected a 3 mJy pulse lasting 1 h and covering the entire unflagged

1700 MHz bandwidth. In contrast to the ASKAP detected pulses which were all 100 % right-hand circularly polarised (RCP), the ATCA pulse is 50 % left-hand circularly polarised (LCP) suggesting an opposite magnetic field geometry in the two source regions.

We did not detect any pulses in the 2021–09–15 observation at C/X-band, which could be explained by the limited observation duration covering only ∼20 % of the rotational phase which did not align with the L-band pulse. We therefore acquired four additional observations at C/X-band between 2021–10–18 and 2021–10–22 using the hybrid H168 array configuration. While this configuration is unsuitable for L-band observing as the *uv*-coverage is concentrated on short baselines resulting in poor angular resolution, the narrow C/X-band field of view does not contain any field sources bright enough to cause confusion. With these observations we sampled the rest of the SCR J1845−6357 rotation phase, with no detection of any pulses.

April 2022: From April 2022 we observed SCR J1845−6357 at 2100 MHz in 15–16 h blocks in order to contiguously cover the full 14.1 h rotation period. We observed SCR J1845−6357 over two consecutive days on 2022–04–08 and 2022–04–09 and show the Stokes I and V dynamic spectra and visibility lightcurves in Figures 4.4 and 4.5. Over the two days we detected three 100 % RCP pulses—10 h into the first observation, and 1 h and 15 h into the second observation—each extending from the bottom of the band to an upper frequency cutoff of 2200 MHz.

We determined the periodicity of the repeat pulses by computing a two-dimensional auto-correlation function (2D ACF) on the Stokes V dynamic spectra, which is less contaminated by residual sidelobes than Stokes I and is therefore less impacted by periodic sidelobe emission. We show the auto-correlation as a function of time and frequency lag along with the ACF time lag trace at zero-frequency lag in Figure 4.6. The 2D ACF shows no correlated structure over the frequency axis, but peaks at a time-lag of 14.06 h—closely aligned with both the TESS and ASKAP pulse periods. We used DSTOOLS to fold the dynamic spectra into three 14.06 h chunks aligned in rotation phase, shown in Figure 4.7. The three pulses occur consecutively over each period and are aligned in rotation phase indicating they originate from the same active auroral region detected over two full stellar rotations.

September 2022: We observed SCR J1845−6357 over another two consecutive days on 2022–09–22 and 2022–09–23, and show the Stokes I and V dynamic spectrum and visibility lightcurves from 2022–09–22 in Figure 4.8. We detected a bright 100 % LCP pulse showing strong frequency dependence with a lower frequency cut-off at 1700 MHz and break in emission between 2200–2700 MHz. This pulse is much shorter than any of the previously detected pulses with a duration of 2 min, and is significantly brighter reaching a peak flux density of 25 mJy in the unbinned data. We made no pulse detections on 2022–09–23 despite covering a full stellar rotation, indicating the source of the 2022–09–22 pulse quenched within a timescale less than 14.1 h. It is then possible the short pulse duration is intrinsic to the emission rather than caused by rotational modulation of the highly beamed ECMI cone, as the stable, rotationally modulated pulse profiles were in previous observations.

October 2022–January 2023: We observed SCR J1845−6357 on 2022–10–01,

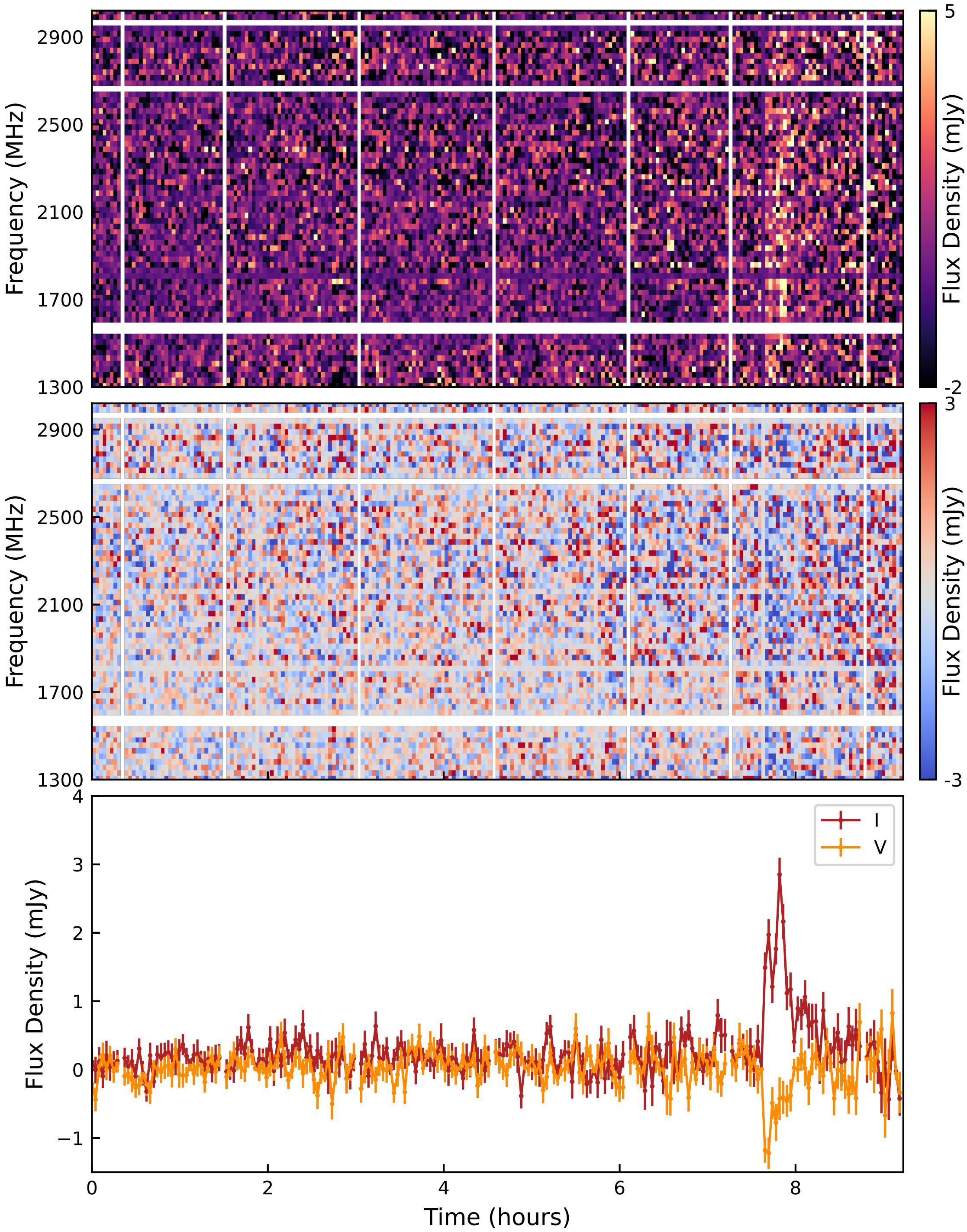

Figure 4.3: Dynamic spectrum of 2021–09–16 2100 MHz ATCA observation of SCR J1845−6357 in Stokes I (top) and V (middle), and frequency averaged visibility lightcurve (bottom). A 50 % left circularly polarised burst is visible at 7.5 h spanning the full 2048 MHz band. Data have been binned to a time resolution of 150 s and frequency resolution of 25 MHz. Data gaps correspond to flagged channel ranges due to excess RFI and off-source time during calibrator scans.

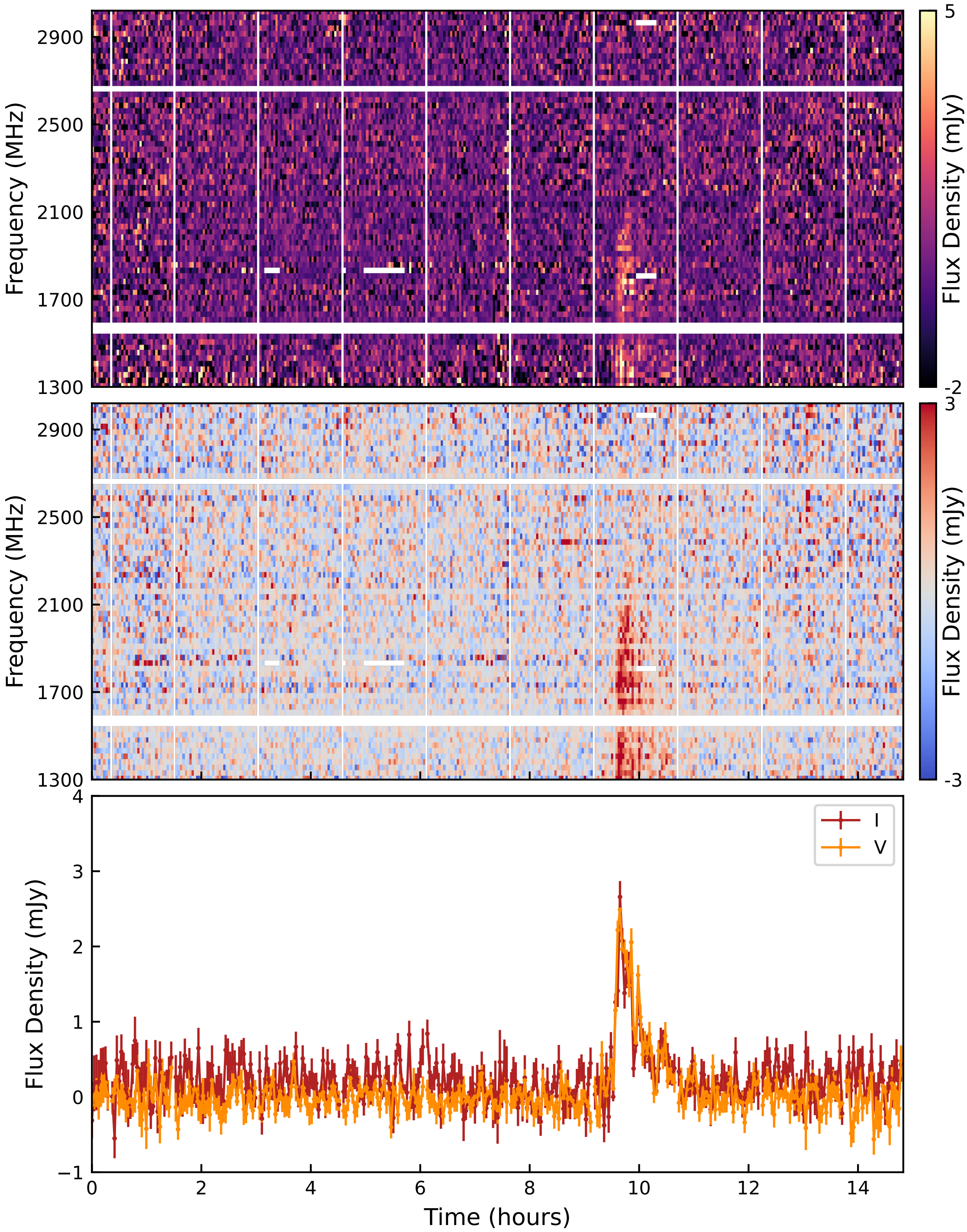

Figure 4.4: Dynamic spectrum of 2022–04–08 2100 MHz ATCA observation. A 100 % right circularly polarised burst is visible at 10 h with an upper frequency cutoff of 2200 MHz. The visibility lightcurves are formed from averaging the dynamic spectra over the 1300–2200 MHz frequency range. Other details are as in Figure 4.3.

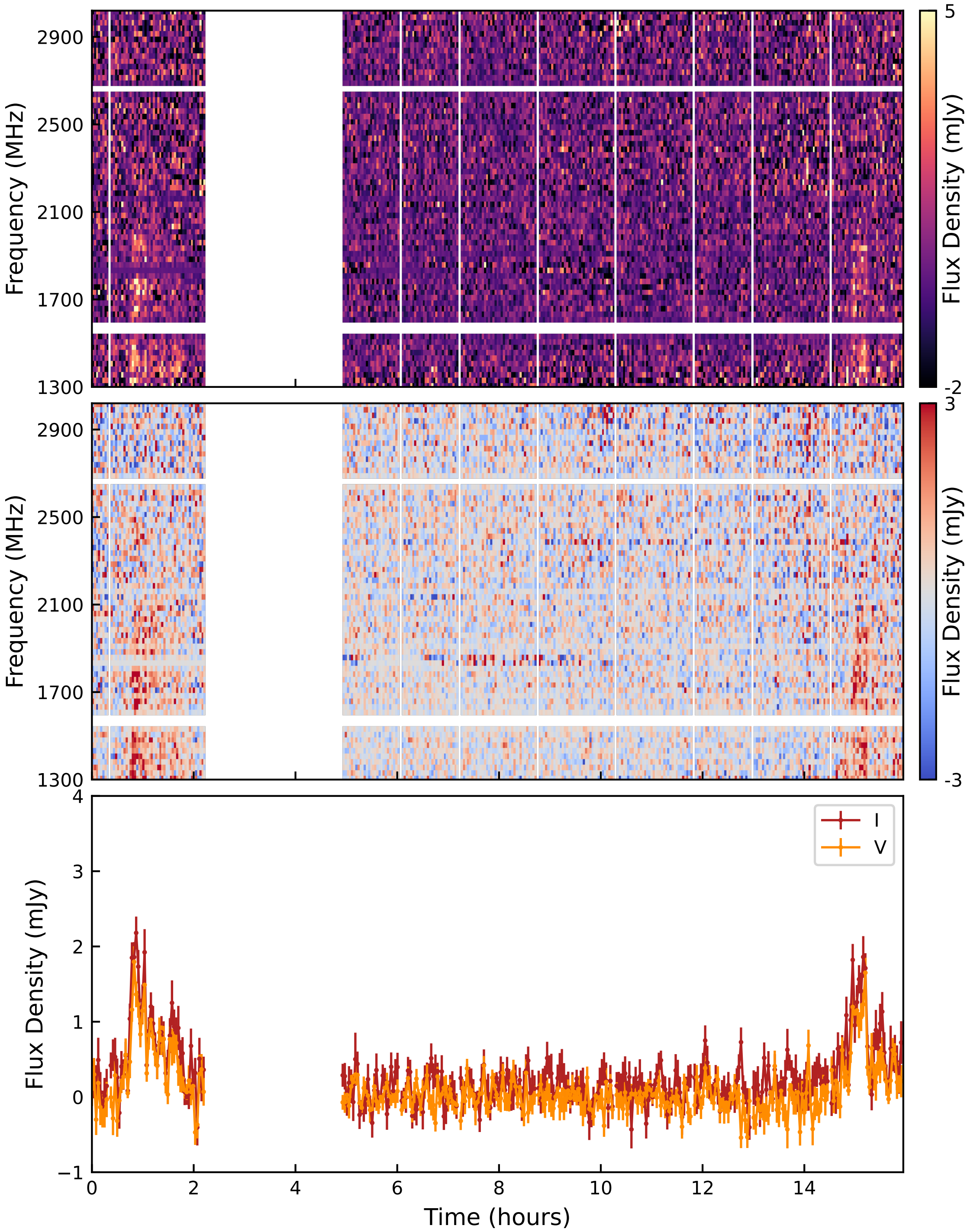

Figure 4.5: Dynamic spectrum of 2022–04–09 2100 MHz ATCA observation of SCR J1845−6357. 100 % right circularly polarised pulses are visible at 1 h and 15 h with an upper frequency cutoff of 2200 MHz. The visibility lightcurves are formed from averaging the dynamic spectra over the 1300–2200 MHz frequency range. Other details are as in Figure 4.3.

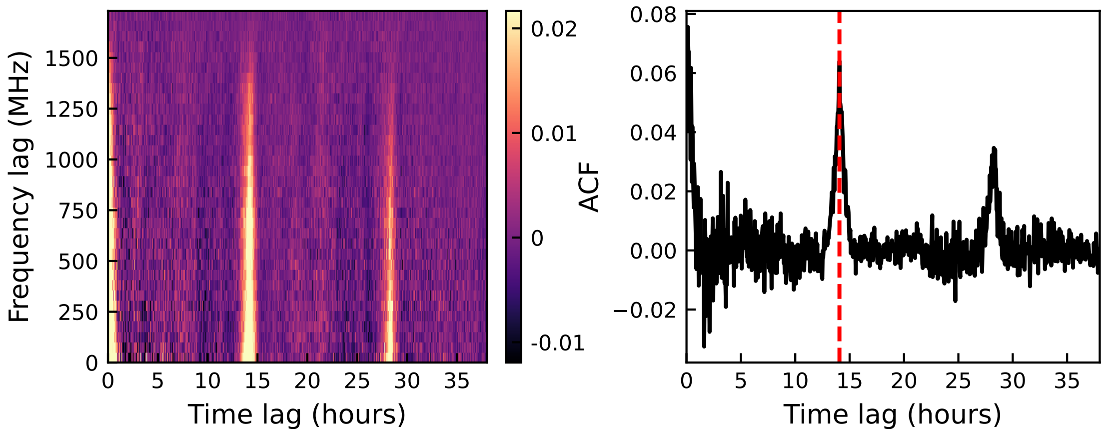

Figure 4.6: Two-dimensional autocorrelation function (ACF; left) and zero frequency-lag ACF trace (right) of visibility lightcurves from 2100 MHz ATCA observations on 2022–04–08 and 2022–04–09. The peak correlated time-lag of 14.06 h is shown by the dashed red line. The second peak at 28.12 h is an alias due to alignment between the first and third pulse detected in the observing run.

2022–11–11, and 2023–01–01 for 15–16 h each. In each epoch we detected quiescent emission in Stokes I with a flux density of 180–220 µJy, but made no pulse detections.

February 2023: We observed SCR J1845−6357 on 2023–02–05 and show the Stokes I and V dynamic spectrum and visibility lightcurves in Figure 4.9. We detected three main pulse features, with two 100 % RCP pulses showing sub-structure in time and frequency over a duration of 2–4 h, and a 2 min long 75 % LCP pulse covering a frequency range of 1600–3000 MHz. The RCP pulses are spaced 9 h apart and the LCP pulse occurs 4 h after the second RCP pulse, indicating that each pulse originates from a distinct emission site. The first RCP pulse is also undetected 14.1 h later, suggesting that the source of the emission is transient on the timescale of a single stellar rotation. This could be caused by quenching of the electron distribution powering an auroral pulse—as seen in the final two observations of DWF 2021—or an intrinsically short timescale to bursts unassociated with auroral activity.

May 2023: We observed SCR J1845−6357 on 2023–05–30 and show the Stokes I and V dynamic spectrum and visibility lightcurves in Figure 4.10. We detected a pair of 100 % RCP pulses lasting 4 h with an upper frequency cutoff at 1550 MHz and extending to the bottom of the band.

July 2023: We observed SCR J1845−6357 on 2023–07–01 with only detection of quiescent emission, and again on 2023–07–23 for which we show the Stokes I and V dynamic spectrum and visibility lightcurves in Figure 4.11. We detected a single 100 % RCP pulse lasting 30 min with a lower frequency cutoff at 2100 MHz and extending to the top of the unflagged band at 3000 MHz.

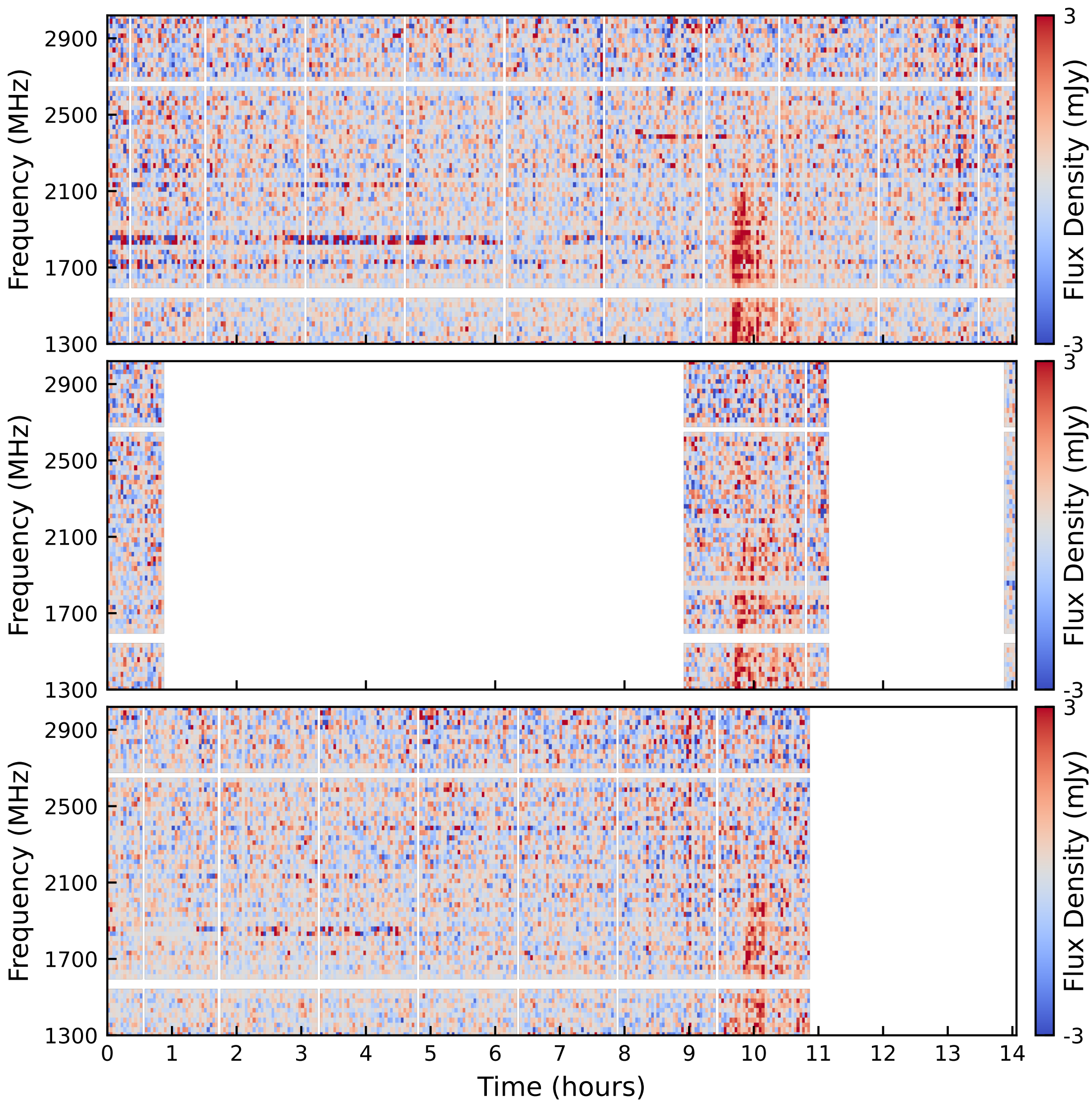

Figure 4.7: Rotation phase aligned Stokes V dynamic spectra showing three consecutive pulses in 2100 MHz ATCA observations on 2022–04–08 and 2022–04–09. Data have been folded to the derived SCR J1845−6357 rotation period of 14.06 h. Other details are as in Figure 4.3.

4.5.3 Auroral Pulse Properties

In the DWF 2021 observations with ASKAP we detected pulses over a period of two weeks that are periodic on the rotation period of $\sim$14.1 h, indicative of a persistent site of beamed auroral radio emission that is modulated by stellar rotation. When folded using the ASKAP pulse ephemeris used in Figure 4.2, the ATCA September 2021 pulse detected five days later arrives with a phase advance of ~ 0.1 or 85 min earlier than expected if associated with the ASKAP pulse emission site. This suggests the two pulses originate from separate regions in the magnetosphere, which is supported by the opposite sense of circular polarisation indicating opposing magnetic field orientations in source region of each pulse.

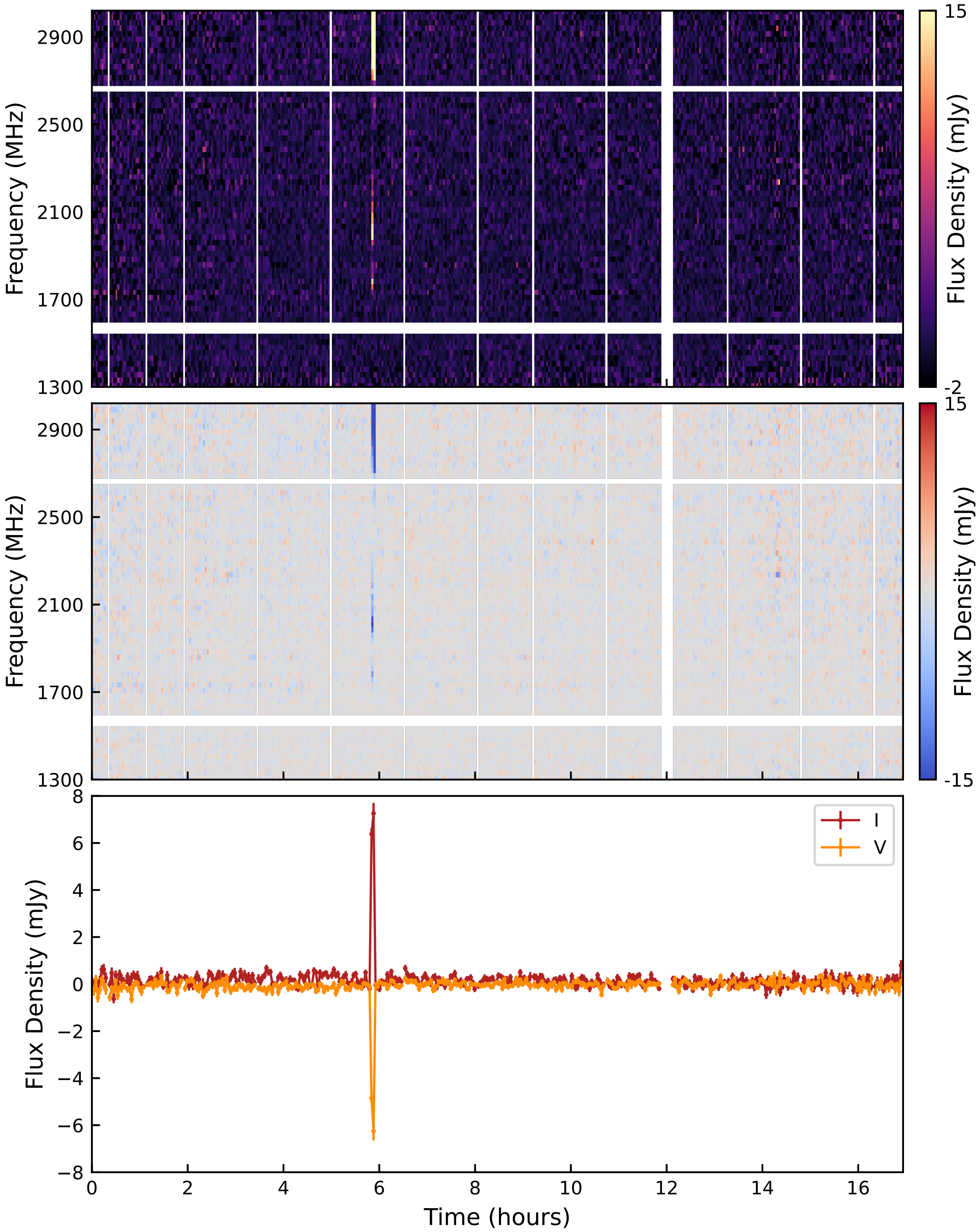

Figure 4.8: Dynamic spectrum of 2100 MHz ATCA observation on 2022–09–22. A short duration 100 % left circularly polarised pulse is visible at 6 h with a lower frequency cutoff of 1700 MHz and break in emission between 2200–2700 MHz. Other details are as in Figure 4.3.

The ATCA pulse extends over the full unflagged 1300–3000 MHz bandwidth and does not show signs of cutting off towards either end of the band, and the DWF 2021

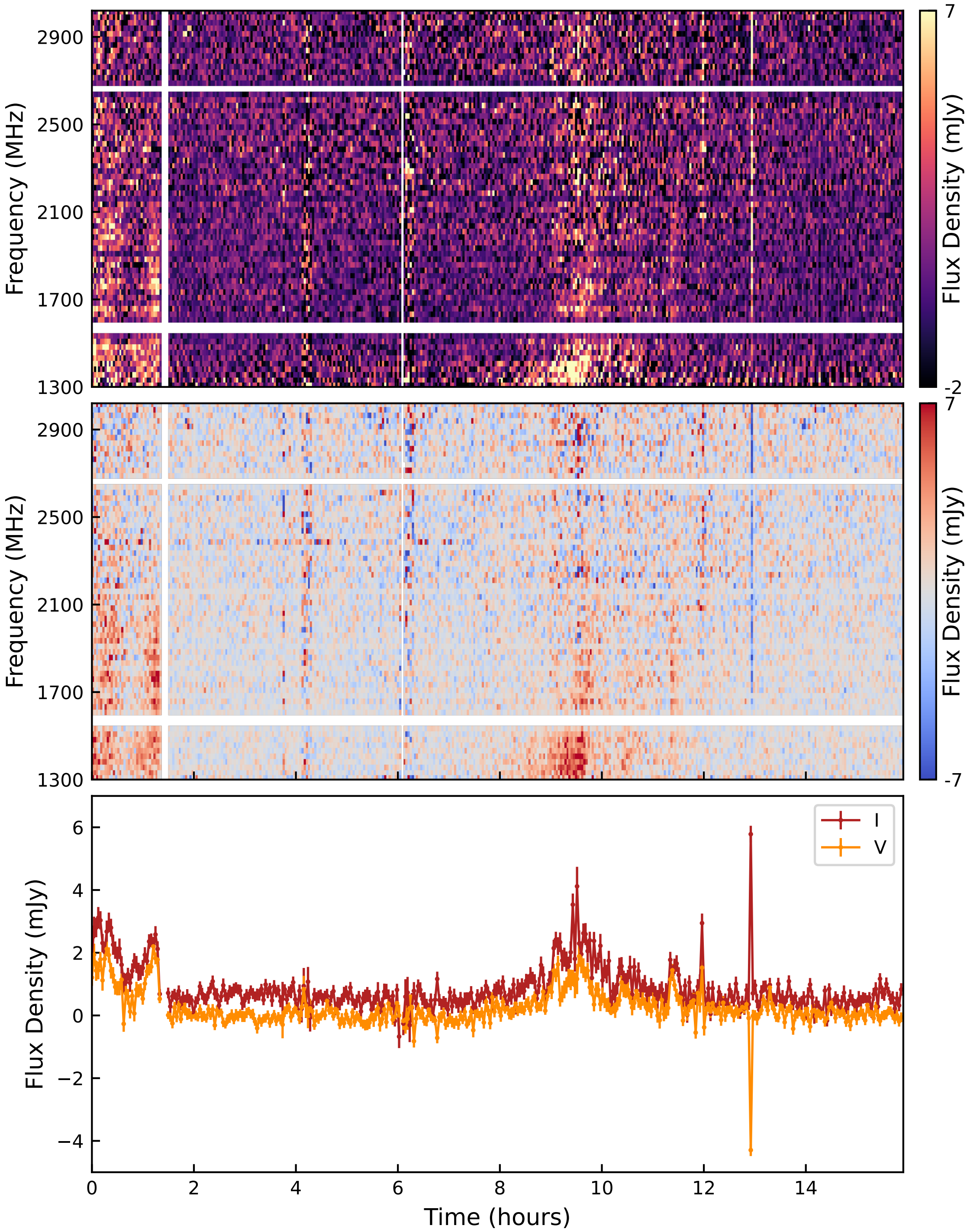

Figure 4.9: Dynamic spectrum of 2100 MHz ATCA observation on 2023–02–05. 2 h long 100 % RCP pulses are visible at 1 h and 9 h and a 2 min long 75 % LCP pulse at 13 h. Other details are as in Figure 4.3.

pulses similarly extend over the full 799–1087 MHz ASKAP band. As it is unlikely that two distinct broadband pulses would feature respective upper and lower cutoffs at the same frequency of ∼1200 MHz each of the pulses should have been detectable

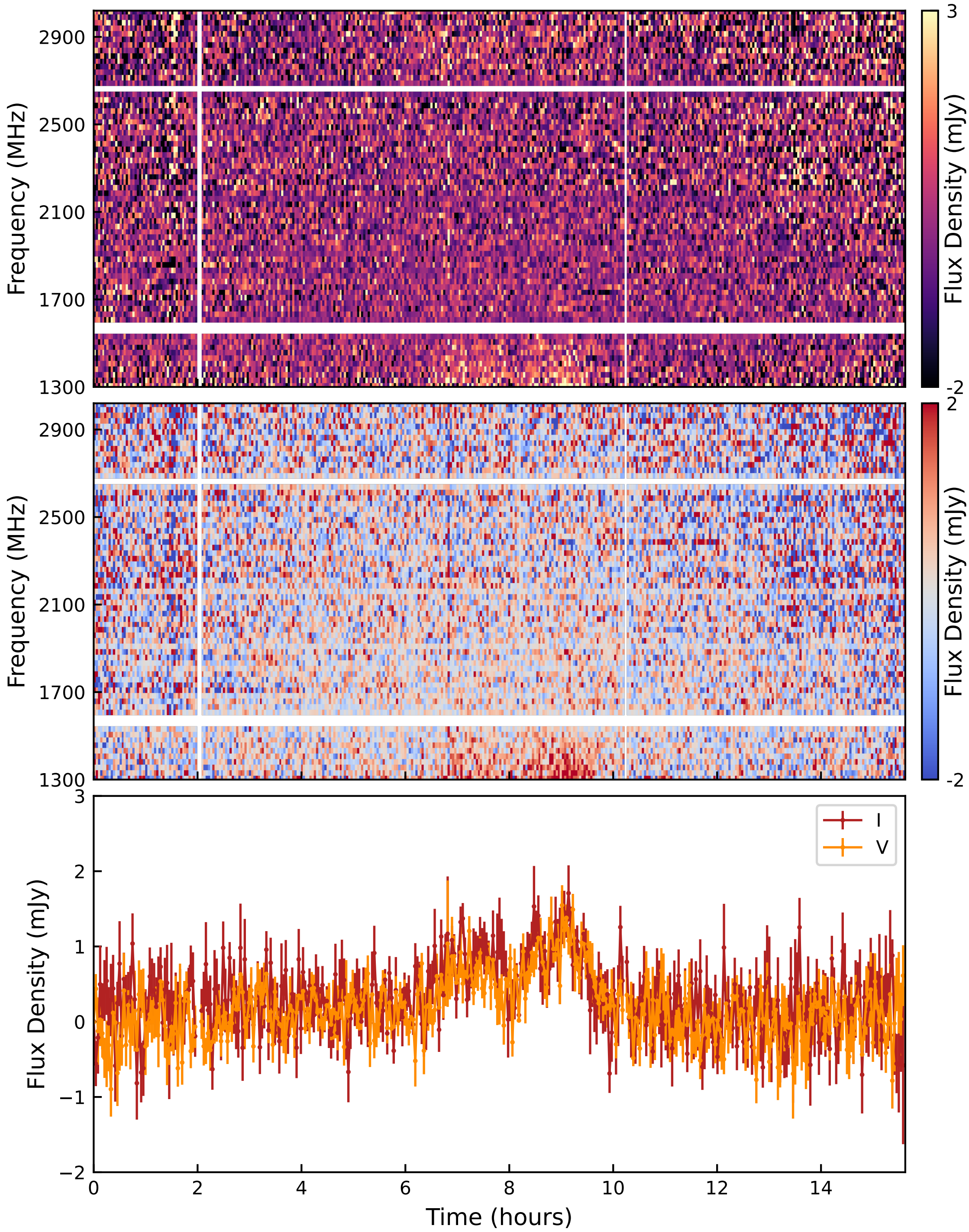

Figure 4.10: Dynamic spectrum of 2100 MHz ATCA observation on 2023–05–30. 100 % RCP emission is visible 6 h into the observation which is resolved into two 2 h long pulses with an upper frequency cutoff at 1550 MHz. The visibility lightcurves are formed from averaging the dynamic spectra over the 1300–1550 MHz frequency range. Other details are as in Figure 4.3.

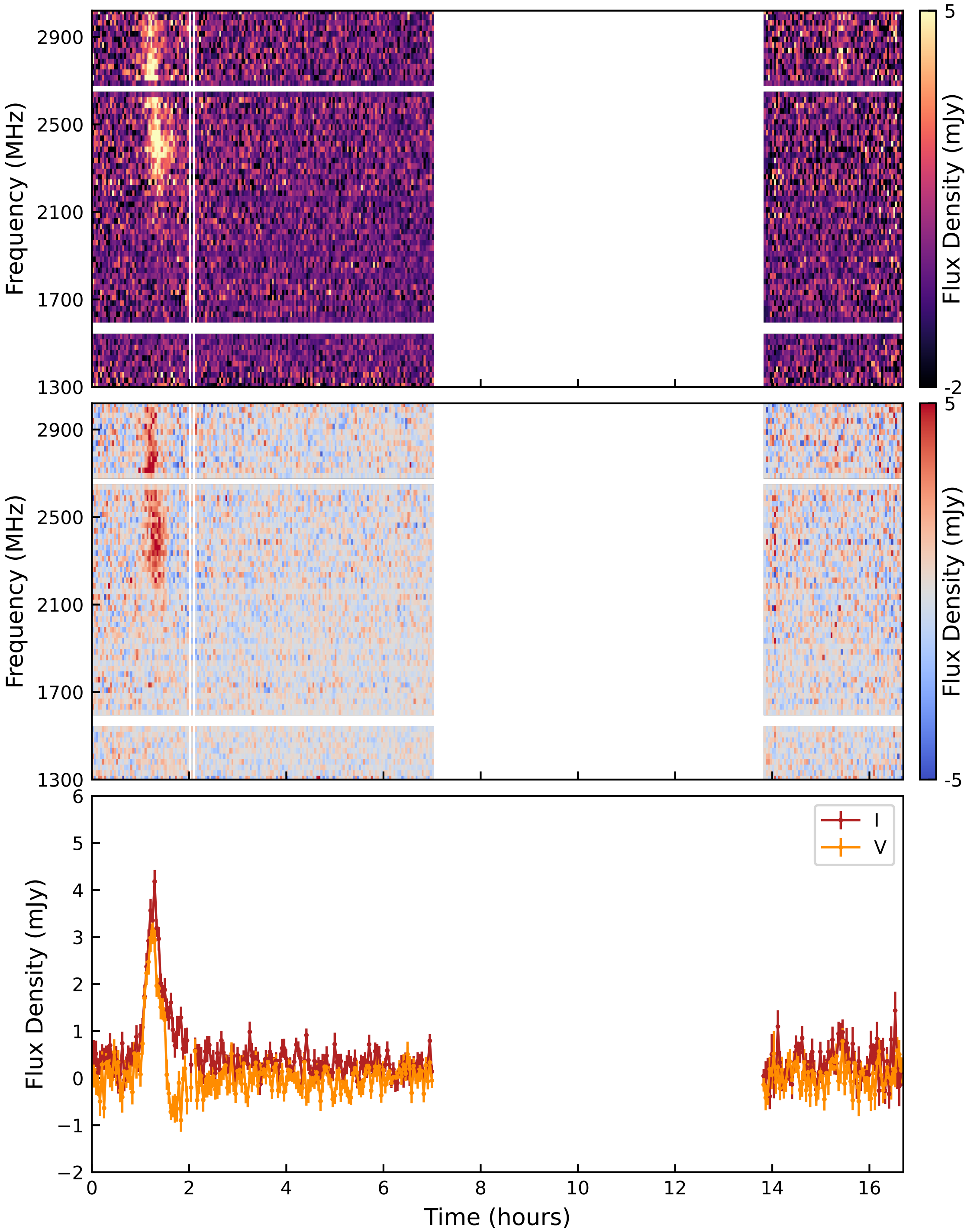

Figure 4.11: Dynamic spectrum of 2100 MHz ATCA observation on 2023–07–23. A 100 % RCP pulse is visible 1 h into the observation with a lower frequency cutoff at 2100 MHz. The visibility lightcurves are formed from averaging the dynamic spectra over the 2100–3000 MHz frequency range. The spike at ∼16 h is caused by residual RFI in a heavily flagged time-sample. Other details are as in Figure 4.3.

by both instruments, suggesting that a new aurorally active region emerged within the five days between ASKAP and ATCA observations. Non-detection of the RCP ASKAP pulse in the ATCA observation is also consistent with the apparent weakening of the pulse profile towards the end of the DWF 2021 observing run, as shown in the bottom panel of Figure 4.2.

We made no pulse detections at C/X-band, which may be explained by a quenching of the emission region in the month between the ATCA L-band detection and C/X-band observations achieving full rotation phase coverage—however, the frequency range of auroral pulses is intrinsically tied to the local magnetic field strength, so pulse activity is not necessarily correlated across large fractional bandwidths (e.g. Lynch et al. 2015). Therefore non-detection of pulses at C/X-band may also be explained by an upper frequency cutoff to auroral emission from SCR J1845−6357 somewhere between the detection at 3000 MHz and non-detection at 4500 MHz. This cutoff represents the coronal depth at which ECMI cannot operate due to increase plasma density driving $\nu_p > \nu_c$, and corresponds to a magnetic field strength of 1–1.6 kG if emission is at ν_c, or 500–800 G if driven at the first harmonic $2\nu_c$.

The majority of detected pulses have durations from 30–120 min, but two pulses on 2022–09–23 and 2023–02–05 occur over a duration of only 2–4 min and reaching a flux density of 20–30 mJy. Zoomed in dynamic spectra of these two pulses are shown in Figure 4.12. The pulses are both left circularly polarised and show evidence of unresolved fine structure with both frequency cutoffs and drifts and distinct sub-pulses. These pulses may be explained by a similar model as presented by Bastian et al. (2022) for the sub-pulse structure in the auroral pulses of UV Cet, in which a range of separate, nearby active field lines sweep the line of sight as a function of time and frequency.

4.6 Conclusions

In two years of monitoring of the ultracool dwarf SCR J1845−6357 with ASKAP and ATCA we have detected magnetospheric radio emission in the form of auroral pulses and persistent, variable quiescent emission. The auroral activity of SCR J1845−6357 demonstrates a variety of phenomenology including pulse repetition at the rotation period of 14.1 h, persistence of pulse profile over weeks-long timescales, extent over a frequency range of 800–3000 MHz with varying maximum and minimum cutoffs between pulse groups, and presence of both 100 % RCP and LCP circular polarisation. Future work to model these features will help to determine the configuration of auroral sources in the stellar corona (e.g. Hess et al. 2008) and constrain the configuration of the global magnetic field. These measurements will be important for the validation of fully convective dynamo models in the regime of slow rotators.

Acknowledgements

JP is supported by the Australian Government Research Training Program Scholarship. Parts of this research were conducted by the Australian Research Council

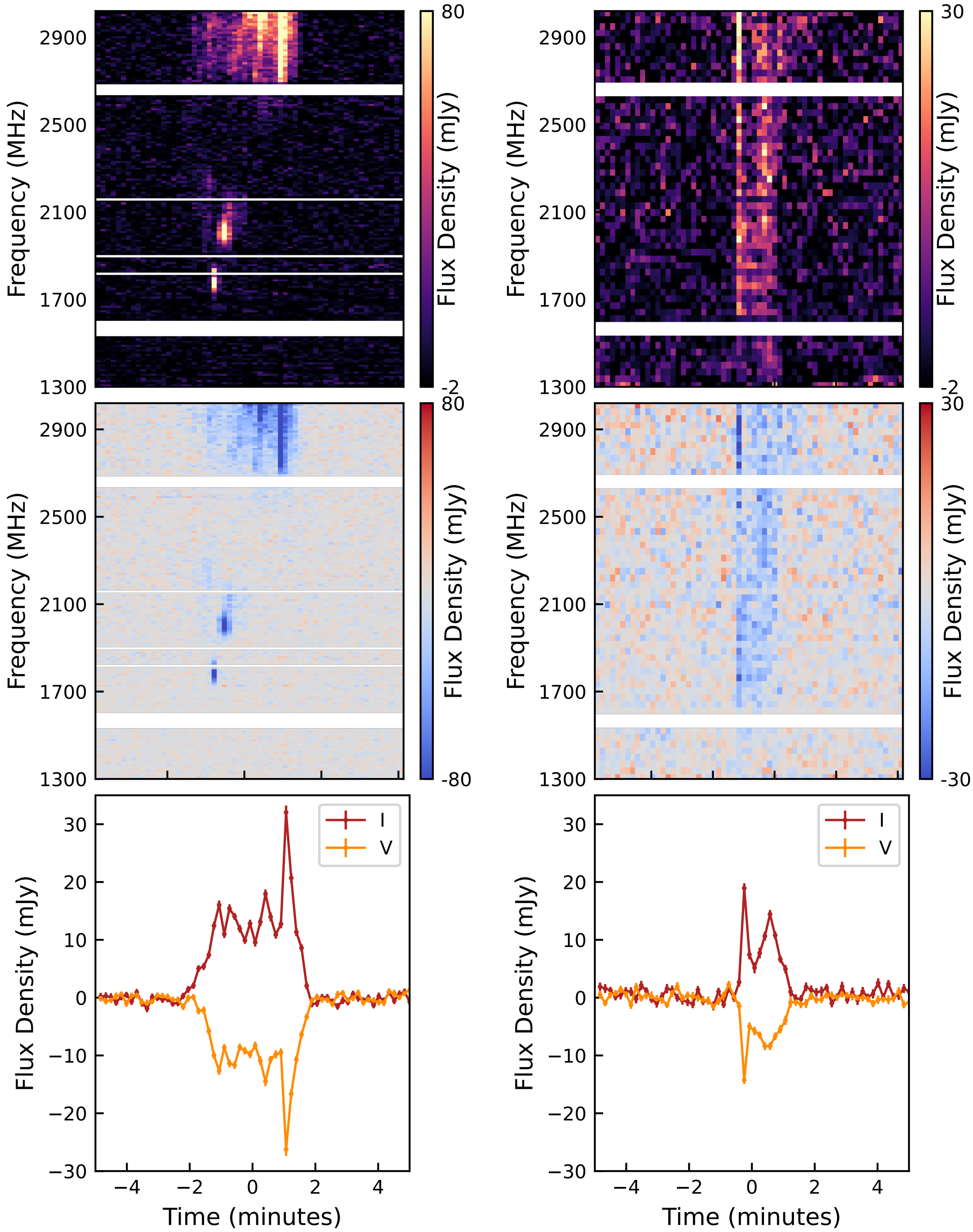

Figure 4.12: Zoomed-in dynamic spectra of short timescale pulses detected with ATCA on 2022–09–23 (left) and 2023–02–05 (right). Data are binned to a frequency resolution 10 MHz and 30 MHz respectively, and have full time resolution of 10 s.

Centre of Excellence for Gravitational Wave Discovery (OzGrav), project number CE170100004. The Australian SKA Pathfinder is part of the Australia Telescope National Facility (grid.421683.a) which is managed by CSIRO. Operation of ASKAP is funded by the Australian Government with support from the National Collaborative Research Infrastructure Strategy. ASKAP uses the resources of the Pawsey Supercomputing Centre. Establishment of ASKAP, the Murchison Radio-astronomy Observatory and the Pawsey Supercomputing Centre are initiatives of the Australian Government, with support from the Government of Western Australia and the Science and Industry Endowment Fund. We acknowledge the Wajarri Yamatji people as the traditional owners of the Observatory site. The Australia Telescope Compact Array is part of the Australia Telescope National Facility (grid.421683.a) which is funded by the Australian Government for operation as a National Facility managed by CSIRO. We acknowledge the Gomeroi people as the traditional owners of the Observatory site. Funding for the TESS mission is provided by NASA's Science Mission directorate. This paper includes data collected by the TESS mission, which are publicly available from the Mikulski Archive for Space Telescopes (MAST). This work has made use of data from the European Space Agency (ESA) mission *Gaia* (`https://www.cosmos.esa.int/gaia`), processed by the *Gaia* Data Processing and Analysis Consortium (DPAC, `https://www.cosmos.esa.int/web/gaia/dpac/consortium`). Funding for the DPAC has been provided by national institutions, in particular the institutions participating in the *Gaia* Multilateral Agreement. This research has made use of the SIMBAD database, operated at CDS, Strasbourg, France. This research has made use of NASA's Astrophysics Data System. This research made use of the following PYTHON packages: ASTROPY (Astropy Collaboration et al. 2013, 2018), a community-developed core Python package for Astronomy, MATPLOTLIB (Hunter 2007), a Python library for publication quality graphics, NUMPY (van der Walt et al. 2011; Harris et al. 2020), and PANDAS (Wes McKinney 2010; McKinney 2011).

Chapter 5

Conclusions and Future Outlook

Throughout the history of radio astronomy, the identification of stellar radio emission has been challenging amidst the extragalactic radio sources that dominate the sky. Targeted surveys of well-known radio loud systems have provided a wealth of insight into the reconnection driven mechanisms responsible for particle energisation in the Sun, and a clearer picture has emerged of the connection between complex auroral current systems observed within the Solar system and their analogue in scaled up stellar environments.

These targeted studies require an unbiased counterpart in order to remain open to new, unexpected discoveries, and to build reliable samples that are large enough to make inference on statistical parameters, including:

- the radio star surface density and expected detection rates in future transient surveys,
- the rate and energy distributions of burst activity,
- the size and fraction of the total population among various classes of radio active stars,
- and the dependence of these statistics on other fundamental stellar parameters.

The current generation of radio telescopes including ASKAP, LOFAR, the MWA, MeerKAT, and the Jansky Very Large Array are capable of reaching sub-mJy sensitivity over timescales of minutes to hours. These telescopes are beginning to conduct large widefield surveys that are ripe for the discovery of new stellar radio transient sources, but also come with significant identification challenges. The ever-increasing surface density of extragalactic radio sources causes naive positional crossmatches between radio and optical surveys to produce an overwhelming number of false-positive matches, and the bright sources of diffuse emission towards the Galactic plane present significant challenges to effective calibration and imaging on the short timescales typical of stellar radio activity. The development of techniques to robustly identify stellar radio activity is therefore important to fully exploit the discovery potential of these new instruments. In this thesis I have explored the use of circular polarisation to unambiguously identify sources of magnetically driven stellar radio emission in the first widefield surveys with ASKAP.

In Chapter 2 I presented the first all-sky survey in circular polarisation at centimetric wavelengths as part of the Rapid ASKAP Continuum Survey at 888 MHz. This project resulted in the detection of 33 radio stars, including 23 that have never been previously identified as radio loud. Some of these stars are atypical radio emitters, including M-dwarfs without any other signs of magnetic activity, and represent a population of radio stars that has been systematically missed by targeted surveys. This sample is the subject of ongoing targeted surveys aimed at testing the existing paradigm of M-dwarf radio activity that has previously been heavily informed by a small number of the most active stars. This work led to the use of circular polarisation searches as a standard technique in transient surveys with ASKAP.

In Chapter 3 I presented an extension of the circular polarisation search technique to the first multi-epoch transient survey with ASKAP at 888 MHz—the Variables and Slow Transients (VAST) pilot survey. This project resulted in the detection of a further 196 detections of a sample of 43 radio stars in 15 epochs covering a 5131 deg^2 survey footprint. Through repeat sampling of the survey footprint I constrained the typical duty cycle of coherent M-dwarf stellar radio bursts to less than 10 %, and provided a statistical framework for estimating the fraction of the M-dwarf population that produce coherent bursts, placing a lower limit of 10 ± 3 % with currently available data. Future epochs of the full VAST survey—now underway—will allow continued refinement of this limit and extension to other rarer source classes.

In Chapter 4 I presented the discovery of auroral radio pulses from the ultracool dwarf SCR J1845−6357 in a circular polarisation search of the Deeper Wider Faster 2021 observing run. This object is both the oldest (1.8–3.1 Gyr) and the slowest rotating (14.1 h) ultracool dwarf yet observed to produce auroral radio pulses, and highlights the discovery potential of circular polarisation searches in widefield surveys. In this project I conducted a followup monitoring campaign of SCR J1845−6357 over two years with ASKAP and the Australia Telescope Compact Array, and presented dynamic spectra capturing a diverse variety of auroral radio activity. This project is ongoing, and future work will be aimed at modelling the auroral emission to constrain the auroral source configuration and evolution of magnetic activity over the duration of the survey. These insights will be valuable in constraining the dynamo mechanisms capable of producing strong magnetic fields in such an old and slowly rotating fully convective star.

Circular polarisation searches are a valuable tool for both the identification of large statistical radio star samples and the discovery of rare objects for followup, targeted study. Coherent M-dwarf radio bursts represent the largest source class identified in the work presented in this thesis, and these detections are likely driven by the ECMI emission mechanism which operates at a frequency directly proportional to the local magnetic field strength. Circular polarisation searches of future widefield radio surveys spanning multiple spectral bands will therefore form an excellent statistical probe of M-dwarf magnetism, providing measurements of the distribution of magnetic field strength and its correlation to other parameters associated with stellar magnetic activity. Through the cumulative detection rates in the work of Chapter 2 and Chapter 3 I have provided an estimate of the radio star detection yield in next-generation surveys with the Square Kilometre Array, which should detect tens of thousands of stars in single epoch surveys of the radio sky. In addition to the stellar radio science that circular polarisation searches will afford in these surveys, searches for rarer, extragalactic radio transients will be aided through an effective filter to remove the foreground fog of variable radio stars.

Circular polarisation searches of future widefield surveys will also identify large samples of radio loud stars that can be studied in followup observations using instruments with improved instantaneous sensitivity, wider bandwidth, and finer temporal and spectral resolution—such as the Australia Telescope Compact Array (ATCA) and MeerKAT. These observations will be important to help answer some of the key questions that remain open surrounding the nature of magnetically driven stellar radio emission. Some of these questions include:

What are the emission mechanisms driving coherent stellar radio bursts? Plasma emission and the ECMI are the two coherent emission mechanisms known to operate in stellar and planetary atmospheres, with plasma emission dominating in weak magnetic environments where the electron cyclotron frequency drops below the plasma frequency and the ECMI dominating in more strongly magnetised, low density plasmas. In the Solar system plasma emission is responsible for the majority of Solar radio bursts while ECMI drives auroral radio emission from the magnetised planets and moons. However, radio studies of the more strongly magnetised atmospheres of M-dwarfs have previously revealed the presence of ECMI in both auroral type emission (Lynch et al. 2017b; Zic et al. 2019b; Bastian et al. 2022) and a Solar type IV burst (Zic et al. 2020), and recent Solar radio studies have detected auroral activity in an isolated coronal active region (Yu et al. 2023). These results suggest a breakdown in the Solar type vs planetary auroral emission dichotomy—and followup studies of large unbiased samples of coherently emitting radio stars will allow a more generalised understanding of how plasma emission and ECMI operate in stars with plasma properties distinct from the Sun.

How is the emission excited by macrophysical plasma dynamics? Solar system studies have allowed detailed exploration of the connection between microphysical emission processes and the plasma macrophysics that drive them. Solar radio bursts have been classified into five main types based upon their morphology in dynamic spectra, allowing the underlying emission mechanism to be identified and tied to plasma dynamics—such as the formation of shocks and acceleration of electron beams. However, this classification system is already incomplete as a description of the full range of Solar burst phenomena (e.g. Maxwell & Swarup 1958), and it is presently unclear how the plasma processes driving plasma emission and ECMI operate in stellar radio bursts produced in regimes of stronger magnetism than the Sun. Followup observations of such systems with wide spectral bandwidth and fine spectral and temporal resolution will aid modelling of stellar magnetospheres and identification of novel plasma processes unobserved in the Solar system, and the large samples produced by widefield circular polarisation searches will facilitate a more comprehensive classification system of stellar radio bursts.

How are linear and elliptical polarisation produced in stellar radio bursts? While coherent stellar radio emission is typically circularly polarised, recent studies have revealed the presence of elliptical polarisation in auroral radio pulses produced by the flare star UV Cet (Lynch et al. 2017b; Zic et al. 2019b; Bastian et al. 2022). This phenomenon is typically only seen in Jovian decametric bursts (e.g. Lecacheux et al. 1991), where extremely low-density plasma cavities are required to preserve the linear polarisation. Widefield circular polarisation searches will provide an opportunity to identify more elliptically polarised bursts, and followup studies with sensitive, wideband instruments will allow tracing of the origin and evolution of the polarised emission. Application of standard linear polarisation processing techniques to these bursts such as rotation measure (RM) synthesis (Burn 1966; Brentjens & de Bruyn 2005; Heald 2009) may provide a means to constrain the magnetospheric properties of stellar atmospheres harbouring elliptically polarised bursts, in addition to the field strength and polarity constraints already provided by circular polarisation.

How are stellar radio bursts correlated with multi-wavelength activity? Simultaneous studies with radio, optical, infra-red, X-ray, and gamma ray facilities are necessary to build a more comprehensive picture of the plasma processes at work in magnetically active stars. Stellar radio bursts are often observed in isolation to activity at other wavelengths (e.g. Kundu et al. 1988; Pope et al. 2021; Rigney et al. 2022), though without more simultaneous, high-cadence multi-wavelength observations it is difficult to assess whether some of these events are in fact correlated with a time delay. Recent work also indicates periodic gamma ray emission may be produced by auroral processes in active ultracool dwarf atmospheres, with radio and gamma ray emissions tracing the evolution of accelerated electrons and ions respectively (Song & Paglione 2020). This band has been relatively unexplored for stellar radio bursts, and correlation between the high energy emission with periodic radio signals will be important inputs to models of the particle acceleration mechanism and partition of energy into electromagnetic bands.

Star-planet interaction as a probe of exoplanetary magnetism. A scaled up version of the electrodynamic interaction between Jupiter and Io is a phenomenon highly anticipated to occur in strongly magnetised stars and close-in exoplanets (Zarka et al. 2001). This star-planet interaction (SPI) is expected to be driven by the ECMI emission mechanism producing auroral pulses within the magnetic flux tube coupling the star and satellite, and could provide a means for direct radio detection of exoplanets and form a probe of exoplanetary magnetospheres. Two barriers are currently preventing the robust claim of this phenomenon:

1. the emission is expected to be weak and hence high instantaneous sensitivity is required to detect pulses,

2. and auroral pulses periodic with stellar rotation are also commonly generated by the breakdown of co-rotation rather than interaction with a satellite.

Widefield circular polarisation searches will be an important method to identify prospective SPI systems due to the high degrees of circular polarisation in ECMI pulses. Hot-Jupiter exoplanets are a promising candidate class for SPI due to the combination of large size and close-in orbital distance, which should intercept a relatively higher flux of plasma and produce a higher auroral radio power compared to smaller, more distant satellites (Lynch et al. 2017a). These searches should be conducted across a wide range of frequency bands to probe both weakly and strongly magnetised exoplanets, as well as the higher frequency emission that may be produced in the stronger magnetic fields of the host stars (Turnpenney et al. 2018, 2020). Robust identification of SPI will require novel methods to distinguish between satellite induced activity and co-rotation breakdown driven emission modulated at the stellar rotation period. The period of interest is likely to be longer than available observation windows which are limited in duration by source elevation for non-circumpolar stars, requiring statistical correlation of pulses detected in separate observations to establish periodicity. All-sky monitoring with a Lunar based radio telescope presents a plausible solution to this, with the slower $\sim$27 d Lunar rotation period allowing longer contiguous coverage of a wide field of view.

Widefield surveys with the current and next generation of radio telescopes will detect an abundance of radio transients. Continued development of novel search techniques will be necessary to fully realise the discovery potential of these facilities, and to adapt to the dynamic science objectives they aim to address as new classes of radio transient are discovered. This thesis has detailed the role of circular polarisation in overcoming the technical challenge of identifying rare stellar radio bursts among the background of extragalactic radio sources, and the insights circular polarisation provides as a remote sensor of stellar magnetospheric plasma properties. Application of these techniques to next-generation surveys will dramatically improve our understanding of stellar magnetism and plasma dynamics in novel regimes that are not observed in Solar system environments.

Appendix A

Stellar Variable Terminology

Variable stars are often classified based on the morphology of their optical lightcurves, presence of spectral lines in emission or absorption, or some other physical property related to variability such as starspot coverage or orbital configuration. Table A.1 defines some of the terminology used in this thesis to describe such systems.

Table A.1: Definition of variable star terminology used in this thesis.

Variable Type	Definition
Ap / Bp	A- or B- type star with chemical peculiarities.
ApSi	A-type chemically peculiar star with strong Silicon emission lines.
α^2 CVn	Chemically peculiar A- or B- or A-type stars with optical variability caused by an uneven surface distribution of metals. These stars feature strong magnetic fields that separate and trap chemical peculiarities at the surface. α^2 Canum Venaticorum is the prototype of this variable class.
BY Dra	Star that demonstrate optical variability caused by an uneven distribution of starspots modulated by stellar rotation. BY Draconis is the prototype of this variable class.
EA2 Algol	Eclipsing variables in which the component stars are semi-attached, with one star filling its Roche lobe. Algol is the prototype of this variable class
RS CVn	Close detached binary systems with strong Ca II H and K line emission. RS Canum Venaticorum is the prototype of this variable class.

Bibliography

Aarnio A. N., Matt S. P., Stassun K. G., 2012, ApJ, 760, 9

Abada-Simon M., Aubier M., 1997, A&AS, 125, 511

Abbuhl E., Mutel R. L., Lynch C., Güedel M., 2015, ApJ, 811, 33

Ackley K., et al., 2020, PASA, 37, e047

Adelman-McCarthy J. K., et al., 2008, ApJS, 175, 297

Ainsworth R. E., Scaife A. M. M., Ray T. P., Taylor A. M., Green D. A., Buckle J. V., 2014, ApJ, 792, L18

Alvarado-Gómez J. D., et al., 2020, ApJ, 895, 47

Andrae R., et al., 2018, A&A, 616, A8

Andre P., 1996, in Taylor A. R., Paredes J. M., eds, ASP Conference Series Vol. 93, Radio Emission from the Stars and the Sun. pp 273–284

Andre P., Montmerle T., Feigelson E. D., 1987, AJ, 93, 1182

Andre P., Montmerle T., Feigelson E. D., Stine P. C., Klein K.-L., 1988, ApJ, 335, 940

Andre P., Phillips R. B., Lestrade J.-F., Klein K.-L., 1991, ApJ, 376, 630

Andreoni I., Cooke J., 2019, in Griffin R. E., ed., , Vol. 339, Southern Horizons in Time-Domain Astronomy. Southern Horizons in Time-Domain Astronomy, pp 135–138 (arXiv:1802.01100), doi:10.1017/S1743921318002399

Ansdell M., et al., 2015, ApJ, 798, 41

Antonova A., Hallinan G., Doyle J. G., Yu S., Kuznetsov A., Metodieva Y., Golden A., Cruz K. L., 2013, A&A, 549, A131

Anumarlapudi A., et al., 2023, ApJ, 956, 28

Appleton E. V., 1932, Institution of Electrical Engineers-Proceedings of the Wireless Section of the Institution, 7, 257

Aschwanden M. J., 1995, in Benz A. O., Krüger A., eds, , Vol. 444, Coronal Magnetic Energy Releases. Coronal Magnetic Energy Releases, p. 13, doi:10.1007/3-540-59109-5_40

Astropy Collaboration et al., 2013, A&A, 558, A33

Astropy Collaboration et al., 2018, AJ, 156, 123

Ball B., Drake J. J., Lin L., Kashyap V., Laming J. M., García-Alvarez D., 2005, ApJ, 634, 1336

Bastian T. S., Dulk G. A., Leblanc Y., 2000, ApJ, 545, 1058

Bastian T. S., Cotton W. D., Hallinan G., 2022, ApJ, 935, 99

Becker R. H., White R. L., Helfand D. J., 1995, ApJ, 450, 559

Beitia-Antero L., Gómez de Castro A. I., 2016, A&A, 596, A49

Benz A. O., Güdel M., 1994, A&A, 285, 621

Benz A. O., Wentzel D. G., 1981, A&A, 94, 100

Benz A. O., Magun A., Stehling W., Su H., 1992, Sol. Phys., 141, 335

Benz A. O., Monstein C., Meyer H., 2005, Sol. Phys., 226, 143

Benz A. O., et al., 2009a, Earth Moon and Planets, 104, 277

Benz A. O., Monstein C., Beverland M., Meyer H., Stuber B., 2009b, Sol. Phys., 260, 375

Berdyugina S. V., Tuominen I., 1998, A&A, 336, L25

Berger E., 2002, ApJ, 572, 503

Berger E., 2006, ApJ, 648, 629

Berger E., et al., 2001, Nature, 410, 338

Berger E., et al., 2005, ApJ, 627, 960

Berger E., et al., 2009, ApJ, 695, 310

Berger E., et al., 2010, ApJ, 709, 332

Bhunia S., Carley E. P., Oberoi D., Gallagher P. T., 2023, A&A, 670, A169

Bieging J. H., Abbott D. C., Churchwell E. B., 1989, ApJ, 340, 518

Boller T., Freyberg M. J., Trümper J., Haberl F., Voges W., Nandra K., 2016, A&A, 588, A103

Bolton J. G., Stanley G. J., 1949, Australian Journal of Scientific Research A Physical Sciences, 2, 139

Bolton S. J., et al., 2002, Nature, 415, 987

Boro Saikia S., et al., 2018, A&A, 616, A108

Borovsky J. E., Valdivia J. A., 2018, Surveys in Geophysics, 39, 817

Borovsky J. E., Thomsen M. F., Elphic R. C., 1998, J. Geophys. Res., 103, 17617

Bower G. C., Bolatto A., Ford E. B., Kalas P., 2009, ApJ, 701, 1922

Bowman J. D., et al., 2013, PASA, 30, e031

Brandenburg A., Subramanian K., 2005, Phys. Rep., 417, 1

Braun R., Bonaldi A., Bourke T., Keane E., Wagg J., 2019, arXiv e-prints, p. arXiv:1912.12699

Brentjens M. A., de Bruyn A. G., 2005, A&A, 441, 1217

Briggs D. S., 1995, PhD thesis, New Mexico Institute of Mining and Technology

Briquet M., Aerts C., Lüftinger T., De Cat P., Piskunov N. E., Scuflaire R., 2004, A&A, 413, 273

Browning M. K., 2008, ApJ, 676, 1262

Budding E., Marsden S. C., Slee B., 2001, PASA, 18, 140

Burgasser A. J., Putman M. E., 2005, ApJ, 626, 486

Burn B. J., 1966, MNRAS, 133, 67

Burrows A., et al., 1997, ApJ, 491, 856

Cairns I. H., Robinson R. D., 1987, Sol. Phys., 111, 365

Cairns I. H., Knock S. A., Robinson P. A., Kuncic Z., 2003, Space Sci. Rev., 107, 27

Callingham J. R., et al., 2021a, Nature Astronomy, 5, 1233

Callingham J. R., et al., 2021b, A&A, 648, A13

Callingham J. R., et al., 2023, A&A, 670, A124

Chabrier G., Küker M., 2006, A&A, 446, 1027

Chambers K. C., et al., 2016, arXiv e-prints, p. arXiv:1612.05560

Chapman J. M., Dempsey J., Miller D., Heywood I., Pritchard J., Sangster E., Whiting M., Dart M., 2017, in Lorente N. P. F., Shortridge K., Wayth R., eds, Astronomical Society of the Pacific Conference Series Vol. 512, Astronomical Data Analysis Software and Systems XXV. p. 73

Chiuderi Drago F., Klein K. L., 1990, Ap&SS, 170, 81

Christensen U. R., 2010, Space Sci. Rev., 152, 565

Chu K. R., 2004, Reviews of Modern Physics, 76, 489

Cincunegui C., Díaz R. F., Mauas P. J. D., 2007, A&A, 469, 309

Claßen H. T., Aurass H., 2002, A&A, 384, 1098

Climent J. B., Guirado J. C., Pérez-Torres M., Marcaide J. M., Peña-Moñino L., 2023, Science, 381, 1120

Cliver E. W., White S. M., Balasubramaniam K. S., 2011, ApJ, 743, 145

Collier A. C., Haynes R. F., Slee O. B., Wright A. E., Hillier D. J., 1982, MNRAS, 200, 869

Condon J. J., 1997, PASP, 109, 166

Condon J. J., Cotton W. D., Greisen E. W., Yin Q. F., Perley R. A., Taylor G. B., Broderick J. J., 1998, AJ, 115, 1693

Cornwell T., Humphreys B., Lenc E., Voronkov M., Whiting M., 2011, Technical report, ATNF ASKAP memorandum 27: ASKAP Science Processing, https://www.atnf.csiro.au/projects/askap/ASKAP-SW-0020.pdf. CSIRO, https://www.atnf.csiro.au/projects/askap/ASKAP-SW-0020.pdf

Cowley S. W. H., Bunce E. J., 2001, Planet. Space Sci., 49, 1067

Cowley S. W. H., Bunce E. J., 2003, Annales Geophysicae, 21, 1691

Crosley M. K., Osten R. A., 2018a, ApJ, 856, 39

Crosley M. K., Osten R. A., 2018b, ApJ, 862, 113

Crosley M. K., et al., 2016, ApJ, 830, 24

Cruz K. L., Reid I. N., 2002, AJ, 123, 2828

Da Costa G. S., et al., 2019, MNRAS, 489, 5900

Dai S., et al., 2019, ApJ, 874, L14

Das B., et al., 2022, ApJ, 925, 125

Davis R. J., Lovell B., Palmer H. P., Spencer R. E., 1978, Nature, 273, 644

Davis I., Vedantham H. K., Callingham J. R., Shimwell T. W., Vidotto A. A., Zarka P., Ray T. P., Drabent A., 2021, A&A, 650, L20

Del Zanna G., Aulanier G., Klein K. L., Török T., 2011, A&A, 526, A137

Desch M. D., Rucker H. O., 1983, J. Geophys. Res., 88, 8999

Dobie D., et al., 2019, ApJ, 887, L13

Dobie D., et al., 2022, MNRAS, 510, 3794

Dobie D., et al., 2023, MNRAS, 519, 4684

Dobler W., Stix M., Brandenburg A., 2006, ApJ, 638, 336

Dougherty S., Taylor A., Waters L., 1991, A&A, 248, 175

Drake S. A., Simon T., Linsky J. L., 1986, AJ, 91, 1229

Drake S. A., Simon T., Linsky J. L., 1989, ApJS, 71, 905

Drake S. A., Simon T., Linsky J. L., 1992, ApJS, 82, 311

Drake S. A., Simon T., Brown A., 1993, ApJ, 406, 247

Driessen L. N., Heald G., Duchesne S. W., Murphy T., Lenc E., Leung J. K., Moss V. A., 2023, PASA, 40, e036

Duchesne S. W., et al., 2023, PASA, 40, e034

Duchesne S. W., et al., 2024, PASA, 41, e003

Dulk G. A., 1985, ARA&A, 23, 169

Dulk G. A., Marsh K. A., 1982, ApJ, 259, 350

Dulk G. A., Suzuki S., Sheridan K. V., 1984, A&A, 130, 39

Dungey J. W., 1961, Phys. Rev. Lett., 6, 47

Durney B. R., De Young D. S., Roxburgh I. W., 1993, Sol. Phys., 145, 207

Elgarøy E. Ø., 1977, Solar noise storms. Elsevier, doi:10.1016/C2013-0-05754-4

Ergun R. E., et al., 2004, Journal of Geophysical Research (Space Physics), 109, A12220

Evans D. S., Moore T. E., 1979, J. Geophys. Res., 84, 6451

Falgarone E., Gilmore W., 1981, A&A, 95, 32

Fey A. L., et al., 2015, AJ, 150, 58

Florkowski D. R., Johnston K. J., Wade C. M., de Vegt C., 1985, AJ, 90, 2381

Frith J., et al., 2013, MNRAS, 435, 2161

Fuhrmeister B., Schmitt J. H. M. M., 2003, A&A, 403, 247

Gaia Collaboration et al., 2018, A&A, 616, A1

Gaia Collaboration et al., 2023, A&A, 674, A1

Gary D. E., 2023, ARA&A, 61, 427

Gelfreikh G. B., 2004, in Gary D. E., Keller C. U., eds, Astrophysics and Space Science Library Vol. 314, Astrophysics and Space Science Library. p. 115, doi:10.1007/1-4020-2814-8_6

Ginzburg V. L., Syrovatskii S. I., 1965, ARA&A, 3, 297

Ginzburg V. L., Zhelezniakov V. V., 1958, Soviet Ast., 2, 653

Golay W. W., Mutel R. L., Lipman D., Güdel M., 2023, MNRAS, 522, 1394

Golovin A., Reffert S., Just A., Jordan S., Vani A., Jahreiß H., 2023, A&A, 670, A19

Gopalswamy N., 2006, Geophysical Monograph Series, 165, 207

Graffagnino V. G., Wonnacott D., Schaeidt S., 1995, MNRAS, 275, 129

Griffin R., 1998, The Observatory, 118, 273

Grodent D., et al., 2018, Journal of Geophysical Research (Space Physics), 123, 3299

Grunhut J. H., et al., 2012, MNRAS, 419, 1610

Güdel M., 1992, A&A, 264, L31

Güdel M., 2002, ARA&A, 40, 217

Güdel M., Benz A. O., 1993, ApJ, 405, L63

Güdel M., Schmitt J. H. M. M., Bookbinder J. A., Fleming T. A., 1993, ApJ, 415, 236

Gulati A., et al., 2023, PASA, 40, e025

Gurzadyan G. A., Terzian Y., 1980, Flare stars. Pergamon Press

Guzman J., et al., 2019, ASKAPsoft: ASKAP science data processor software, Astrophysics Source Code Library, record ascl:1912.003, doi:10.25919/5cca3787a6353

Haakonsen C. B., Rutledge R. E., 2009, ApJS, 184, 138

Hajduk M., Leto P., Vedantham H., Trigilio C., Haverkorn M., Shimwell T., Callingham J. R., White G. J., 2022, A&A, 665, A152

Hale C. L., et al., 2021, PASA, 38, e058

Hallinan G., Antonova A., Doyle J. G., Bourke S., Brisken W. F., Golden A., 2006, ApJ, 653, 690

Hallinan G., et al., 2007, ApJ, 663, L25

Hallinan G., Antonova A., Doyle J. G., Bourke S., Lane C., Golden A., 2008, ApJ, 684, 644

Hallinan G., et al., 2015, Nature, 523, 568

Hambaryan V., Neuhäuser R., Stelzer B., 1999, A&A, 345, 121

Han J. L., Manchester R. N., Xu R. X., Qiao G. J., 1998, MNRAS, 300, 373

Harris C. R., et al., 2020, Nature, 585, 357

Hartree D. R., 1931, Proceedings of the Cambridge Philosophical Society, 27, 143

Hawley S. L., Gizis J. E., Reid I. N., 1996, AJ, 112, 2799

Heald G., 2009, in Strassmeier K. G., Kosovichev A. G., Beckman J. E., eds, Vol. 259, Cosmic Magnetic Fields: From Planets, to Stars and Galaxies. pp 591–602, doi:10.1017/S1743921309031421

Helfand D. J., Schnee S., Becker R. H., White R. L., McMahon R. G., 1999, AJ, 117, 1568

Hess S. L. G., Zarka P., 2011, A&A, 531, A29

Hess S., Cecconi B., Zarka P., 2008, Geophys. Res. Lett., 35, L13107

Hey J. S., 1946, Nature, 157, 47

Hey J. S., Parsons S. J., Phillips J. W., 1946, Nature, 158, 234

Hill T. W., 1979, J. Geophys. Res., 84, 6554

Hill T. W., 2001, J. Geophys. Res., 106, 8101

Hotan A. W., et al., 2014, PASA, 31, e041

Hotan A. W., et al., 2021, PASA, 38, e009

Hunter J. D., 2007, Computing in Science and Engineering, 9, 90

Hurley-Walker N., et al., 2017, MNRAS, 464, 1146

Hyman S. D., et al., 2021, MNRAS, 507, 3888

Ighina L., et al., 2022, A&A, 663, A73

Intema H. T., Jagannathan P., Mooley K. P., Frail D. A., 2017, A&A, 598, A78

Isaacson H., Fischer D., 2010, ApJ, 725, 875

Jackson J. D., 1999, Classical Electrodynamics, 3rd Edition. John Wiley & Sons

Jackson P. D., Kundu M. R., White S. M., 1987, in Linsky J. L., Stencel R. E., eds, , Vol. 291, Cool Stars, Stellar Systems and the Sun. Springer Berlin Heidelberg, pp 103–105, doi:10.1007/3-540-18653-0_116

Jansky K. G., 1933, Nature, 132, 66

Jao W.-C., Henry T. J., Gies D. R., Hambly N. C., 2018, ApJ, 861, L11

Jeffers S. V., et al., 2018, A&A, 614, A76

Johnston S., Kerr M., 2018, MNRAS, 474, 4629

Johnston S., et al., 2008, Experimental Astronomy, 22, 151

Jones D. O., West A. A., 2016, ApJ, 817, 1

Jones K. L., Stewart R. T., Nelson G. J., Duncan A. R., 1994, MNRAS, 269, 1145

Kao M. M., Hallinan G., Pineda J. S., Escala I., Burgasser A., Bourke S., Stevenson D., 2016, ApJ, 818, 24

Kao M. M., Hallinan G., Pineda J. S., Stevenson D., Burgasser A., 2018, ApJS, 237, 25

Kao M. M., Mioduszewski A. J., Villadsen J., Shkolnik E. L., 2023, Nature, pp 1–3

Kaplan D. L., et al., 2019, ApJ, 884, 96

Karataş Y., Bilir S., Eker Z., Demircan O., 2004, MNRAS, 349, 1069

Kashyap V., Drake J. J., 1999, ApJ, 524, 988

Kasper M., Biller B. A., Burrows A., Brandner W., Budaj J., Close L. M., 2007, A&A, 471, 655

Kavanagh R. D., Vedantham H. K., 2023, MNRAS, 524, 6267

Kavanagh R. D., Vidotto A. A., Klein B., Jardine M. M., Donati J.-F., Ó Fionnagáin D., 2021, MNRAS, 504, 1511

Kellermann K. I., Pauliny-Toth I. I. K., 1969, ApJ, 155, L71

Kellett B. J., Bingham R., Cairns R. A., Tsikoudi V., 2002, MNRAS, 329, 102

Kimball A. E., Knapp G. R., Ivezić Ž., West A. A., Bochanski J. J., Plotkin R. M., Gordon M. S., 2009, ApJ, 701, 535

Kiraga M., 2012, Acta Astron., 62, 67

Klassen A., Karlický M., Mann G., 2003, A&A, 410, 307

Klein K. L., Chiuderi-Drago F., 1987, A&A, 175, 179

Kochukhov O., 2021, A&A Rev., 29, 1

Kochukhov O., Bagnulo S., 2006, A&A, 450, 763

Koen C., Miszalski B., Väisänen P., Koen T., 2017, MNRAS, 465, 4723

Komesaroff M., 1958, Australian Journal of Physics, 11, 201

Kontar E. P., et al., 2017, Nature Communications, 8, 1515

Kontogeorgos A., et al., 2006, Experimental Astronomy, 21, 41

Kowalski A. F., Hawley S. L., Holtzman J. A., Wisniewski J. P., Hilton E. J., 2010, ApJ, 714, L98

Kramer M., Stappers B. W., Jessner A., Lyne A. G., Jordan C. A., 2007, MNRAS, 377, 107

Krupar V., et al., 2018, ApJ, 857, 82

Kundu M. R., Pallavicini R., White S. M., Jackson P. D., 1988, A&A, 195, 159

Kundu M. R., Raulin J. P., Nitta N., Hudson H. S., Shimojo M., Shibata K., Raoult A., 1995, ApJ, 447, L135

Kurth W. S., et al., 2017, Geophys. Res. Lett., 44, 7114

Lacy C. H., Evans D. S., Quigley R. J., Sandmann W. H., 1978, ApJS, 37, 313

Lacy M., et al., 2020, PASP, 132, 035001

Lecacheux A., Boischot A., Boudjada M. Y., Dulk G. A., 1991, A&A, 251, 339

Lenc E., et al., 2017, PASA, 34, e040

Lenc E., Murphy T., Lynch C. R., Kaplan D. L., Zhang S. N., 2018, MNRAS, 478, 2835

Lépine S., Gaidos E., 2011, AJ, 142, 138

Leto P., Trigilio C., Buemi C. S., Umana G., Leone F., 2006, A&A, 458, 831

Leto P., Trigilio C., Buemi C. S., Umana G., Ingallinera A., Cerrigone L., 2017, MNRAS, 469, 1949

Leto P., et al., 2018, MNRAS, 476, 562

Leung J. K., et al., 2021, MNRAS, 503, 1847

Li W., Hudson M. K., 2019, Journal of Geophysical Research (Space Physics), 124, 8319

Li C. Y., Chen Y., Wang B., Ruan G. P., Feng S. W., Du G. H., Kong X. L., 2017, Sol. Phys., 292, 82

Linsky J. L., Drake S. A., Bastian T. S., 1992, ApJ, 393, 341

Lo K. K., et al., 2012, MNRAS, 421, 3316

Lomb N. R., 1976, Ap&SS, 39, 447

Lorimer D. R., Kramer M., 2004, Handbook of pulsar astronomy. Vol. 4, Cambridge University Press

Louarn P., et al., 2017, Geophys. Res. Lett., 44, 4439

Louis C. K., et al., 2017, Geophys. Res. Lett., 44, 9225

Louis C. K., et al., 2023, Journal of Geophysical Research (Space Physics), 128, e2023JA031985

Lovell A. C. B., 1964a, The Observatory, 84, 191

Lovell A. C. B., 1964b, Nature, 201, 1013

Loyd R. O. P., Shkolnik E. L., Schneider A. C., Barman T. S., Meadows V. S., Pagano I., Peacock S., 2018, ApJ, 867, 70

Lynch C., Mutel R. L., Güdel M., 2015, ApJ, 802, 106

Lynch C., Murphy T., Ravi V., Hobbs G., Lo K., Ward C., 2016, MNRAS, 457, 1224

Lynch C. R., Murphy T., Kaplan D. L., Ireland M., Bell M. E., 2017a, MNRAS, 467, 3447

Lynch C. R., Lenc E., Kaplan D. L., Murphy T., Anderson G. E., 2017b, ApJ, 836, L30

Macquart J.-P., 2002, PASA, 19, 43

Mandrini C. H., et al., 2015, ApJ, 809, 73

Matthews L. D., 2019, PASP, 131, 016001

Mauch T., Murphy T., Buttery H. J., Curran J., Hunstead R. W., Piestrzynski B., Robertson J. G., Sadler E. M., 2003, MNRAS, 342, 1117

Mauk B. H., Saur J., 2007, Journal of Geophysical Research (Space Physics), 112, A10221

Maxwell A., Swarup G., 1958, Nature, 181, 36

McCauley P. I., Cairns I. H., White S. M., Mondal S., Lenc E., Morgan J., Oberoi D., 2019, Sol. Phys., 294, 106

McClure M. K., et al., 2008, ApJ, 683, L187

McConnell D., et al., 2016, PASA, 33, e042

McConnell D., et al., 2020, PASA, 37, e048

McCready L. L., Pawsey J. L., Payne-Scott R., 1947, Proceedings of the Royal Society of London Series A, 190, 357

McKinney W., 2011, Python for High Performance and Scientific Computing, 14

McLean M., Berger E., Reiners A., 2012, ApJ, 746, 23

Melrose D. B., 1971, Ap&SS, 12, 172

Melrose D. B., 1980, Sol. Phys., 67, 357

Melrose D. B., 1986, Instabilities in Space and Laboratory Plasmas. Cambridge University Press, doi:10.1017/CBO9780511564123

Melrose D. B., 1987, Sol. Phys., 111, 89

Melrose D. B., 1991, ARA&A, 29, 31

Melrose D. B., 2006, ApJ, 637, 1113

Melrose D. B., 2009, in Gopalswamy N., Webb D. F., eds, Vol. 257, Universal Heliophysical Processes. pp 305–315, doi:10.1017/S1743921309029470

Melrose D. B., 2017, Reviews of Modern Plasma Physics, 1, 5

Melrose D. B., Dulk G. A., 1982, ApJ, 259, 844

Melrose D. B., Wheatland M. S., 2016, Sol. Phys., 291, 3637

Menietti J. D., Gurnett D. A., Christopher I., 2001, Geophys. Res. Lett., 28, 3047

Mercier C., Subramanian P., Chambe G., Janardhan P., 2015, A&A, 576, A136

Messina S., Desidera S., Turatto M., Lanzafame A. C., Guinan E. F., 2010, A&A, 520, A15

Miles B. E., Shkolnik E. L., 2017, AJ, 154, 67

Mohanty S., Basri G., Shu F., Allard F., Chabrier G., 2002, ApJ, 571, 469

Mondrik N., Newton E., Charbonneau D., Irwin J., 2019, ApJ, 870, 10

Morin J., Donati J. F., Petit P., Delfosse X., Forveille T., Jardine M. M., 2010, MNRAS, 407, 2269

Morosan D. E., Kilpua E. K. J., Carley E. P., Monstein C., 2019, A&A, 623, A63

Morosan D. E., Pomoell J., Kumari A., Kilpua E. K. J., Vainio R., 2023, A&A, 675, A98

Morris D. H., Mutel R. L., 1988, AJ, 95, 204

Morrissey P., et al., 2007, ApJS, 173, 682

Mullan D. J., Paudel R. R., 2019, ApJ, 873, 1

Murphy T., Mauch T., Green A., Hunstead R. W., Piestrzynska B., Kels A. P., Sztajer P., 2007, MNRAS, 382, 382

Murphy T., et al., 2010, MNRAS, 402, 2403

Murphy T., et al., 2021, PASA, 38, e054

Mutel R. L., Lestrade J. F., 1985, AJ, 90, 493

Mutel R. L., Doiron D. J., Lestrade J. F., Phillips R. B., 1984, ApJ, 278, 220

Mutel R. L., Morris D. H., Doiron D. J., Lestrade J. F., 1987, AJ, 93, 1220

Newton E. R., Irwin J., Charbonneau D., Berta-Thompson Z. K., Dittmann J. A., West A. A., 2016, ApJ, 821, 93

Newton E. R., Irwin J., Charbonneau D., Berlind P., Calkins M. L., Mink J., 2017, ApJ, 834, 85

Nichols J. D., Milan S. E., 2016, MNRAS, 461, 2353

Nichols J. D., Burleigh M. R., Casewell S. L., Cowley S. W. H., Wynn G. A., Clarke J. T., West A. A., 2012, ApJ, 760, 59

Ning H., Chen Y., Ni S., Li C., Zhang Z., Kong X., Yousefzadeh M., 2021, A&A, 651, A118

Nürnberger D., Brandner W., Yorke H. W., Zinnecker H., 1998, A&A, 330, 549

O'Gorman E., Harper G. M., Vlemmings W., 2017, A&A, 599, A47

Oláh K., Strassmeier K. G., Kovári Z., Guinan E. F., 2001, A&A, 372, 119

Osten R. A., Bastian T. S., 2006, ApJ, 637, 1016

Osten R. A., Bastian T. S., 2008, ApJ, 674, 1078

Osten R. A., Wolk S. J., 2009, ApJ, 691, 1128

Pacholczyk A. G., Swihart T. L., 1970, ApJ, 161, 415

Pacholczyk A. G., Swihart T. L., 1971, ApJ, 170, 405

Pallavicini R., Willson R. F., Lang K. R., 1985, A&A, 149, 95

Parker E. N., 1955, ApJ, 122, 293

Payne-Scott R., Yabsley D. E., Bolton J. G., 1947, Nature, 160, 256

Pedersen M. G., Antoci V., Korhonen H., White T. R., Jessen-Hansen J., Lehtinen J., Nikbakhsh S., Viuho J., 2017, MNRAS, 466, 3060

Pineda J. S., Villadsen J., 2023, Nature Astronomy, 7, 569

Pintaldi S., Stewart A., O'Brien A., Kaplan D., Murphy T., 2022, in Ruiz J. E., Pierfedereci F., Teuben P., eds, Astronomical Society of the Pacific Conference Series Vol. 532, Astronomical Society of the Pacific Conference Series. p. 333 (arXiv:2101.05898), doi:10.48550/arXiv.2101.05898

Pope B. J. S., Callingham J. R., Feinstein A. D., Günther M. N., Vedantham H. K., Ansdell M., Shimwell T. W., 2021, ApJ, 919, L10

Pottelette R., Ergun R. E., Treumann R. A., Berthomier M., Carlson C. W., McFadden J. P., Roth I., 1999, Geophys. Res. Lett., 26, 2629

Pritchard J., et al., 2021, MNRAS, 502, 5438

Pritchard J., Murphy T., Heald G., Wheatland M. S., Kaplan D. L., Lenc E., O'Brien A., Wang Z., 2024, MNRAS, p. stae127

Quiroga-Nuñez L. H., Intema H. T., Callingham J. R., Villadsen J., van Langevelde H. J., Jagannathan P., Shimwell T. W., Boven E. P., 2020, A&A, 633, A130

Ramaty R., 1969, ApJ, 158, 753

Ramesh R., Kathiravan C., Chellasamy E. E., 2022, ApJ, 932, 48

Ransom R. R., Bartel N., Bietenholz M. F., Lebach D. E., Ratner M. I., Shapiro I. I., Lestrade J. F., 2002, ApJ, 572, 487

Rau U., 2010, PhD thesis, New Mexico Institute of Mining and Technology, http://www.aoc.nrao.edu/~rurvashi/DataFiles/UrvashiRV_PhdThesis.pdf

Ravi V., et al., 2010, MNRAS, 408, L99

Readhead A. C. S., 1994, ApJ, 426, 51

Reber G., 1940, ApJ, 91, 621

Reber G., 1944, ApJ, 100, 279

Reber G., Greenstein J. L., 1947, The Observatory, 67, 15

Reid H. A. S., Ratcliffe H., 2014, Research in Astronomy and Astrophysics, 14, 773

Reiner M. J., Fainberg J., Stone R. G., 1995, Science, 270, 461

Reylé C., 2018, A&A, 619, L8

Ricker G. R., 2015, in AAS/Division for Extreme Solar Systems Abstracts. p. 503.01

Rigney J., et al., 2022, MNRAS, 516, 540

Robinson P. A., 1992, Sol. Phys., 139, 147

Robinson P. A., Melrose D. B., 1984, Australian Journal of Physics, 37, 675

Robishaw T., Heiles C., 2021, in Wolszczan A., ed., , The WSPC Handbook of Astronomical Instrumentation, Volume 1: Radio Astronomical Instrumentation. World Scientific, pp 127–158, doi:10.1142/9789811203770_0006

Robrade J., Poppenhaeger K., Schmitt J. H. M. M., 2010, A&A, 513, A12

Rodríguez Martínez R., Lopez L. A., Shappee B. J., Schmidt S. J., Jayasinghe T., Kochanek C. S., Auchettl K., Holoien T. W. S., 2020, ApJ, 892, 144

Rose K., et al., 2023, ApJ, 951, L43

Route M., Wolszczan A., 2012, ApJ, 747, L22

Rutledge R. E., Basri G., Martín E. L., Bildsten L., 2000, ApJ, 538, L141

Ryabov V. B., Zarka P., Hess S., Konovalenko A., Litvinenko G., Zakharenko V., Shevchenko V. A., Cecconi B., 2014, A&A, 568, A53

Ryle M., 1949, Proceedings of the Physical Society A, 62, 491

Saur J., Pouquet A., Matthaeus W. H., 2003, Geophys. Res. Lett., 30, 1686

Saur J., Grambusch T., Duling S., Neubauer F. M., Simon S., 2013, A&A, 552, A119

Scargle J. D., 1982, ApJ, 263, 835

Schmitt J., Güdel M., Predehl P., 1994, A&A, 287, 843

Schneider F. R. N., Podsiadlowski P., Langer N., Castro N., Fossati L., 2016, MNRAS, 457, 2355

Schwinger J., 1949, Physical Review, 75, 1912

Shibasaki K., Alissandrakis C. E., Pohjolainen S., 2011, Sol. Phys., 273, 309

Shimwell T. W., et al., 2017, A&A, 598, A104

Shklovski I., 1953, in Dokl. Akad. Nauk. SSSR. p. 983

Shultz M., et al., 2015, MNRAS, 449, 3945

Simões P. J. A., Costa J. E. R., 2006, A&A, 453, 729

Simões P. J. A., Costa J. E. R., 2010, Sol. Phys., 266, 109

Skinner S. L., Brown A., Stewart R. T., 1993, ApJS, 87, 217

Skrutskie M. F., et al., 2006, AJ, 131, 1163

Slee O. B., 1963, Nature, 199, 991

Slee O. B., Nelson G. J., Stewart R. T., Wright A. E., Innis J. L., Ryan S. G., Vaughan A. E., 1987, MNRAS, 229, 659

Slee O. B., Wilson W., Ramsay G., 2008, PASA, 25, 94

Smerd S. F., 1950, Australian Journal of Scientific Research A Physical Sciences, 3, 34

Smerd S. F., Sheridan K. V., Stewart R. T., 1975, Astrophys. Lett., 16, 23

Smith K., Pestalozzi M., Güdel M., Conway J., Benz A. O., 2003, A&A, 406, 957

Song Y., Paglione T. A. D., 2020, ApJ, 900, 185

Spangler S. R., Owen F. N., Hulse R. A., 1977, AJ, 82, 989

Spicer D. S., Benz A. O., Huba J. D., 1982, A&A, 105, 221

Spiegel D. S., Burrows A., Milsom J. A., 2011, ApJ, 727, 57

Stähli M., Gary D. E., Hurford G. J., 1989, Sol. Phys., 120, 351

Stewart R. T., Slee O. B., Budding E., Coates D. W., Thompson K., Bunton J. D., 1989, Space Sci. Rev., 50, 367

Stocke J. T., Scott J. S., 1975, MNRAS, 172, 567

Sürgit D., Erdem A., Budding E., 2010, MNRAS, 407, 497

Sutinjo A., O'Sullivan J., Lenc E., Wayth R. B., Padhi S., Hall P., Tingay S. J., 2015, Radio Science, 50, 52

Takakura T., 1972, Sol. Phys., 26, 151

Tamazian V. S., Malkov O. Y., 2014, Acta Astron., 64, 359

Thyagarajan N., Helfand D. J., White R. L., Becker R. H., 2011, ApJ, 742, 49

Tingay S. J., et al., 2013, PASA, 30, e007

Toet S. E. B., Vedantham H. K., Callingham J. R., Veken K. C., Shimwell T. W., Zarka P., Röttgering H. J. A., Drabent A., 2021, A&A, 654, A21

Torres G., Ribas I., 2002, ApJ, 567, 1140

Treumann R. A., 2006, A&A Rev., 13, 229

Trigilio C., Leto P., Leone F., Umana G., Buemi C., 2000, A&A, 362, 281

Trigilio C., Leto P., Umana G., Buemi C. S., Leone F., 2011, ApJ, 739, L10

Turnpenney S., Nichols J. D., Wynn G. A., Burleigh M. R., 2018, ApJ, 854, 72

Turnpenney S., Nichols J. D., Wynn G. A., Jia X., 2020, MNRAS, 494, 5044

Uchida Y., Sakurai T., 1985, in Kundu M. R., Holman G. D., eds, Vol. 107, Unstable Current Systems and Plasma Instabilities in Astrophysics. pp 281–285

Umana G., Trigilio C., Catalano S., 1998, A&A, 329, 1010

Umana G., et al., 2015, MNRAS, 454, 902

Vedantham H. K., et al., 2020a, Nature Astronomy, 4, 577

Vedantham H. K., et al., 2020b, ApJ, 903, L33

Vedantham H. K., et al., 2023, A&A, 675, L6

Vida K., et al., 2016, A&A, 590, A11

Vidotto A. A., Fares R., Jardine M., Donati J. F., Opher M., Moutou C., Catala C., Gombosi T. I., 2012, MNRAS, 423, 3285

Vigan A., Bonnefoy M., Chauvin G., Moutou C., Montagnier G., 2012, A&A, 540, A131

Villadsen J., Hallinan G., 2019, ApJ, 871, 214

Villadsen J., Hallinan G., Bourke S., Güdel M., Rupen M., 2014, ApJ, 788, 112

Vocks C., et al., 2018, A&A, 614, A54

Wang Z., et al., 2021, ApJ, 920, 45

Wang Z., et al., 2022a, MNRAS, 516, 5972

Wang Y., et al., 2022b, ApJ, 930, 38

Wang Y., et al., 2023, MNRAS, 523, 5661

Watson L. C., Hearnshaw J. B., Pollard K. R., Kilmartin P. M., Gilmore A. C., 2000, MNRAS, 315, 69

Wayth R. B., et al., 2015, PASA, 32, e025

Webb D. F., Howard T. A., 2012, Living Reviews in Solar Physics, 9, 3

Wendker H., 1995, A&AS, 109, 177

Wes McKinney 2010, in Stéfan van der Walt Jarrod Millman eds, Proceedings of the 9th Python in Science Conference. pp 56–61, doi:10.25080/Majora-92bf1922-00a, https://doi.org/10.25080/Majora-92bf1922-00a

West A. A., Hawley S. L., Bochanski J. J., Covey K. R., Reid I. N., Dhital S., Hilton E. J., Masuda M., 2008, AJ, 135, 785

West A. A., Weisenburger K. L., Irwin J., Berta-Thompson Z. K., Charbonneau D., Dittmann J., Pineda J. S., 2015, ApJ, 812, 3

White R. L., 1985, ApJ, 289, 698

White S. M., Franciosini E., 1995, ApJ, 444, 342

White S. M., Kundu M. R., 1997, Sol. Phys., 174, 31

White S. M., Jackson P. D., Kundu M. R., 1989, ApJS, 71, 895

Whiting M., Humphreys B., 2012, PASA, 29, 371

Wild J. P., Smerd S. F., Weiss A. A., 1963, ARA&A, 1, 291

Williams P. K. G., 2018, in Deeg H. J., Belmonte J. A., eds, , Handbook of Exoplanets. Springer, p. 171, doi:10.1007/978-3-319-55333-7_171

Williams P. K. G., Berger E., 2015, ApJ, 808, 189

Winter L. M., Ledbetter K., 2015, ApJ, 809, 105

Winters J. G., Henry T. J., Jao W.-C., Subasavage J. P., Finch C. T., Hambly N. C., 2011, AJ, 141, 21

Wright E. L., et al., 2010, AJ, 140, 1868

Wright N. J., Drake J. J., Mamajek E. E., Henry G. W., 2011, ApJ, 743, 48

Wright E. L., et al., 2013, AJ, 145, 84

Wu C. S., Lee L. C., 1979, ApJ, 230, 621

Yang H., et al., 2017, ApJ, 849, 36

Yu S., Chen B., Sharma R., Bastian T., Mondal S., Gary D., Luo Y., Battaglia M., 2023, arXiv e-prints, p. arXiv:2310.01240

Zarka P., 1998, J. Geophys. Res., 103, 20159

Zarka P., Treumann R. A., Ryabov B. P., Ryabov V. B., 2001, Ap&SS, 277, 293

Zic A., Lynch C., Murphy T., Kaplan D. L., Chandra P., 2019a, MNRAS, 483, 614

Zic A., et al., 2019b, MNRAS, 488, 559

Zic A., et al., 2020, ApJ, 905, 23

Zic A., et al., 2024, MNRAS, p. stae033

Zlotnik E. Y., 1968, Soviet Ast., 12, 245

Zlotnik E. Y., Klassen A., Klein K. L., Aurass H., Mann G., 1998, A&A, 331, 1087

van Haarlem M. P., et al., 2013, A&A, 556, A2

van den Oord G. H. J., de Bruyn A. G., 1994, A&A, 286, 181

van der Walt S., Colbert S. C., Varoquaux G., 2011, Computing in Science and Engineering, 13, 22